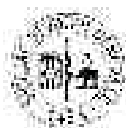

Università degli Studi di Catania

in convenzione con

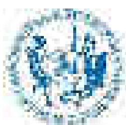

Università degli Studi di Palermo

Dottorato di Ricerca in
Scienza dei Materiali e Nanotecnologie XXX Ciclo

Salvatore Francesco Lombardo

Coupled Kinetic and Electromagnetic approaches for the simulation of complex processes

In the beginning there was light, so why not use it for the future as well?

Tutor:
Prof.ssa M. G. Grimaldi (UniCT)

Co-Tutor:
Dr. A. La Magna (CNR-IMM of Catania)

Coordinatore:
Prof.ssa M. G. Grimaldi (UniCT)

Tesi per il conseguimento del titolo di Dottore di Ricerca

Salvatore Francesco Lombardo: *Coupled Kinetic and Electromagnetic approaches for the simulation of complex processes,* Ph.D. Thesis,

Universita' degli Studi di Catania, Dipartimento di Fisica ed AstronomiaA.A. 2014-2017

Keywords: Laser annealing, simulation, Plasma, PECVD, Comsol®

All rights reserved. No part of the material protected by this copyright notice may be reproduced or utilized in any form of by any means, electronic or mechanical, including photocopying, recording or by any information storage and retrieval system, without permission from the author.

Dedicato a mia moglie.

Contents

Glossary **xiii**

1 Modeling of Plasma Processes **1**
- 1.1 Introduction 1
- 1.2 Plasma equipment 1
  - 1.2.1 Plasma-Enhanced Chemical Vapor Deposition 2
- 1.3 Plasma Modeling 4
  - 1.3.1 Data Required For Plasma Modeling 5
  - 1.3.2 Domain equations 9
  - 1.3.3 Surface reactions and surface species 11
  - 1.3.4 Boundary conditions 12
- 1.4 Plasma chemistry 13
  - 1.4.1 Model settings 13
- 1.5 Simulation results 14
- 1.6 Feature size simulation 19
  - 1.6.1 Experiments 20
- 1.7 Conclusion 24

2 Laser annealing modeling **27**
- 2.1 Introduction 27
- 2.2 Theoretical background 28
  - 2.2.1 Electromagnetic calculations for the heat sources in laser-annealing 28
- 2.3 Front tracking methods 30
  - 2.3.1 Enthalpy method 31
  - 2.3.2 Phase Field Formalism 33
  - 2.3.3 Alternative phase field formulation 36

2.4 Anomalous impurity redistribution 37
2.4.1 Phase field models of impurity trapping and full LA simulations 38
2.5 LIAB: The Laser Innovation Application Booster 41
2.6 Validation study I: 1D case silicon 43
2.7 Validation study II: 1D case non silicon materials 49
2.8 Validation study II 51
2.9 Conclusion 56

3 Laser Annealing of FinFET structures 57
3.1 Introduction 57
3.2 Simulation settings 59
3.3 Focused Results 62
3.3.1 Analysis of temperature geometry dependence 70
3.3.2 Analysis of molten area versus geometry dependence . 74
3.4 Tuning selectivity through polarization 77
3.5 Validation tests 85
3.6 Conclusion 87

4 Advanced modelling 89
4.1 Introduction 89
4.2 The Mechanism of Explosive Crystallization 90
4.3 A phase field model for the EC 94
4.3.1 Dopant/Impurity field 96
4.4 Experimentals 96
4.5 Three phase simulations 99
4.6 Model Validation 106
4.6.1 In-situ transient reflectivity and Micro-structural analysis 106
4.6.2 Chemical analysis 109
4.7 Advanced modeling for alloys 111
4.8 Conclusion 116

5 Advanced modeling of MEOL structure 117
5.1 Introduction 117
5.2 Simulation setting 117
5.3 Simulation results 120
5.3.1 Temperature geometry dependencies 126
5.3.2 Considerations on the melting area shape 129
5.4 Conclusion 133

6 Conclusion 135
6.1 Future development 137

A Material Parameters **139**
A.1 Introduction 139
A.1.1 Phases 139
A.1.2 Dopant 140
A.2 Material set 140
A.3 Silicon 142
A.4 Germanium 145
A.5 Silicon Germanium 148
A.5.1 $Si_{0.5}Ge_{0.5}$ 148
A.6 Copper 150
A.7 Silicon Dioxide 151
A.8 Dielectric materials 152
A.9 Tungsten 154
A.10 Air 155

B The LIAB GUI **157**
B.1 Solver 160

Acknowledgements **161**

Curriculum vitae **163**
List of publications 163
List of conferences 164

Bibliography **167**

List of Figures

1.1 Sketch of the typical ICP configuration 3
1.2 Cross section for Argon 7
1.3 3D image of the simulated reactor 16
1.4 2D section of the reactor 17
1.5 Radially dependent grow rate at t=1 s 17
1.6 3D views of the deposited film at t=1 s 18
1.7 The height of the deposited film at various timesteps 18
1.8 SEM Image and the corresponding simulated structure 21
1.9 A comparison between simulation results and SEM cross sections for different applied powers. 22
1.10 A comparison between simulation results and SEM cross sections by doubling the process time 23
1.11 A comparison of the effect of different geometries. The original one (on the left) and a thinner one (on the right panel). . . . 23

2.1 Plot of all the laser shape 29
2.2 Temperature and phase dependent $\widetilde{C_p}$ 32
2.3 Interface speed for amorphous and crystalline phases 35
2.4 Free energy density for different temperatures 37
2.5 Comparison between experimental and simulated SIMS profile, 1D case 2 J/cm^2 39
2.6 Comparison between experimental and simulated, with two-state model, SIMS profile 40
2.7 Screenshot of the LIAB Graphical User Interface 42
2.8 Simulation example of the Laser Annealing process, reporting heat source, phase and temperature 43
2.9 The simulated 1D structure 45

2.10 Mesh of the 1D structure 46
2.11 Simulated maximum temperature in the 1D Si structure for 0.5 J/cm^2 fluence 47
2.12 Simulated maximum temperature in the 1D Si structure for 1.0 J/cm^2 fluence 47
2.13 Simulated maximum temperature in the 1D Si structure for 2.0 J/cm^2 fluence 48
2.14 Comparison between simulated and experimental melt depth in the Dd structure for the Si case 49
2.15 Simulated maximum temperature in the 1D Ge structure for 0.5 J/cm^2 fluence 50
2.16 Simulated maximum temperature in the 1D Cu based structure for 1.0 J/cm^2 fluence 50
2.17 Schematic of the 2D structure 52
2.18 Comparison of the maximum temperature in 1D-2D Ge structure for 0.4 J/cm^2 53
2.19 Comparison of the maximum temperature in 1D-2D Ge structure for 0.8 J/cm^2 54
2.20 Comparison of the maximum temperature in 1D-2D Cu structure for 2.0 J/cm^2 54
2.21 Comparison of the maximum temperature in a 1D-2D SiGe structure for 0.6 J/cm^2 55
2.22 Comparison of the maximum temperature in 1D-2D SiGe structure for 1.2 J/cm^2 56

3.1 FinFET in a planar configuration 58
3.2 FinFET geometry 58
3.3 Simulated FinFET 59
3.4 A TEM image of the FinFET 61
3.5 Simulated FinFET structure 61
3.6 Maximum temperature in the top-Fin for pitch of 35 nm, 0.6 J/cm^2 63
3.7 Maximum temperature in the top-Fin for pitch of 35 nm, 0.7 J/cm^2 63
3.8 Maximum temperature in the top-Fin for pitch of 35 nm, 0.8 J/cm^2 64
3.9 Temperature, heat source and phase for pitch of 35 nm 66
3.10 Maximum temperature in the top-Fin for pitch of 45 nm, 0.6 J/cm^2 67
3.11 Maximum temperature in the top-Fin for pitch of 45 nm, 0.7 J/cm^2 67
3.12 Maximum temperature in the top-Fin for pitch of 45 nm, 0.8 J/cm^2 68

3.13 Maximum temperature in the top-Fin for pitch of 135 nm, 0.6 J/cm^2 . . . 68
3.14 Temperature, heat source and phase for pitch of 135 nm . . . 69
3.15 Comparison of the heat source for different geometries 71
3.16 Maximum temperature in the FinFET for different polarization and pitch values, case $0.6 J/cm^2$ . . . 72
3.17 Maximum temperature in the FinFET for different pitch and laser energies. The polarization is 0° . . . 73
3.18 Maximum temperature in the FinFET for different pitch and laser energies values. Polarization is 45° . . . 73
3.19 Maximum temperature in the FinFET for different pitch and laser energies values. Polarization is 90° . . . 74
3.20 Melt area for different pitch and laser energies values. Polarization is 0° . . . 75
3.21 Melt area for different pitch values and laser energies. Polarization is 45° . . . 76
3.22 Melt area pitch and laser energies values. Polarization is 90° . 76
3.23 Melt area for different polarization values, for 0.7 J/cm^2 case 77
3.24 Comparison between the maximum temperature in the top of the Fin and in the substrate, pitch 35 nm and 0.7 J/cm^2 . . . 79
3.25 Comparison between the maximum temperature in the top of the Fin and in the substrate, pitch 45 nm and 0.7 J/cm^2 . . . 79
3.26 Comparison between the maximum temperature in the top of the Fin and in the substrate, pitch 135 nm and 0.7 J/cm^2 . . 80
3.27 Comparison between the maximum temperature in the top of the Fin and in the substrate . . . 80
3.28 Maximum temperature in the FinFET for different polarization and pitch values, case $0.6 J/cm^2$ . . . 82
3.29 Maximum temperature in the FinFET for different pitch and laser energies values. Polarization is 0° . . . 82
3.30 Maximum temperature in the FinFET for different pitch and laser energies values. Polarization is 45° . . . 83
3.31 Maximum temperature in the FinFET for different pitch and laser energies values. Polarization is 90° . . . 84
3.32 SEM images of defect level . . . 86
3.33 Comparison with damage experiment . . . 87

4.1 Schematic evolution of the E.C. . . . 92
4.2 Schematic evolution for middle fluence cases . . . 93
4.3 [Schematic evolution for higher fluence cases . . . 93
4.4 Comparison between the free energy function of Wheeler and for our method . . . 95
4.5 TEM image of the sample before laser process. The amorphous layer ranges between 30-35 nm. . . . 98

4.6 Initial configuration for phase and dopant 100
4.7 Snapshot before the E.C. event 101
4.8 Snapshot of the E.C. event 102
4.9 Snapshot during the secondary melting 103
4.10 Snapshot at the end of the simulation 104
4.11 Temperature at the surface for different fluences 106
4.12 Comparison between in situ reflectivity and simulation, and side by side the corresponding TEM images 108
4.13 SIMS measurement for different fluences 109
4.14 Comparison between SIMS and simulation for 0.55 J/cm^2 case 110
4.15 Comparison between SIMS and simulation for 1.2 J/cm^2 case 111
4.16 Snapshot of the simulation for t=50ns 113
4.17 Snapshot of the simulation for t=100ns 114
4.18 Snapshot of the simulation for t=160ns 114
4.19 Snapshot of the simulation for t=50ns 115
4.20 Maximum temperature and melt area in irradiated 1D SiGe . 116

5.1 MEOL structure 119
5.2 Maximum temperature for a MEOL geometry for pitch value of 35 nm and laser irradiation of 0.4 J/cm^2 121
5.3 Maximum temperature and molten area for the MEOL geometry for pitch value of 35 nm and laser irradiation of 0.5 J/cm^2 122
5.4 Maximum temperature and molten area for the MEOL geometry for pitch value of 35 nm and laser irradiation of 0.6 J/cm^2 123
5.5 Maximum temperature and molten area for the MEOL geometry for pitch value of 55 nm and laser irradiation of 0.5 J/cm^2 124
5.6 Maximum temperature and molten area for the MEOL geometry for pitch value of 75 nm and laser irradiation of 0.5 J/cm^2 125
5.7 Maximum temperature for the MEOL geometry for pitch value of 100 nm and laser irradiation of 0.5 J/cm^2 126
5.8 Maximum temperature in the MEOL structure for different polarization and pitch values, case 0.5 J/cm^2 127
5.9 Maximum temperature in the MEOL structure for different pitch and laser energy values. Polarization is 0° 128
5.10 Maximum temperature in the MEOL structure for different pitch and laser energies values. Polarization is 45° 128
5.11 Maximum temperature in the MEOL structure for different pitch and laser energies values. Polarization is 90° 129
5.12 Melting shape for different pitch values 130

5.13 Melt area for different pitch and laser energies values. Polarization is 0° . . . 131
5.14 Melt area for different pitch and laser energies values. Polarization is 45° . . . 132
5.15 Melt area pitch and laser energies values. Polarization is 90° . 132
5.16 Melt area for different polarization values, for 0.5 J/cm^2 case 133

A.1 Optical parameter of $Si_{1-x}Ge_x$ . . . 148

B.1 The 2D structure draw panel in the LIAB GUI . . . 158
B.2 The viewer panel in the LIAB GUI . . . 159
B.3 The database panel in the LIAB GUI . . . 160

List of Tables

1.1 Balance and rate equations used in the plasma domains . . . 6
1.2 Surface reactions . . . 8
1.3 Parameters of the surface species . . . 8
1.4 Additional parameters of the species. . . . 9
1.5 Design of Experiments of the dry etching plasma case . . . 19

A.1 Data parameter meanings . . . 141
A.2 Data parameter of Silicon . . . 144
A.3 Data parameter of Germanium . . . 147
A.4 Data parameter of $Si_{1-X}Ge_X$ . . . 149
A.5 Data parameter of $Si_{0.5}Ge_{0.5}$. . . . 150
A.6 Data parameter of copper. . . . 151
A.7 Data parameter of Silicon dioxide. . . . 152
A.8 Data parameter of low-κ. . . . 153

A.9 Data parameter of silicon nitride. 153
A.10 Data parameter of tantalium nitride. 153
A.11 Data parameter of titanium nitride. 154
A.12 Data parameter of tungsten. 155
A.13 Data parameter of air. 156

Glossary

B Boron, see Appendix A.

CAD Computer-Aided Design.

CMOS Complementary Metal Oxide Semiconductor.

Cu Copper, see Appendix A.

CVD Chemical Vapor Deposition is a chemical process used to produce high quality, high-performance, solid materials. The process is often used in the semiconductor industry to produce thin films. In typical CVD, the wafer (substrate) is exposed to one or more volatile precursors, which react and/or decompose on the substrate surface to produce the desired deposit.

DOE The Design Of Experiments is the design of any task that aims to describe or explain the variation of information under conditions that are hypothesized to reflect the variation.

DOF The Degree Of Freedom of a system is the number of independent parameters that define its configuration.

EM ElectroMagnetic.

Ge Germanium, see Appendix A.

GUI Graphical User Interface.

LA Laser Annealing.

P Phosphorus, see Appendix A.

RT The Room Temperature. In our simulation is always 300 K.

sccm standard cubic centimeters per minute, a flow measurement term, indicating cm^3/min at a standard temperature and pressure.

SEM A Scanning Electron Microscope is a type of electron microscope that produces images of a sample by scanning the surface with a focused beam of electrons.

Si Silicon, see Appendix A.

SiGe Silicon Germanium, see Appendix A.

SIMS Secondary-Ion Mass Spectrometry is a technique used to analyze the composition of solid surfaces and thin films by sputtering the surface of the specimen with a focused primary ion beam and collecting and analyzing ejected secondary ions.

TCAD Technology CAD (or Technology Computer Aided Design) is a branch of electronic design automation that models semiconductor fabrication and semiconductor device operation. Included are the modelling of process steps (such as diffusion and ion implantation), and modelling of the behavior of the electrical devices based on fundamental physics, such as the doping profiles of the devices.

TEM The Transmission electron microscopy, is a microscopy technique in which a beam of electrons is transmitted through a specimen to form an image. An image is formed from the interaction of the electrons with the sample as the beam is transmitted through the specimen.

Foreword

Electromagnetic fields are often used to manipulate matter in many technological processes including those applied in emerging fields related to nanotechnology. Generalizing this concept, manipulation processes use forces or fields generated by electromagnetic interactions (e.g. a thermal process at constant and uniform temperature uses lamps as heat sources). Often, in the description of the evolution induced by the process it is more convenient to identify a simplified scheme of the driven force/field (i.e. constant high temperature in the previous example). Of course, these simplifications affect also the theoretical analysis of the material modification promoted by the processes. Reconsidering the cited example of thermal process, temperature is just a parameter of the diffusion equations used to evaluate the material redistribution activated by the high temperature. In these cases also the experimental control of the process takes advantage of the definition of quasi-equilibrium thermodynamic parameters as process parameters.

However, the effect of the interaction between the electromagnetic field and the material is more difficult to control in some processes where the amount of energy released from the field towards the samples depends dynamically and self-consistently on the material kinetic evolution. The self-consistency makes difficult inferring the manipulation effects on a new system from the previous phenomenology on different systems. In this case, optimized new applications usually need complex and expensive Design of Experiments (DOE) in terms of man power and materials. This PhD dissertation focuses on such processes. In particular, considering plasma and laser annealing processes, we aim to demonstrate that a reliable process control can be obtained by means of simulation methodologies which consider the full complexity of the process kinetics. In spite of the differences in terms of machines and role in the manufacturing flow, plasma and laser processes share two striking common features, from the modeling perspective:

- The manipulation results critically depend on the structure of the sample (especially if sub-micron structures are processed);
- Electromagnetic simulations coupled with many-component kinetic models are the key aspect of the multi-scale / multi-physics formalism implemented in the numerical codes.

In the following we summarize the plan of the thesis. Chapter 1 is dedicated to plasma processes. We will discuss how semi-quantitative predictions can be obtained by simulations at the feature size of the processed micro-systems: quantitative modeling can be only achieved by coupling the micro-scale kinetic modeling with the plasma status simulations at the macro scale of the plasma reactor. For a particular equipment class we will present numerical methods and results.

Equipment simulation is not needed for the case of laser processes, since the pulse (duration in the range of 10-100 ns) interacting with the irradiated samples is controllable with precision. However, the formalism and results discussion are significantly complex when the non-linear trends of this process are a function of the sample geometry and material, especially when liquid-solid phase transitions take place during the irradiation. As a consequence, we have dedicated four chapters to the laser annealing process. Chapter 2 is dedicated to the formalism and its original implementation in numerical tools with the aid of the open source FEniCS (`https://fenicsproject.org/`) routines. Aiming to validate the code, benchmarks and comparisons with results of a commercial simulator (Comsol Multiphysics®) will be also presented in planar 1D and 2D systems.

Computer aided process design of laser processes in a device structure will be discussed in Chapter 3, considering the reference Fin Field Effect Transistor (FinFET) geometry and materials used in contemporary integrated circuits. In this chapter, an expert reader in process engineering can appreciate the use of the simulator in a practical case and how geometry, laser energy density and light polarization can be tuned to obtain the desired results (usually regarding the localized melting and non-destructive heating of far regions within the chip).

Extensions of the phase kinetic formalism and their implementations, both elaborated during the PhD period, are presented in Chapters 4 and 5. These extensions introduce advanced features of the material kinetic modeling in order to allow quantitative simulations when amorphous and alloyed regions are present in the structures. In Chapter 4 we analyze the explosive re-crystallization phenomenon, within the concurrent three phases (amorphous, liquid, crystal) and an ultra fast evolution, that characterizes the irradiation of amorphous Si and Ge samples.

The main challenge in the alloy model is the dependence of the thermal parameters of the alloy on the local alloy fraction. This modeling extension

will be applied, in Chapter 5, for the laser process design of the Middle-End of Line (MEOL) structure. This structure connects and, as a consequence, is built between the active part of the chip and the final interconnections, and it contains alloyed "amorphous" SiGe pockets.

Appendixes describe the materials calibration (Appendix A) and the graphical user interface of the developed numerical tool (Appendix B).

1

Modeling of Plasma Processes

1.1 Introduction

This chapter is dedicated to the modeling of plasma processes and their numerical simulations. These processes are used for the controlled (nowadays manufacturing requires resolution in the nm scale) deposition or etching of thin films in blanketed or structured samples. Plasmas are conductive assemblies of charged particles, neutrals and fields that exhibit collective effects. Plasma systems are, by their intrinsic nature, complicated systems with a high degree of non-linearity. Small changes to the electrical input or plasma chemistry can result in significant changes in the discharge characteristics. Theoretical models of low-temperature plasmas represent the amalgamation of fluid mechanics, reaction engineering, physical kinetics, heat transfer, mass transfer, and electromagnetics. The net result is a true multi-physics problem involving complicated coupling between the different physics. A reliable approximation is obtained using the Boltzmann Equation, Two-Term Approximation, that computes the electron transport properties and source coefficients from a set of electron impact collision cross sections. For space-dependent models, the reactions and the species, which constitute the plasma, have to be studied. In a simulation of a real reaction chamber also the fluid velocity and the gas temperature fields have to be computed.

1.2 Plasma equipment

There are many different types of plasma that are typically of interest. The main difference between the plasmas relies on the different mechanism of energy transfer between the electrons and fields. The common types of

plasma are:

- Inductively coupled plasmas
- Capacitively coupled plasmas
- Transformer Coupled plasmas
- Microwave plasmas
- Light sources
- Electrical breakdown
- Space thrusters and Magnetron Sputtering
- Direct Current discharges
- Dielectric barrier discharges
- Electron cyclotron resonance

Here we describe briefly the plasma equipment that we used in our simulation, specifically an Inductively Coupled Plasmas (ICP) reactor. We note that generalization to other kinds of equipment needs mainly modification of the Computer Aided Design (CAD) of the machine, whilst the applied model has strong similarities. Indeed, we have also essentially the same model framework in the global formulation (i.e. neglecting the CAD specifications) to a Transformer Coupled plasmas (TCP) case in section 1.6. Inductively coupled plasmas were first used in the 1960's as thermal plasmas in coating equipment [1] and in the 1990's they are used in film processing industry as a way of fabricating large semiconductor wafers. These devices operate with electronic temperature of the order of 10000 K, but at very low pressure, from 0.2 to 130 Pa, as a consequence the gas temperature remains close to room temperature. Low-pressure ICP is interesting because can create a relatively uniform plasma density over a large volume, with a high plasma density, around 10^{18} $1/\mathrm{m}^3$, which results in a significant ion flux to the surface of the wafer [2]. In fig. 1.1 a typical ICP configuration is shown.

1.2.1 Plasma-Enhanced Chemical Vapor Deposition

ICP configuration can work in etching (i.e. dry etch) or deposition mode. We have considered in greater detail the latter case (TCP dry etching is simulated in a simplified global framework see section 1.6) which is used for the Plasma-enhanced chemical vapor deposition (PE-CVD) process. The PE-CVD is an alternative technique to traditional Chemical Vapor Deposition (CVD) because it can provide a very efficient deposition process, trough the generation of the radical species in the plasma, without the need for very

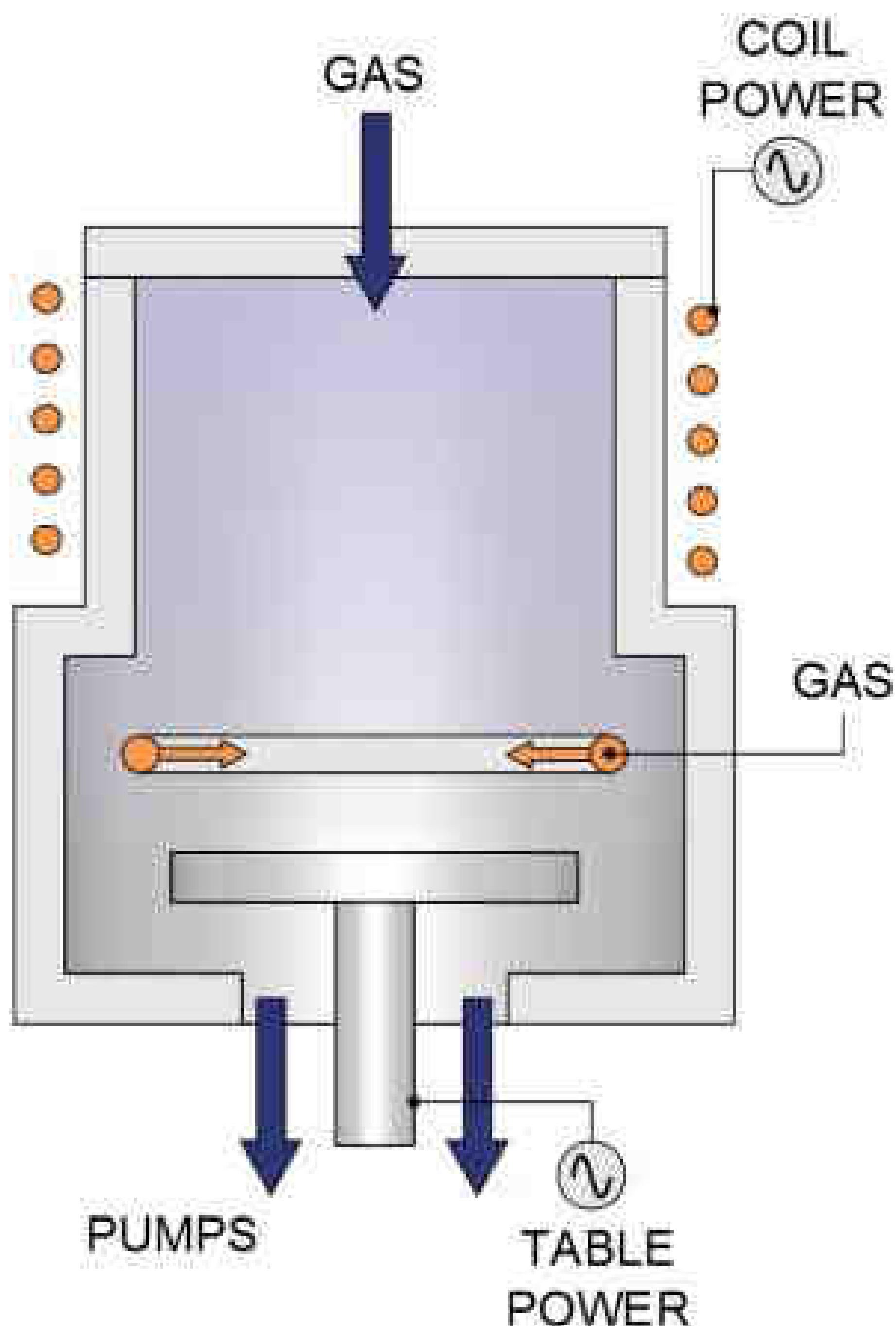

Figure 1.1: *Sketch of the typical ICP configuration used in the semiconductor processing industry. The gas injected from the top of the chamber (usually chemical inactive Argon Ar) ionizes and activates easily the plasma formation allowing the driving mechanism for the species reactions, while the gas injected below is the one useful for the deposition (Silane* SiH_4 *in our case). A pump keeps the pressure constant.*

high gas temperatures. The use of a silane (SiH_4) plasma creates, trough electron impact reactions, highly reactive silicon hydrides and hydrogen gas. The chemical reactions that take place on the surface are, also, very important to define the plasma status. Typical the PE-CVD reactors are in ICP configuration, although microwave plasmas are also used.

1.3 Plasma Modeling

The study of plasma is performed in all space dimensions: 0D (or global, where space variations are neglected), 1D, 2D, and 3D. We study the plasma problem with the Comsol Multyphisics® software. All methods used to solve plasma problems essentially solve an appropriate transport equation along with Maxwell's equations, and can be divided in to three types:

- The **Kinetic** approach calculates the distribution function of ions and electrons in a plasma by solving either the Boltzmann equation, or an approximation, like the Fokker-Planck equation. The drawback of this approach lies in the difficulty to implement arbitrary plasma chemistries and a high computational cost, especially for 2D and 3D systems, but it allows to use and arbitrary shape in energy space for the electron energy distribution.

- The **Fluid** method describes the plasma in terms of macroscopic quantities by assuming a specific form of the distribution function and taking velocity moments of the Boltzmann equation. The use of this approach implies the use of the finite element method (FEM) analysis to solve the partial differential equations. As a consequence, it is easy to couple the electron dynamics to the electromagnetic fields, and also Computational Fluid Dynamics (CFD), thermal analysis and so on that are based on the FEM approach. Define complex chemistries is straightforward. *Fluid approximation is the scheme we have adopted for the plasma simulation.*

- The **Hybrid** method tries to combine multiple approaches, treating, usually, the electrons kinetically (using Fokker-Planck equation or Monte Carlo method), and the ions and other radical species with a fluid model, offering the fidelity of kinetics models and the speed of the fluid one. Moreover, they offer a suitable scheme for the coupling with Monte Carlo feature scale simulations, since particle and energy distributions are used sequentially to pick up the parameter of the plasma species interacting with the microstructure (for the details see section 1.6)

1.3.1 Data Required For Plasma Modeling

Modeling of low-temperature plasmas is not only difficult because of the large number of physical processes occurring but also because of the amount of data that needs to be supplied to calibrate reliably the model[3]. One of the main difficulties is to find a complete and physically correct chemical mechanism for the plasma of interest. This can involve just a handful of reactions and species (as for Argon), or in the case of molecular gases there can be hundreds of reactions and then thousands of species.

Electron Impact Reactions For each electron impact reaction, the information required is the reaction formula and some other data to indicate the dependency of the reaction rate on the electron energy [4]. The most common way of accomplishing this is to specify cross-section data for each of the electron impact reactions, see fig. 1.2 where we report the cross section only for the Argon case. The electron impact equation used in the simulations is shown in table 1.1. Some useful resources for cross-section data are available at the following links:

- `https://fr.lxcat.net/home/`
- `http://kinema.com/plasma-chemistry-modeling/`
- http://jila.colorado.edu

If cross-section data are not available then the rate coefficient can be specified with a constant value, an Arrhenius expression, or by a lookup table.

Depending on the type of electron impact collision, the following data is also required:

- The mass ratio of the electron to the target species for elastic collisions
- The energy loss (in eV) for inelastic collisions
- The ratio of statistical weights between the target and produced species if a detailed balance is required.

Reactions For gas phase reactions, the forward rate constant using either Arrhenius coefficients or numeric data is required. If the reaction is reversible, the reverse rate constant has to be provided in the same way. The typical reaction equations are shown in table 1.1, reactions numbers 6 and 7.

Reaction	Formula	Type	$\delta\varepsilon(eV)$
1	e+Ar $\rightarrow$ e+Ar	Elastic	0
2	e+Ar $\rightarrow$ e+Ar_E	Excitation	11.5
3	e+Ar_E $\rightarrow$ e+Ar	Superelastic	-11.5
4	e+Ar $\rightarrow$ 2e+Ar^+	Ionization	15.8
5	e+Ar_E $\rightarrow$ 2e+Ar^+	Ionization	4.24
6	Ar_E+Ar_E $\rightarrow$ e+Ar+Ar^+	Penning ionization	-
7	Ar_E+Ar $\rightarrow$ Ar+Ar	Metastable quenching	-
8	e+SiH_4 $\rightarrow$ SiH_4^-	attachment	0
9	e+SiH_4 $\rightarrow$ e+ SiH_4	elastic	
10	e+SiH_4 $\rightarrow$ e+SiH_{4E}	Excitation	0.115
11	e+SiH_4 $\rightarrow$ e+SiH_{4E}	Excitation	8.1
12	e+SiH_4 $\rightarrow$ e+SiH_{4E}	Excitation	8.92
13	e+SiH_4 $\rightarrow$ 2e+SiH_4^+	Ionization	12.9

Table 1.1: *Balance and rate equations used in the plasma domain. Argon cross sections extracted from PROGRAM MAGBOLTZ, VERSION 7.1 JUNE 2004. The silane reactions are taken from [5]*

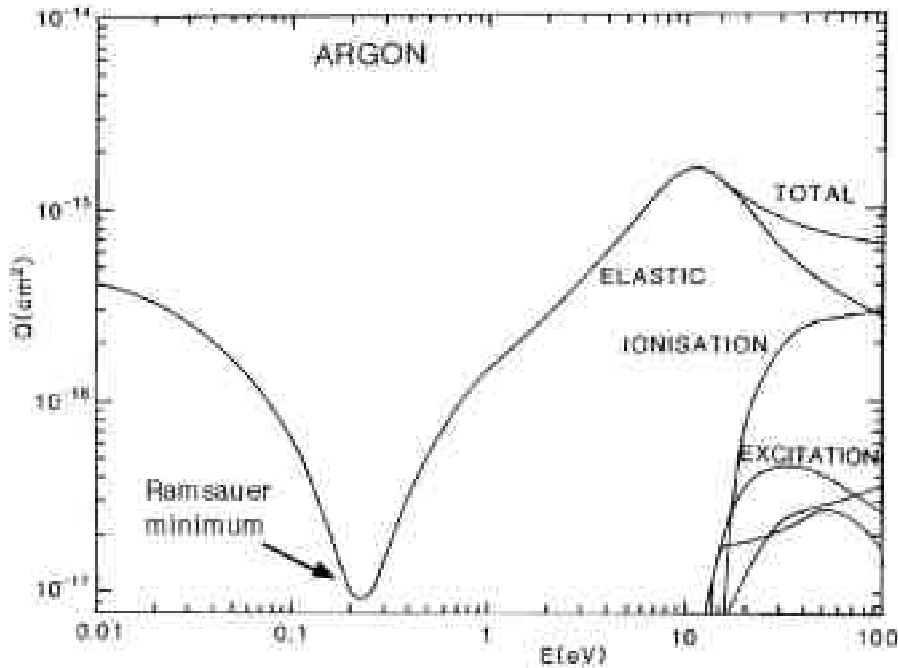

Figure 1.2: *Cross section for argon. Every curve represents an electron impact reaction*

Surface Reactions For surface reactions the following data are required:

- The forward sticking or rate coefficient, which can either be a numeric value or specified in terms of Arrhenius parameters as a function of the surface temperature
- For first-order reactions, the total surface site concentration is required
- For surface reactions that result in emission of secondary electrons, the secondary emission coefficient and mean energy of the secondary electrons are required

The surface reactions are shown in table 1.2. Surface species parameters are reported in table 1.3.

Species For each of the non-electron species the following information is required:

- The molecular weight of the species
- The potential characteristic length of the species; required to compute the correct diffusivity and mobility

Reaction	Formula	Sticking coefficient	Boundary
1	SiH_4+2Si_s → Si_b+2SiH_s+H_2	1E-3	only wafer
2	SiH_s → Si_s+0.5H_2	1E-4	only wafer
3	Ar_E → Ar	1	all walls
4	Ar^+ → Ar	1	all walls
5	SiH_4^+ → SiH_4	1	all walls
6	SiH_{4E} → SiH_4	1	all walls

Table 1.2: *Surface reactions in the plasma reactor. Equations 1-2 are active only in the wafer region and lead to the formation of the deposited film. The excited and ionized atoms that hit a reactor wall return to the ground state.*

Species	density of surface sites Γ_0 [mol/m^2]	initial site fraction Z_k	Density [kg/m^3]
Si_s	1.95 E-5	0.995	/
SiH_s	1.95 E-5	0.005	/
Si_b	/	/	2329

Table 1.3: *Parameters of the surface species. The Si_b is a bulk species and it is not involved in the reactions as a reactant. As a consequence, only its density is a relevant parameter.*

Species	Molar mass M_w [kg/mol]	characteristic length σ [m]	Diffusion coefficient D_f [m^2/s]	initial mass fraction
Ar	0.04	3.33E-10	0.01	1
H_2	0.002	3.92E-10	0.01	1E-5
SiH_4	0.032	4.08E-10	0.01	1E-2

Table 1.4: *Additional parameters of the species. Excited and ionized species have the same parameters as the atoms in the ground state.*

- The potential energy minimum of the species; required to compute the correct diffusivity and mobility

To solve also for the neutral gas temperature, the following additional information is required:

- The species molar enthalpy, entropy, and specific heat, which can be introduced directly as a function of temperature or by using NASA polynomials
- In the case of electronically excited species or ions, the properties of the ground state species can be introduced, and an additional contribution to the species enthalpy can be also provided.

1.3.2 Domain equations

The electron density and mean electron energy are computed by solving a pair of drift-diffusion equations. Convection of electrons due to fluid motion is neglected.

$$\frac{\partial n_e}{\partial t} + \nabla \cdot [-n_e (\boldsymbol{\mu_e} \cdot \boldsymbol{E}) - \nabla(\boldsymbol{D_e} \cdot n_e)] = R_e - (\boldsymbol{u} \cdot \nabla) n_e \qquad (1.1)$$

$$\frac{\partial n_\varepsilon}{\partial t} + \nabla \cdot [-n_\varepsilon (\boldsymbol{\mu_\varepsilon} \cdot \boldsymbol{E}) - \nabla(\boldsymbol{D_\varepsilon} \cdot n_\varepsilon)] + \boldsymbol{E} \cdot \boldsymbol{\Gamma_e} = R_\varepsilon - (\boldsymbol{u} \cdot \nabla) n_\varepsilon \qquad (1.2)$$

The electron source R_e and the energy loss due to inelastic collisions R_ε are defined later. The transport properties may be tensors and functions of the mean electron energy and a DC magnetic flux density.The electron diffusivity, energy mobility, and energy diffusivity are computed from the electron mobility using:

$$\boldsymbol{D_e} = \boldsymbol{\mu_e} T_e \qquad (1.3)$$

$$\boldsymbol{D_\varepsilon} = \boldsymbol{\mu_\varepsilon} T_e \qquad (1.4)$$

$$\boldsymbol{\mu_\varepsilon} = \frac{5}{3} \boldsymbol{\mu_e} \qquad (1.5)$$

The source coefficients in the above equations are determined by the plasma chemistry using rate coefficients. Suppose that there are M reactions that contribute to the growth or decay of electron density and P inelastic electron-neutral collisions. In general $P \gg M$. In the case of rate coefficients, the electron source term is given by:

$$R_e = \sum_{j=1}^{M} x_j k_j N_n n_e \tag{1.6}$$

where x_j is the mole fraction of the target species for reaction j, k_j is the rate coefficient for reaction j, in m^3/s, and N_n is the total neutral number density, in m^{-3}. The electron energy loss is obtained by summing the collisional energy loss over all reactions:

$$R_\varepsilon = \sum_{j=1}^{P} x_j k_j N_n n_e \Delta\varepsilon_j \tag{1.7}$$

where $\Delta\varepsilon_j$ is the energy loss from reaction j. The rate coefficients can be computed from cross section data by the following integral

$$k_k = \gamma \int_0^\infty \varepsilon \sigma_k(\varepsilon) f(\varepsilon) d\varepsilon \tag{1.8}$$

where $\gamma = \left(\frac{2q}{m_e}\right)^{0.5}$, m_e is the electron mass, ε is energy, σ_k is the collision cross section, and f is the electron energy distribution function. In this case a Maxwellian EEDF is assumed.

Non electron species Transport of the non-electron species is determined from solving a modified form of the Maxwell-Stefan equations

$$\rho \frac{\partial w_k}{\partial t} + \rho(\boldsymbol{u} \cdot \nabla) w_k = \nabla \cdot \mathbf{j_k} + R_k \tag{1.9}$$

where w_k is the mass fraction of the k species and

$$\mathbf{j_k} = \rho w_k D_{k,m} \nabla \ln w_k + D_{k,m} \nabla \ln M + D^T \nabla T - Z_k \mu_k \mathbf{E} \tag{1.10}$$

The mass fraction of silane is not directly computed. Its value comes from the sum of the mass fractions and it must be equal to one.

Electromagnetic field The electrostatic field is computed using Poisson's equation:

$$-\nabla \cdot \varepsilon_0 \varepsilon_r \nabla V = \rho \tag{1.11}$$

The space charge density ρ is automatically computed based on the plasma chemistry using the formula:

$$\rho = q\left(\sum_{k=1}^{N} Z_k n_k - n_e\right) \tag{1.12}$$

We solve for the magnetic vector potential in the frequency domain:

$$\left(j\omega\sigma - \omega^2\varepsilon_0\varepsilon_r\right) A_\varphi + \nabla \times \left(\mu_0^{-1}\mu_r^{-1}\nabla \times A_\varphi\right) = \frac{\sigma V_{loop}}{2\pi r} \tag{1.13}$$

Gas flow The neutral gas flow is determined by the Compressible Navier-Stokes equations with a modified heat source.

$$\frac{\partial\rho}{\partial t} + \nabla \cdot \rho\mathbf{u} = 0 \tag{1.14}$$

$$\rho\frac{\partial\mathbf{u}}{\partial t} + \rho\left(\mathbf{u}\cdot\nabla\right)\mathbf{u} = -\nabla p + \nabla\cdot\eta\left[\nabla\mathbf{u} + \left(\nabla\mathbf{u}\right)^T\right] \tag{1.15}$$

The gas temperature is computed by solving the energy equation.

$$\begin{aligned}\rho C_p\frac{\partial T}{\partial t} + \rho C_p\left(\mathbf{u}\cdot\nabla\right)T = -\frac{T}{\rho}\frac{\partial\rho}{\partial T}\left(\frac{\partial p}{\partial t} + \mathbf{u}\cdot\nabla p\right) + \nabla \\ \cdot\,\kappa\nabla T + \sum_{j=1}^{N} r_j\left(F\Delta\varepsilon - \Delta H_j\right)\end{aligned} \tag{1.16}$$

The last term on the right hand side of the energy equation can lead to substantial gas heating for molecular gases at higher pressures.

1.3.3 Surface reactions and surface species

The surface rate for reaction i is given by:

$$q_i = k_{f,i}\prod_{k=1}^{K} c_k^{v_{ki}^f} \tag{1.17}$$

where the rate constant, k_f is given by:

$$k_{f,i} = \frac{1}{4}\left(\frac{\gamma_i}{1-\gamma_i/2}\right)\frac{1}{\left(\Gamma_{tot}\right)^m}\sqrt{\frac{8RT_s}{\pi M_n}} \tag{1.18}$$

and c_k is the concentration of species k which may be volumetric or surface species, m is the reaction order minus 1, T_s is the surface temperature, R is the gas constant and M_n is the mean molecular weight of the gas

mixture. γ_i is the dimensionless sticking coefficient. For the surface species the following equations are solved:

$$\frac{d\Gamma}{dt} = \sum_{i=1}^{N} q_i \Delta\sigma_i \tag{1.19}$$

where Γ is the surface site concentration, q_i is the reaction rate for reaction i, $\Delta\sigma_i$ is the dimensionless change in site occupancy number for reaction i.

$$\frac{dZ_k}{dt} = \frac{R}{\Gamma_{tot}} \tag{1.20}$$

where Γ_{tot} is the total surface site concentration, Z_k is the dimensionless site fraction and R is the surface rate expression. For the bulk surface species, the following equation is solved for the deposition height:

$$\frac{dh}{dt} = -\frac{RM_w}{\rho} \tag{1.21}$$

where h is the total growth height, M is the molecular weight and ρ is the density of the bulk species.

1.3.4 Boundary conditions

Fluid Flow The following boundary conditions are used on the surface of the wafer. The mass averaged velocity is constrained using:

$$\mathbf{u} = -\frac{M_f}{\rho}\mathbf{n} \tag{1.22}$$

where M_f is the inward (or outward in this example) mass flux which is defined, from

$$M_f = \sum_{k=1}^{K_g} M_k \dot{s_k} \tag{1.23}$$

where s_k is the surface rate expression for each species which comes from summing the surface reaction rates multiplied by their stoichiometric coefficients over all surface reactions:

$$\dot{s_k} = \sum_{i=1}^{I} v_{ki} q_i \tag{1.24}$$

Hydrogen Mass Fraction The flux of hydrogen at the surface of the wafer comes from the surface reactions:

$$\mathbf{n} \cdot \mathbf{j} = M_k s_k \tag{1.25}$$

Energy equation For the energy equation, the following boundary condition is used:

$$\mathbf{n} \cdot \kappa \nabla T = \sum_{i=1}^{I} q_i h_i \qquad (1.26)$$

where h_i is the molar enthalpy change due to reaction i.

1.4 Plasma chemistry

Argon's reaction set is one of the simplest mechanisms to implement at low pressures. The electronically excited states can be lumped into a single species which results in a chemical mechanism consisting of only 3 species and 7 reactions. Table 1.1 on page 6 reports the equations used.

Stepwise ionization (reaction 5) can play an important role in sustaining low pressure argon discharges. Excited argon atoms are consumed via superelastic collisions with electrons, quenching with neutral argon atoms, ionization or Penning ionization where two metastable argon atoms react to form a neutral argon atom, an argon ion and an electron. Reaction number 7 is responsible for heating of the gas. The 11.5 eV of energy which was consumed in creating the electronically excited argon atom is returned to the gas as thermal energy when the excited metastable state quenches. In addition to volumetric reactions, the surface reactions implemented are reported in table 1.2, where the subscript s denotes the "surface species" which means that the species only exist on the surfaces where the reaction is occurring, while the subscript b indicates that a species belongs to the bulk. Since bulk species cannot participate in surface reactions, they must only be products and not reactants in a surface reaction. Only the surface equations 1-2, that are active only in the wafer zone, lead at the formation of the deposited film, following eq. 1.21. The model assumes that, when a metastable atom comes into contact with a wall it returns to the ground state.

1.4.1 Model settings

Due to the symmetry of the system we study a 2D axisymmetric section, showed in fig. 1.4. The 3D plots are obtained by rotating the 2D simulation. The power of the coil is P= 500 W, and it is driven at a frequency of 13.56 MHz. The pressure is 10 milliTorr. The initial temperature is set to 300 K. The same temperature is set for the wafer support. The inlet temperature of Argon and Silane is 300 K. The simulation uses a frequency-transient approach, with a direct solver. This choice takes into account the effect of the electromagnetic forces without the need of solving it in time, saving computational resources. The simulation starts with a variable timestep till the first second and then with a constant timestep of 1 second until one minute. The use of this variable time step is due to the particular timescale of the

plasma. It is important to have a very small time-step in the early stage of the simulations, while after the saturation process it is possible to increase substantially the integration timestep. We performed our experiments with a PlasmalabSystem100 of the Oxford Instruments installed in the Consiglio Nazionale delle Ricerche (CNR) Istituto per la Microelettronica e Microsistemi (IMM) laboratory. The machine inspection and relative measurement of the different parts made possible to align the CAD reported in fig. 1.4 to the real instrumentation.

1.5 Simulation results

In this section we will present the plasma simulation details, discussing, with the aid of 3D complex plots, the space dependency of the main components of the plasma in the reaction chamber. Figure 1.3 shows a 3D image of the plasma reactor. The colored part represents the plasma region, the color scale depends on the mass fraction of silane that is higher in the region where it enters in the chamber. Colored curves represent the iso-temperature curves in terms of gas temperature, which is higher in the central part of the reactor. The arrows show the fluid flow. The black wire-frame represents the coils as circles, the shield and the other structural parts. The Ar is injected homogeneously from the top of the reactor (region indicated by the letter A). The SiH_4 enters in the chamber through a perforated conduit located in the lower part of the reactor which is indicated by the letter B. The wafer, i.e. the zone where the surface equations are different due to the material deposition, is indicated with a blue line in the bottom.

Figure 1.4 shows an axial-symmetric section of the plasma reactor, with the colored part representing the electron density and the colored lines representing the iso-temperature lines in terms of electron temperature. The black wireframe represents the coils as circles, and the other structural part. While the maximum electron temperature is near the coils, i.e. near the external wall of the chamber, the maximum electron density is in the core of the chamber. This spatial difference is due to the fact that the electrons that make collisions with the external walls are absorbed and correspondingly (in order to maintain locally the neutrality) the ionized atom returns in a ground state, see table 1.2 reactions 3-7. The gas temperature reaches its maximum value in a region slightly lower with respect to the maximum of the electron temperature. As cited, Argon enters from the top (A in the figure) at room temperature (300 K). Afterwards it is heated up by the plasma reactions and the space dependency of its temperature becomes similar to the global gas, indicating that in this region, the high temperature species are dominated by Argon. The gas temperature decreases in correspondence of the central zone, due to the lower reaction rate in the plasma. The gas temperature close to the wafer is below 330 K, which confirms that our machine can op-

erate at very low temperatures (e.g. the temperature of interest for treating a thermally sensitive materials, like plastics). The fluid flow is fast in the reaction chamber, due to the high temperature, and zero close to the walls. Before hitting the wafer, the flow is constrained to pass through a couple of holes and we can observe a local increase of the speed in this region. When the ionized gas reaches the lower chamber, it mixes with silane coming from the separate inlet (B) and then the mixed components exit from the chamber from the outflow channel. Figure 1.3 shows the presence of silane in the reactor. Despite the fact that the inlet is positioned in the lower part of the chamber, the silane reaches the upper reaction chamber with a quite high value in fraction, also due to the relatively small input flow rate of Argon with respect to that of SiH_4 (1 sccm of Ar and 20 sccm of SiH_4).

Figure 1.5 shows the growth-rate on the wafer for t=1 s of process (0 is the center of the wafer) and we can consider a constant angular distribution (cylindrical symmetry). The profile grows radially due to the peculiar fluid flow characteristics implemented in our machine, provoked by the presence of the holes in the external part of the control ring. In fig. 1.6 we report the height of deposited film in the wafer in false color and using an enhanced scale for t=1 s. In fig. 1.7 we plot the height of the film at different time steps. For every time step there is a uniform local increase in the deposited height, i.e. the simulated local deposition rate is constant, whilst the point to point variations explain the variation of the thickness of the deposited film at the wafer scale. We have compared the simulation results with experimental measurements of the deposition rate and the results are in agreement with the ones reported in [6].

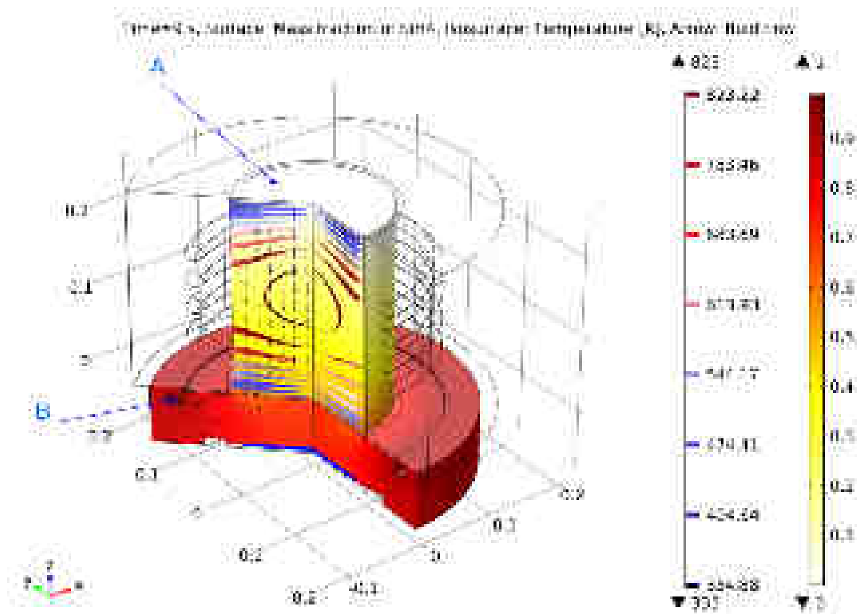

Figure 1.3: *3D image of the simulated reactor at t=9s. The Argon inlet is indicated with letter A, while the letter B indicates the inlet of the Silane. The black line defines the structure of the equipment, with the external shield and the inner coils. The blue line in the bottom indicates the wafer zone. The color domain represents the mass fraction of SiH_4, larger in the bottom part where the Silane inlet is located. The contour lines represent the gas temperature (K). The arrow indicates the gas flow.*

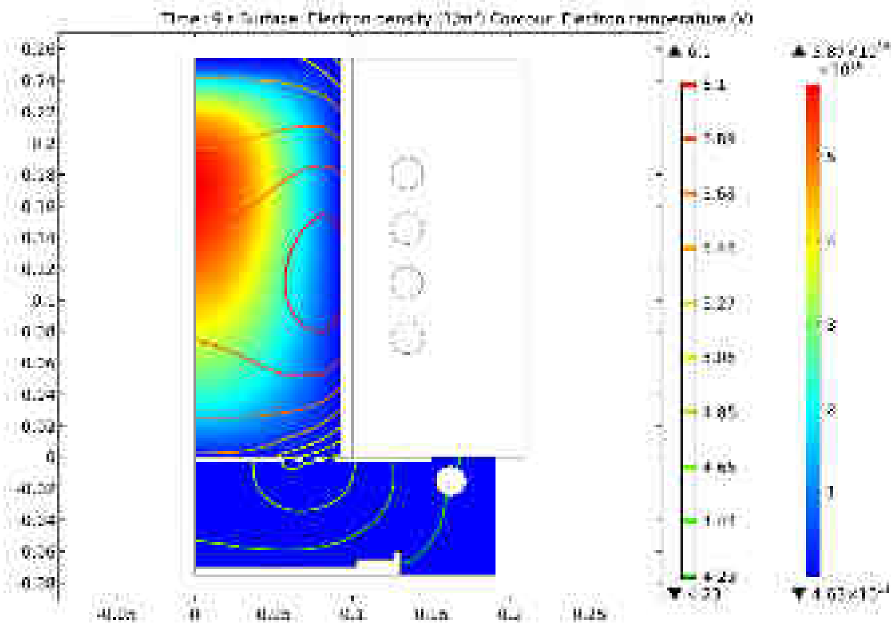

Figure 1.4: *A 2D section of the reactor showing in black the structure of the reactor. In color the electron density [m^{-3}] unit showing a maximum in the core of the reactor. The lines represent the electron temperature [eV], larger close to the coils.*

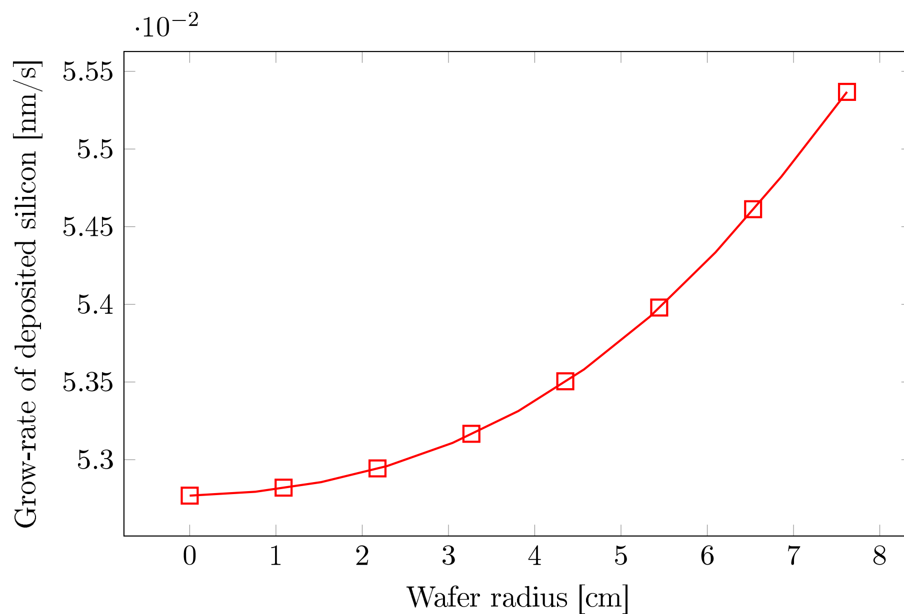

Figure 1.5: *Radially dependent grow rate at t=1 s*

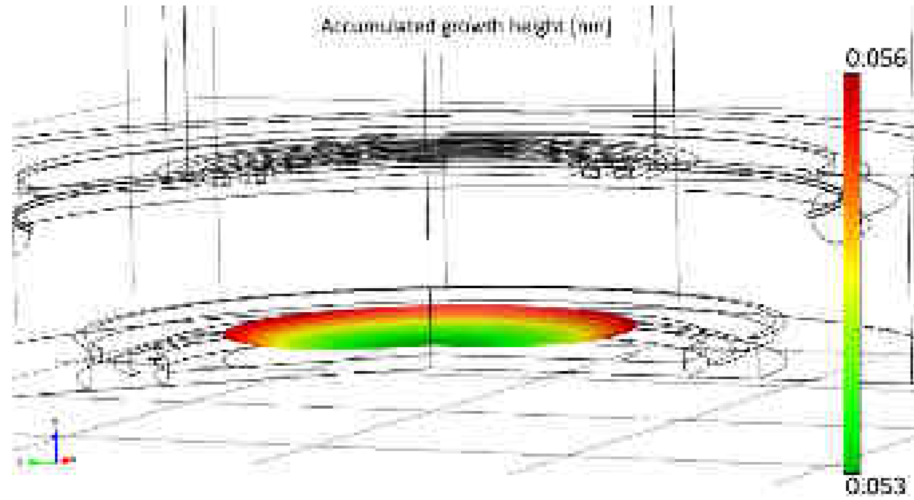

Figure 1.6: *3D views of the deposited film at t=1 s, with false color and not in scale. In black the contour of the chamber. The higher value of the deposited film is in correspondence with the position disc holes and in the proximity of the gas outflow.*

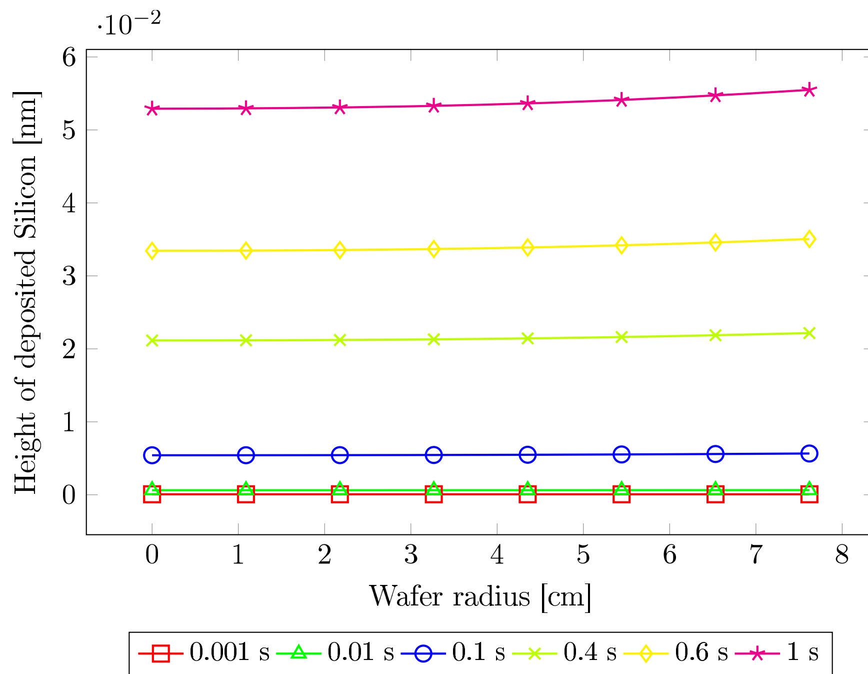

Figure 1.7: *The radially dependent height of the deposited film along the radial coordinate at various timesteps, which is radially dependent.*

1.6 Feature size simulation

In this section we propose a **coupled** approach to solve a different plasma problem. In the case of dry etching, we are also interested in the process results at the micro-scale, due to the nano-scale patterning of the processed structure. As a consequence, we have two different models, a plasma global model and an originally developed Kinetic Monte Carlo (KMC) etching model. The first one simulates the plasma state, in this case a HBr/O_2 one, neglecting the complexity of calculating spatial gradients of plasma parameters within the reactor chamber, solving a zero-dimensional model that requires low computational results. The KMC model studies the interaction of the plasma with the surface, at the nano-structural scale using the plasma parameters predicted by plasma simulations as an input of the etch-process model. In order to implement our model, we used the assumptions and equations of the global model presented by Lieberman et al. [7], adapting them to a particular plasma chemistry which includes in the set of (0D) rate equations for the average quantities in the chamber also the gas pumping and the electromagnetic energy balance. The global model was then combined with a Monte Carlo algorithm based on the numerical formulation of Chiaramonte et al. [8]. Full work is reported in our paper Ref. [9].

This plasma model does not contain the 3D analysis because we will use an industrial equipment for the comparison of the results (access to the machine component is not allowed due to confidentiality agreement). As a consequence, here we propose only the zero-dimensional model and the simulation results are comparable with the experimental ones only in the central part of the wafer, where, in turn, uniformity of the process is guaranteed by the precise manufacturing control.

V_{bias} [V]	O_2 [sccm]	HBr [sccm]	TCP [W]	I_{sat} $\left[\frac{mA}{cm^2}\right]$
149.35	7.0053	100.05	863.36	0.273
149.41	7.0055	99.98	776.10	0.244
149.25	7.0035	99.94	949.91	0.313

Table 1.5: *Design of Experiments: control parameter variations and related measured values of the saturation current. The DOE central point value is reported in the first row.*

1.6.1 Experiments

We have considered a plasma etching process applied to fabricate isolation trenches in Complementary Metal Oxide Semiconductor (CMOS) devices. The experiments consisted in the fabrication of a series of patterned samples, where trenches with a periodic pitch of $\sim$ tens of nanometers are exposed to a plasma process changing one by one the main control parameters. Post processed samples have been analyzed by SEM analysis in cross section configuration. We used a Transformer Coupled Plasma (TCP), confined in a cylindrical chamber of radius R and length L, excited by means of a radio frequency (RF) power at 13.56 MHz supplied to the TCP coil. The TCP chamber used is the LAM model 2300 Versys Kiyo 45. A voltage V_{bias} was supplied to the bottom electrode of the TCP in order to control the ion energy. The chamber temperature was set to 60 °C and the work pressure was 12 mTorr. A sub-set of the control parameter variations is reported in table 1.5, describing the so called Design of Experiments (DOE).

The variation of the top electrode power, modifying the rate of energy transferred from the coil to the plasma, affects all the plasma components. Only by coupling the plasma simulation at the reactor scale with the feature size simulations, we can obtain reliable results.

The comparison between the SEM sections and the simulated profiles is shown in fig. 1.9, and the code predicts correctly the effect of process parameter variations on the vertical etch rate and the profile shape. The SEM analysis evidences a strong effect of the power variation on the vertical etch rate. This fact is consistent with the sensor data indicating an important variation of 10% for the saturation current (see table 1.5).

The comparison of the SEM cross section and the simulation, confirms the predictive capability of the code, shown in fig. 1.10 where we use a double time process.

Changing the geometrical shape, see fig. 1.11 where we compare the already discussed geometry on the left with the one obtained in trenches with a smaller pitch, leads to a change in the simulation results in spite of the same setting for the process (central point of the DOE). In this case, we can see a different shape in the trenches and a slightly global etch depth.

We underline that experimental as well as simulation results have a non-linear dependence on both the equipment parameters and the geometrical constrains. When considering a planar structure, the evolution of the system is quite straightforward. The local growth rate is globally equal, the topology remains constant and the evolution does not create additional prediction issues, which has no variation in topology, In a structured sample, each profile point has a different visibility angle with respect to the incident plasma components. The etching or the deposition rate depends, not only on the process parameters, but also on the local shape of the profile. If we consider the process and its evolution, the shape changes over time, and therefore

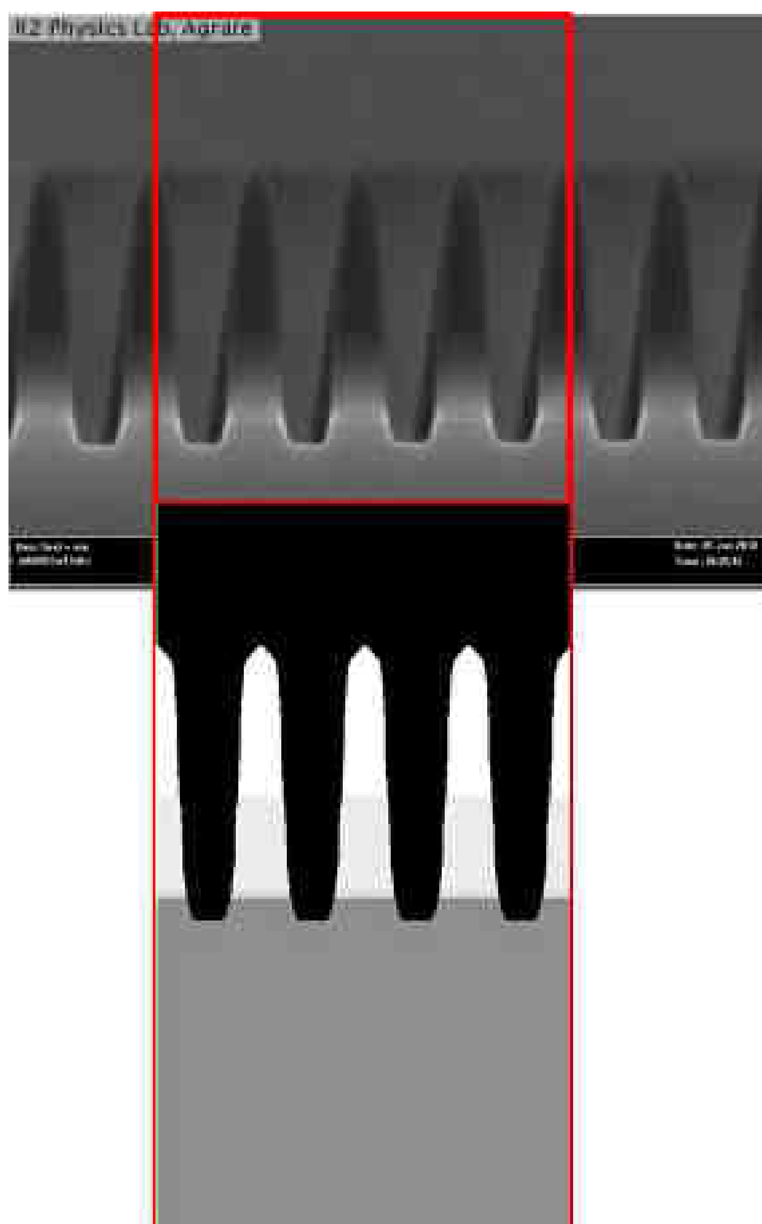

Figure 1.8: *Setting of the computational box: the SEM analysis (top) is mapped in the simulation box using a pixel interpolation technique. The imported structure reproduces all the different materials (from the bottom): silicon, two layers composing the hard-mask and the residual resist material.*

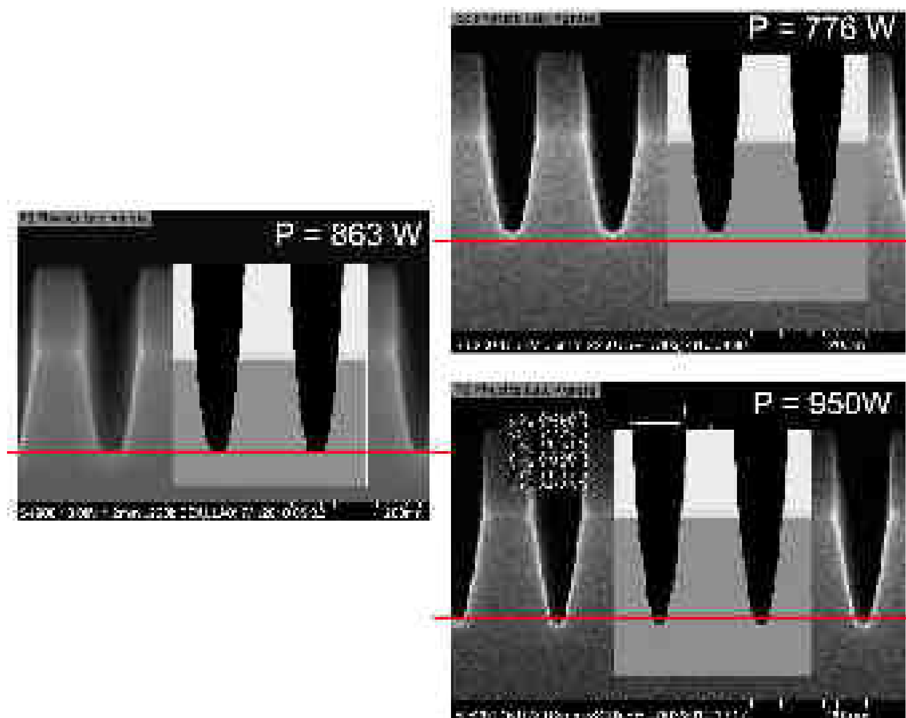

Figure 1.9: *Comparison between simulation results (foreground) and SEM images (background) for different applied powers. The code predicts correctly the effect of power variation on the vertical etch rate and the profile shape. For each image, the red line is positioned at the maximum depth of the trench with respect to the DOE central point case.*

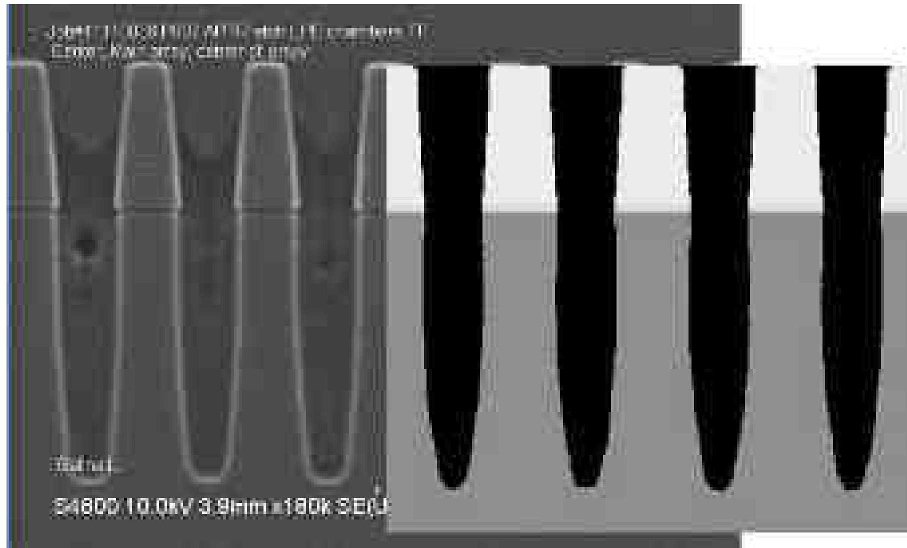

Figure 1.10: *Comparison between simulation results (foreground) and SEM images (background) by doubling the process time. The code correctly predicts the depth of etching.*

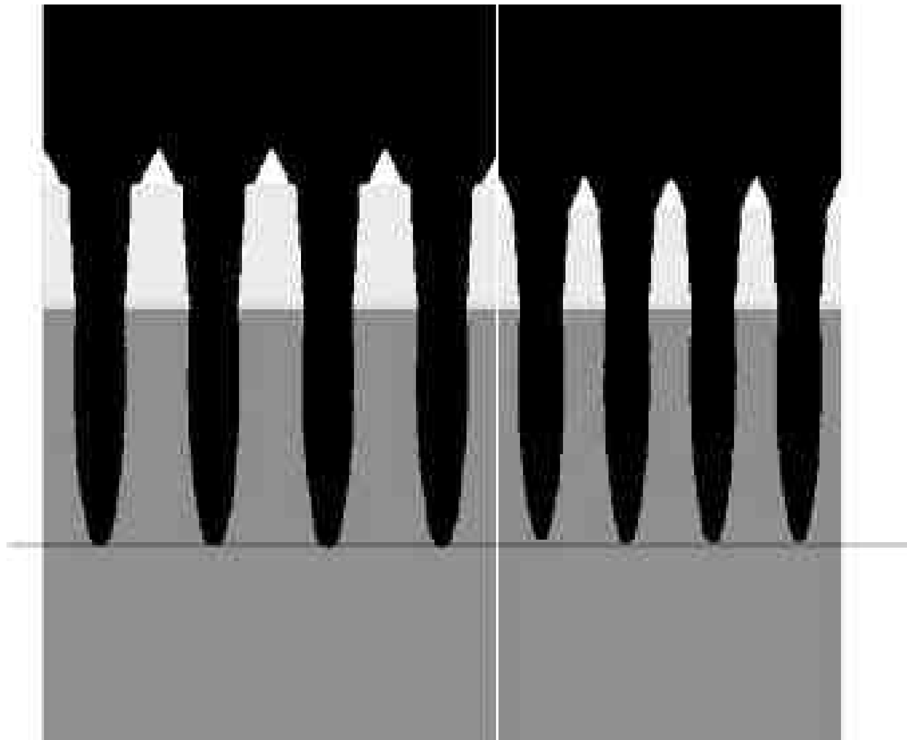

Figure 1.11: *A comparison of the already seen geometry (on the left panel) with a thinner one (on the right). The changes in geometry modified non linearly the results. The erosion of the resist is higher in the thinner geometry.*

the interaction of the device with a patterned sample is both space and time dependent. These considerations lead to the need of using a simulator capable of simulating both the in-bulk plasma and the corresponding surface response at the device feature size.

Another, more complex and accurate extension of the simulation approach could be to use the ion/particle distribution that comes out from an equipment scale simulation, combined with a corresponding particle energy distribution calculated with a Monte Carlo plasma simulation. This approach should allow to transfer more and accurate information between the codes operating at the two scales.

1.7 Conclusion

In this chapter we discussed the technological value of plasma processes and the need for simulation tools to control their complexity. In particular, the ability to process low temperature samples with excellent yields is one of the major attractions to this type of equipment, for example for plastic applications or flexible media. The great difficulty of plasma processes is the spatial difference between input and output which requires a multiscale approach. Typical process parameters belong to macroscopic nature (pressure, initial temperature, species involved, etc.) but the required results are on micro-nanoscopic scale, and their binding, as seen in this chapter, is not based on a simple understanding. Our aim was to be able to connect machine parameters with desired results using originally developed tools. To achieve this goal, we have to analyze an extremely complex, non-equilibrium process where a huge number of reactions takes place, which must be modeled in the best possible way, taking into account not only the correctness but also the computational availability. To complete a correct simulation, the study of thermo-fluidodynamics should also be added as the reaction rates can depend on the local temperature and on the spatial distribution of the species involved. In view of these features in the literature, different approaches have been proposed, each adapted to particular categories of plasma equipment. We have shown two possible approaches, the first applied to a PE-CVD process with an ICP reactor with the **fluid** approach, while the second using a TCP reactor with the **coupled** approach. The first study focused on the correct spatial, electromagnetic, thermal, fluid and chemical analysis of a plasma reactor. In this case, macroscopic information was obtained on the condition of the desired structures at the wafer level treated. The second has shown that not only input parameters influence geometry, but also the initial geometry and evolution of the process are important. In both cases, in addition to having a good agreement with the experiments, the importance of using simulations to study such complex processes has emerged, thus reducing trial experiments or alternative recipes in order to

optimize production processes.

2

Laser annealing modeling

2.1 Introduction

Laser Annealing (LA) is the preferred material processing option when local heating in the tens of nm range of the sample is required. As a consequence it can be applied when a local material modification has to be activated at high temperature (T), when this high T could be detrimental for the materials and structures present in the surrounding areas. In semiconductor technologies, the importance of LA increases with the complexity of the realized/proposed integration scheme, which nowadays includes also 3D integration where additional device structures have to be built on top of pre-fabricated ones (see ref. [10] for a complete discussion on LA applications in emerging technologies).

In many of these applications LA is preceded by a process (e.g. impurity implantation or low temperature deposition) producing a strongly disordered or amorphous material. Moreover, for the majority of the proposed conditions, LA induces localized melting and the ultra fast recovery of the crystalline order. As a consequence, a key aspect of the material modifications caused by LA is the strong non-equilibrium kinetics which is often exploited to obtain the desired results: e.g. the non-equilibrium impurity segregation during the fast solidification favors the incorporation of high concentrations of electrically active dopant atoms [11–13]. This non-equilibrium kinetics affect also locally the optical parameters of the sample and the absorbed electromagnetic energy density consistently changes. As a consequence the predictive control of the process is extremely complicated without the aid of computational tools, which virtually reproduce all this complex phenomenology including also other particular anomalous aspects in terms of redistribution of materials components (see e.g. refs.[10, 14–21]).

The scope of this chapter is the introduction of the complete formalism needed for the simulation of laser annealing for the case of pulsed laser

sources. The mathematical aspects will be accompanied by numerical results to discuss model features and benchmarks of the developed computational tools for their validation. Planar systems in 1D and 2D will be considered for this study.

2.2 Theoretical background

In contrast to other thermal process, LA results depend critically on the interaction between equipment and specimen. Indeed, the absorption of the laser-beam, i.e. the driving force for the material modifications, depends strongly on the sample's geometry and material type, due to the impact of the laser light diffraction and thermal diffusion within the irradiated structure [12, 13]. The accurate modeling of the micro-structural kinetics during LA can not be developed without the precise determination of the thermal field and the eventual melting front kinetics. In this section we will discuss the simulation formalism based on electromagnetic calculations coupled with a kinetic model for the evolving temperature and phase fields.

2.2.1 Electromagnetic calculations for the heat sources in laser-annealing

In laser annealing, using pulsed laser configurations, the spatial distribution of the electromagnetic (E.M.) power can be considered uniform over areas $\sim$ cm ^{2}. The coherence length L_c of the E.M. field is in general much smaller than the pulse dimension $L_c << 1$ cm but much larger than the feature size (e.g. the pitch $\sim 10^{-8} - 10^{-7}$ cm, for the case of a periodic pattern of devices) of the irradiated structures. As a consequence, the heat source can be approximated as the one generated by a generic incident coherent electromagnetic plane wave with fixed angular frequency ω in a given polarization state. The laser pulse is usually specified in terms of the total fluence (energy density) E_{laser} in [J/cm^2] units and the normalized power density $P_{norm}(t)$

$$\int_0^{\Delta t_{pulse}} P_{norm}(t)dt = 1 \tag{2.1}$$

where $P_{norm}(t) \equiv 0$ when $t < 0$ or $t > \Delta t$. The time dependencies of the laser pulse that can be generated by the experimental equipment Laser Annealer LT-3000/3100 produced by **SCREEN Semiconductor Solutions Co.- Laser Systems & Solutions of Europe(LASSE)** considered in our analysis are reported in fig. 2.1. Please note that the curves are normalized, i.e the area under the curves is equal to 1.

The pulse duration Δt_{pulse} is usually much larger than the inverse of the frequency

$$\nu^{-1} = \left(\frac{\omega}{2\pi}\right)^{-1} = \left(\frac{c}{\lambda}\right)^{-1}, \tag{2.2}$$

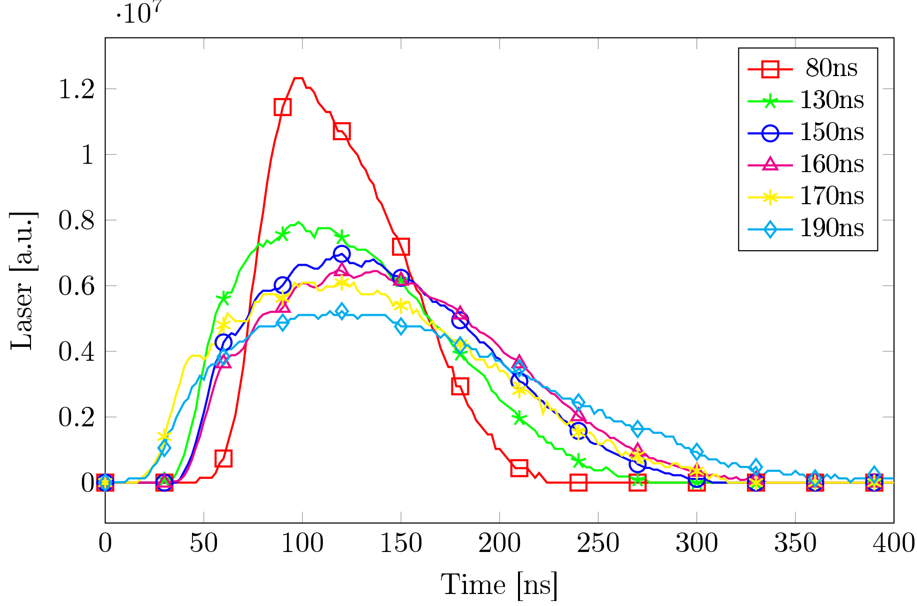

Figure 2.1: *Different pulse normalized shapes measured in the laser equipment used to irradiate the experimental samples studied in this PhD thesis.*

where ω is the angular frequency and c is the light speed. For example for a laser wave length $\lambda = 308 \times 10^{-9}$ m the inverse of the frequency is $\nu^{-1} = 308 \times 10^{-9}/299792458 \sim 10^{-15}$ s while the usual range of Δt_{pulse} is 20-200$\times 10^{-9}$ s. These considerations make ineffective any fully time dependent solution of the Maxwell equations for the heat source calculations in the case of the LA problem under study. An "adiabatic-like" formulation of the heating problem is necessary, assuming that the change of the optical constants during the annealing is slow with respect to the system response to the electromagnetic excitation. In this approximation, with the additional assumption that the electromagnetic excitation is efficiently transferred from the electrons to the photons (see ref. [19] for a complete discussion on this issue) we can determine the heat sources using a stationary (or time-harmonic) evaluation of the resistive heat averaging the "ultra-fast" time scales of the oscillating electromagnetic field

$$S_{laser}(t, \mathbf{r}) = \frac{\varepsilon''}{2\rho} |\mathbf{E}^{th}(\mathbf{r})|^2 \cdot P_{norm}(t) \qquad (2.3)$$

where ε'' is the imaginary part of the complex dielectric constant $\varepsilon = \varepsilon' + j\varepsilon''$ of the material and $\mathbf{E}^{th}$ is the time-harmonic electric field $\mathbf{E} = \mathbf{E}^{th} \times \exp(-j\omega t + \phi)$ that can be evaluated by the following time independent form (i.e. the time-harmonic Maxwell curl-curl problem)

$$\nabla \times (\boldsymbol{\mu}^{-1} \nabla \times \mathbf{E}^{th}) - j\omega(\boldsymbol{\sigma} - j\omega")\mathbf{E}^{th} = j\omega \mathbf{J}, \qquad \text{in } \Omega \qquad (2.4)$$

and

$$\mathbf{n} \times \mathbf{E}^{th} = \mathbf{n} \times \mathbf{E_0}^{th}, \qquad \text{on } \partial\Omega_e \tag{2.5}$$

$$\mathbf{n} \times (\boldsymbol{\mu}^{-1}\nabla \times \mathbf{E}^{th}) + j\omega\mathbf{n} \times (\boldsymbol{\lambda}(\mathbf{n} \times \mathbf{E}^{th})) = j\omega\mathbf{J_f} + j\omega\mathbf{n} \times \mathbf{H_0}, \quad \text{on } \partial\Omega_h \tag{2.6}$$

where

$$\partial\Omega = \partial\Omega_e \cap \partial\Omega_h \tag{2.7}$$

and

$$\partial\Omega_e \cup \partial\Omega_h = 0 \tag{2.8}$$

here $\Omega \subset \mathbb{R}^d$ (d is the system dimension) is an open, bounded domain with boundary $\Gamma = \partial\Omega$, $\partial\Omega_e$ ($\partial\Omega_h$) is a boundary where a condition on the electric (magnetic) field is imposed, $\mathbf{J} \in (L^2(\Omega))^d$ is a given vector function indicating the internal source and $\omega \in \mathbb{R}(\omega \neq 0)$ $\mathbf{n}$, is the unit outward normal vector to $\partial\Omega$.

$$\mathbf{E}^{th} = E_z^{th}\mathbf{z} \tag{2.9}$$

$$\frac{\partial E_z^{th}}{\partial z} = 0 \tag{2.10}$$

and eq. 2.5 takes the form of the Helmotz equation

$$-\nabla(\boldsymbol{\mu}^{-1}\nabla E_z^{th}) - j\omega(\boldsymbol{\sigma} - j\omega\boldsymbol{\epsilon})E_z^{th} = 0 \tag{2.11}$$

and

$$E_z^{th} = E_0^{th} \qquad \text{on } \partial\Omega_e \tag{2.12}$$

$$-\mathbf{n} \cdot \nabla E_z^{th} - jkE_z^{th} = +j\omega\mathbf{n} \times \mathbf{H_0}. \qquad \text{on } \partial\Omega_h \tag{2.13}$$

Since the optical parameters depend significantly on temperature and phase, eqs. 2.3 and 2.11 have to be solved self-consistently with the phase and temperature evolution equations (see the following section) to evaluate the time and space dependent heat sources.

2.3 Front tracking methods

A process that induces melting, which is commonly ruled by the heat equation, has to be computed considering also the latent heat release/absorption. This is a problem with a moving boundary, i.e. the liquid/solid front (tracked by the $T = T_M$ relation for the temperature field, where T_M is the melting temperature) it is also known as Stefan problem, since Stefan was the first that treated the ice-melting example [22]. The front tracking methods consider the interface between phases as a variable of the problem to be determined. In the following part we describe the formalism for the solid-liquid transformation case.

Without loss of generality, let us consider a one dimensional (1D) fixed domain $[0, l]$ and set the interface at distance $s(t)$. In this condition we have one pure liquid domain in $[0, s(t)]$ and one pure solid one in $[s(t), l]$. The temperature in the point x at time t is defined by $T(x,t)$. As we said before for each domain the heat equation is valid:

$$\begin{cases} \frac{\partial T}{\partial t}(x,t) = \frac{\partial}{\partial x}\left(D_{liq}\frac{\partial u}{\partial x}\right) & x \in \Omega_{liq} \\ \\ \frac{\partial T}{\partial t}(x,t) = \frac{\partial}{\partial x}\left(D_{sol}\frac{\partial u}{\partial x}\right) & x \in \Omega_{sol} \end{cases} \tag{2.14}$$

where D_{liq} and D_{sol} represent the thermal diffusivity in the liquid and the solid, respectively, which involve the heat capacity, heat conduction and density coefficient of the materials. The boundary motion is ruled by the additional constrain

$$LV = D_{sol}\frac{\partial T}{\partial x}(x,t)|_{x\downarrow s(t)} - D_{liq}\frac{\partial T}{\partial x}(x,t)|_{x\uparrow s(t)} \tag{2.15}$$

with L the latent heat. If the position of the interface s is a differentiable function, the velocity of the interface V can be replaced by

$$L\frac{\partial s}{\partial t}(t) = D_{sol}\frac{\partial T}{\partial x}(x,t)|_{x\downarrow s(t)} - D_{liq}\frac{\partial T}{\partial x}(x,t)|_{x\uparrow s(t)} \tag{2.16}$$

As we said before, the interface is tracked by the $T(x,t) = T_M$ relationship. In spite of the straightforward definition, the Stefan problem is difficult to translate in a reliable computational formalism, especially due to the difficult front tracking in 2D and 3D systems. In the following section we will discuss some methods used for the melting front tracking, which incorporate the front evolution in a set of numerically affordable partial differential equations.

2.3.1 Enthalpy method

C_p is the heat capacity or thermal capacity at constant pressure equal to the ratio of the heat added to (or removed from) an object to the resulting temperature change. Within the so called "Enthalpy" method we introduce a modified C_p function that takes into account also the heat absorbed (released) by the phase changes. The jump discontinuity of the modified C_p function in the transition zone is essential to know the position of the interface itself. In the following part we will show the formulation of the enthalpy method in a case of heating-melting problem [23].

The heat equation can be formally written as energy conservation law in terms of the (volumetric) enthalpy H:

$$\partial_t H + \nabla \cdot \overrightarrow{Q} = S \tag{2.17}$$

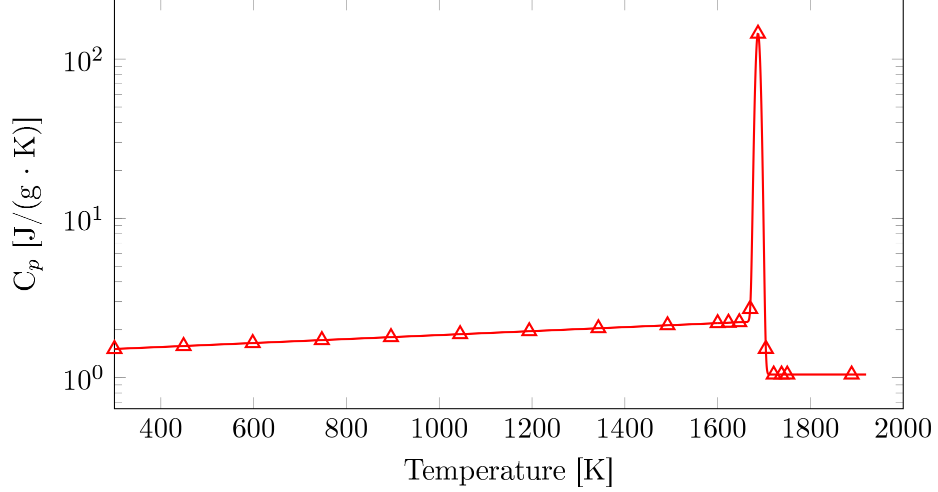

Figure 2.2: *Phase and temperature dependent $\widetilde{C_p}$ used in the enthalpy model for Silicon. On the left part there is the C_p of the crystalline phase that is clearly dependent from temperature. Near the T_M there is the spike of the gaussian shape that represents the heat exchanged during the "phase change". Above T_M there is the C_p of the liquid phase that is constant. The shape of the peak depends on L_f and ΔT.*

where $\overrightarrow{Q}$ is the heat flux and S the heat source.

This law allows to find the heat and phase changes, since in the enthalpy formulation the latent heat is also included. However, this equation has to be coupled with an appropriate equation for relating H and T.

We consider the formulation $H = \rho h$ where H is the enthalpy per unit of volume, ρ is the density, and h is the enthalpy for unit of mass. The value h_{ref}, and so (thus also) $H_{ref} = \rho^S h_{ref}$ that is the enthalpy at the reference state can be arbitrary. With this construction the heat capacity is strictly positive, $\Delta H^{melting} = L$ is also positive and the dependence of H on T is monotonic (with a jump at the melting point) and this means that T can be found by inverting the $H(T)$ relationship. Anyhow an even more convenient "Enthalpy" method can be implemented incorporating the latent heat change in the C_p function of T. Indeed the finite jump of H should include a $L \times \delta(T - T_M)$ term in the heat capacity (where $\delta(T)$ is the Dirac δ function). This term can be suitably approximated by a Gaussian with a finite range of variation (instead of the infinitesimal variation range of the delta function) whilst the integral value (i.e. the enphalpy itself) does not vary. As a consequence the $C_p(T)$ function reads:

$$\widetilde{C_p} = C_p(T) + \frac{1}{\Delta T\sqrt{\pi}} e^{\dfrac{-(T - T_M)}{\Delta T^2}} L_f \tag{2.18}$$

with T_M the melting point, L_f the latent heat of fusion and ΔT a nu-

merical parameter that sets the width of the gaussian (the phase transition region). This last parameter is the only one that the user can set and should be as smaller as possible in order to compute correctly the phase change. However, also the numerical constrains have to be considered, since higher values usually ensure better numerical convergence. In fig. 2.2 we show the $\widetilde{C_p}$ for the Silicon material. Note that for improving the graphical representation, the curve in the figure is plotted with $\Delta T = 5$ K whilst in our simulation the value $\Delta T = 0.5$ K is used.

2.3.2 Phase Field Formalism

Another front tracking method used in our simulations is based on the phase field which has an additional advantage with respect to the "Enthalpy method", since the curvature energy cost can be correctly computed. The phase field method introduces a new thermodynamic variable, $\psi(x,t)$, that represents the phase of the system. In particular the variable varies smoothly from one value in one phase to another value in the other phase, with an interface region of thickness W [m]. The domain of different phases (i.e. the ψ function) can vary in time and space. The phase field permits also natural integration of evolution models for other quantities of interest (e.g. impurities, defects). For this reason an equivalent phase function has been implemented in our code also when the "Enthalpy method" is activated. As a consequence, the rest of the tool is substantially similar for the two approaches. An accurate mathematical phase field model derivation, including extended analytical and numerical tests, can be found in the seminal work of Karma and Rappel (K-R) [24], based on the following phase field equations for a generic temperature T driven solid-liquid phase transition:

$$\tau \frac{\partial \psi}{\partial t} = W^2 \nabla^2 \psi - \frac{\partial F(\psi, \lambda u)}{\partial \psi}, \tag{2.19}$$

$$\frac{\partial u}{\partial t} = D_T \nabla^2 u + \frac{1}{2} \frac{\partial h(\psi)}{\partial t} \tag{2.20}$$

where

$$F(\psi, \lambda u) = f(\psi) + \lambda g(\psi) u \tag{2.21}$$

and

$$u = \frac{c_p (T - T_M)}{L}. \tag{2.22}$$

The following parameters are introduced: W is the (finite) width of the liquid-solid interface, D_T is the heat diffusivity, c_p the constant pressure specific heat and L the latent heat. Here $F(\psi, \lambda u)$ and h must be chosen in a way that the diffuse interface solutions coincide with the free boundary

problem in the sharp interface limit.

$$\begin{aligned}
&\frac{\partial u}{\partial t} = D_T \nabla^2 u \\
&V = D_T \left(\partial_n u|^- - \partial_n u|^+ \right) \\
&u_i = -\frac{d_0}{R} - \beta V
\end{aligned} \tag{2.23}$$

where d_0 is the capillarity length and β is the kinetic coefficient which relates the local interface temperature T to the local interface speed. K-R propose a double-well function with minima at $\phi = -1$ (liquid) and $\phi = +1$ (solid) using the following expressions for $f,\ g,\ h$

$$f(\psi) = -\frac{\psi^2}{2} + \frac{\psi^4}{4} \tag{2.24}$$

$$g(\psi) = \psi - \frac{2\psi^3}{3} + \frac{\psi^5}{5} \tag{2.25}$$

$$h(\psi) = \frac{15}{8}\left[\psi - \frac{2\psi^3}{3} + \frac{\psi^5}{5}\right] \tag{2.26}$$

where the variational choice $h(\psi) \propto g(\psi)$ and the additional constraint

$$\frac{h(+1) - h(-1)}{2} = 1 \tag{2.27}$$

are imposed in order to guarantee that the correct amount of latent heat is produced/consumed at the moving interface. The sharp interface limit fixes the λ value in eq. 2.21 as the one satisfying the following equation

$$\beta = a_1 \left[\frac{\tau}{\lambda W} - a_2 \frac{W}{D_T}\right] \tag{2.28}$$

with $a_1 = 0.8839$ and $a_2 = 0.3981$ while $d_0 = a_1 W/\lambda$ [24]. Please note that a nonlinear relation between $V(T_i)$ and the moving interface temperature u_i (e.g. Fulcher-Vogel type expressions [12]) can be easily implemented deriving a function $\lambda[V(T_i)]$ from $\beta[V(T_i)]$ with the use of the eq. 2.28. In particular we consider the following expression for speed of the interface $V(T)$:

$$V = A \cdot \exp\left(\frac{-E_a}{k_b T}\right) \cdot \left[1 - \exp\left[\left(\frac{\rho L}{k_b N}\right) \times \left(\frac{1}{T_M} - \frac{1}{T}\right)\right]\right] \tag{2.29}$$

where A and E_a are material dependent parameters, k_b is the Boltzmann constant, ρ is the density and N is the atomic density. In fig. 2.3 we report

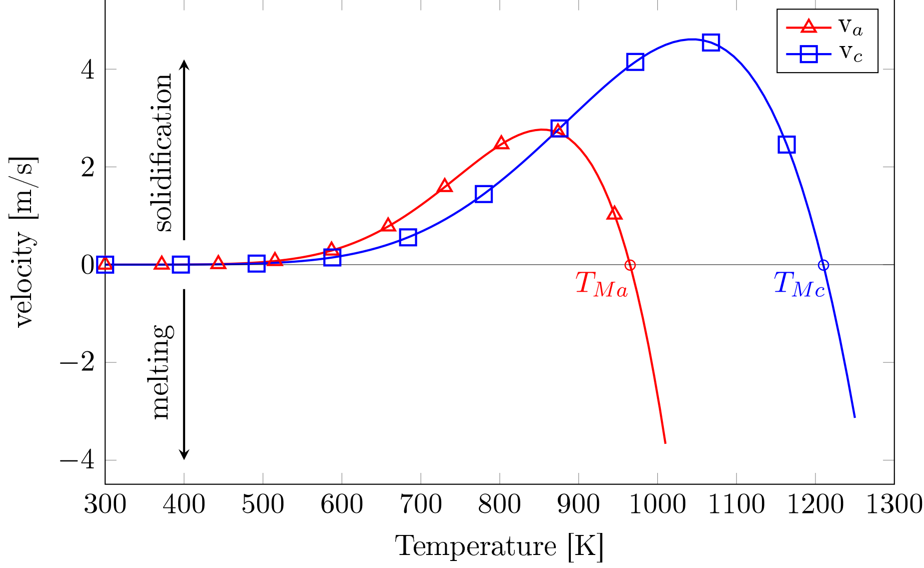

Figure 2.3: *Interface speed for amorphous (red line and triangles) and crystalline (blue line and squares) phases. The velocity reaches a 0 value in correspondence of the melting temperature of each phase.*

the interface speed for the amorphous (red line with triangles) and crystal (blue line with squares) germanium.

Thus, the explicit forms of eqs. 2.19 and 2.20 are

$$\begin{aligned} \tau \frac{\partial \psi}{\partial t} &= W^2 \nabla^2 \psi - \frac{\partial f}{\partial \psi} - \lambda u \frac{\partial g}{\partial \psi} \\ &= W^2 \nabla^2 \psi + \psi (1-\psi)(1+\psi) - \lambda u (1-\psi)^2 (1+\psi)^2 \end{aligned} \tag{2.30}$$

and

$$\begin{aligned} \frac{\partial u}{\partial t} &= D_T \nabla^2 u + \frac{1}{2} \frac{\partial h(\psi)}{\partial t} \\ &= D_T \nabla^2 u + \frac{15}{16} (1-\psi)^2 (1-\psi)^2 \frac{\partial \psi}{\partial t} \end{aligned} \tag{2.31}$$

or for the absolute temperature T

$$c_p \frac{\partial T}{\partial t} = K \nabla^2 T + L \frac{15}{16} (1-\psi)^2 (1-\psi)^2 \frac{\partial \psi}{\partial t} \tag{2.32}$$

where K is the heat conductivity. The material parameters used in the simulation are phase and temperature dependent:

$$\rho(\phi, T) = \theta(\phi) \rho_{sol}(T) + \theta(-\phi) \rho_{liq}(T) \tag{2.33}$$

$$C_p(\phi, T) = \theta(\phi) C_{psol}(T) + \theta(-\phi) C_{pliq}(T) \tag{2.34}$$

$$K(\phi, T) = \theta(\phi) K_{sol}(T) + \theta(-\phi) K_{liq}(T) \tag{2.35}$$

where the subscript *sol* or *liq* denotes the solid and the liquid phases, respectively.

2.3.3 Alternative phase field formulation

Equivalent phase field formulations can be found in the literature, which can be derived from the K-R one by means of transformation of the phase function. For example the phase field formalism of Wheeler et al. [11, 25] practically coincides to the K-R one when the transformation

$$\phi = \frac{\psi + 1}{2} \tag{2.36}$$

is performed in the previous equations. With this formulation the free energy function is defined in the $[0, 1]$ domain, and the pure phases are now defined in 0 and 1. With this formulation we obtain

$$-\frac{\partial f}{\partial \psi} = 4\phi(1 - 2\phi)(1 - \phi) = -\frac{\partial \widetilde{f}}{\partial \phi} \tag{2.37}$$

$$-\frac{\partial g}{\partial \psi} = -16\phi^2 (1 - \phi)^2 = -\frac{\partial \widetilde{g}}{\partial \phi} \tag{2.38}$$

$$\frac{1}{2}\frac{\partial h(\psi)}{\partial t} = 30\phi^2 (1 - \phi)^2 \frac{\partial \phi}{\partial t} = \frac{1}{2}\frac{\partial \widetilde{h}(\phi)}{\partial t} \tag{2.39}$$

and

$$2\tau \frac{\partial \phi}{\partial t} = 2W^2 \nabla^2 \phi - \frac{\partial \widetilde{f}}{\partial \phi} - \lambda u \frac{\partial \widetilde{g}}{\partial \phi} \tag{2.40}$$

$$c_p \frac{\partial T}{\partial t} = D\nabla^2 T + L \frac{1}{2}\frac{\partial \widetilde{h}(\phi)}{\partial t} \tag{2.41}$$

which represents a phase field formulation which starts from a free energy density of the form

$$\widetilde{f}(\phi) = -\phi^2 (1 - \phi)^2 \tag{2.42}$$

and

$$\widetilde{g}(\phi) = 8\left(\frac{1}{3}\phi^3 - \frac{1}{2}\phi^4 + \frac{1}{5}\phi^5\right) \tag{2.43}$$

The melt thickness is usually very small so there is no relevant convective effect to be included. Thus the heat flux in the solid and liquid is due to heat conduction only, $\overrightarrow{Q} = -k\nabla T$, with k the thermal conductivity and T the temperature.

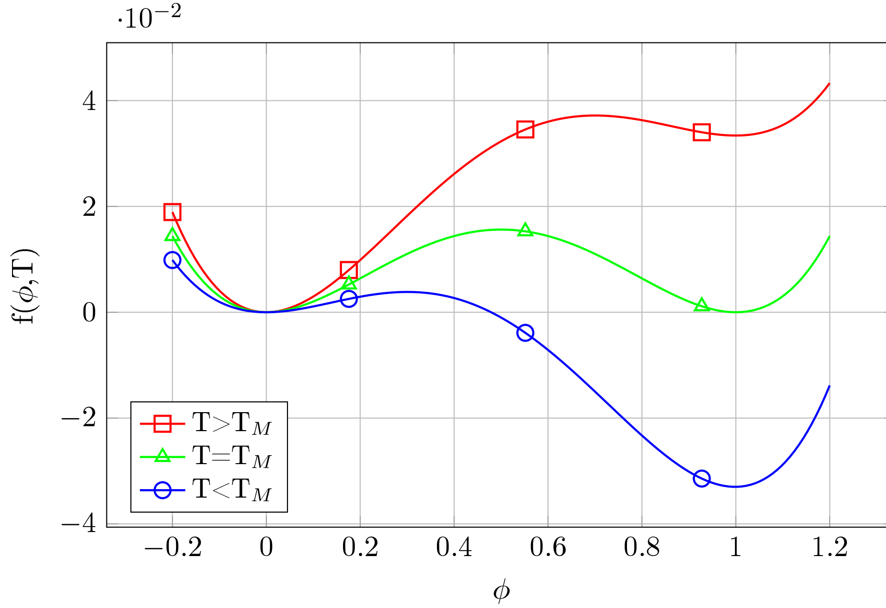

Figure 2.4: *The free-energy density $f(\phi, T)$, derived from [11], displayed as a function of ϕ for tree values of temperature near the melting temperature T_M: for $T < T_M$, $T = T_M$ and $T > T_M$.*

The phase field parameters (τ, W and λ) are chosen in order to correctly achieve the thin interface limit [24]. The phase field model calibration for parameters used in this work is equivalent to that reported in ref. [12].

All the material properties are phase and temperature dependent:

$$\rho\,(\phi, T) = \phi \cdot \rho_{sol}(T) + (1 - \phi) \cdot \rho_{liq}(T) \tag{2.44}$$

$$C_p\,(\phi, T) = \phi \cdot C_{psol}(T) + (1 - \phi) \cdot C_{pliq}(T) \tag{2.45}$$

$$K\,(\phi, T) = \phi \cdot K_{sol}(T) + (1 - \phi) \cdot K_{liq}(T) \tag{2.46}$$

2.4 Anomalous impurity redistribution during a melting LA process

Ultra fast melting and subsequent solidification, induced by pulsed laser irradiation of ion implanted semiconductor samples, promote concurrent non-equilibrium phenomena leading to a significant modification of the micro-state of these systems. In particular: the implantation damage is healed if the melting involves the whole implanted region, impurities redistribute due to the high diffusivity in the liquid state, the rapid crystallization traps a high density of impurities in (active) substitutional crystal sites. Although, this

complex kinetic evolution has been consistently modeled in several cases by integrating diffusion-segregation models in the phase field formalism [12, 25], the diffuse impurity chemical and active profiles show systematic anomalies that need additional theoretical refinements. In this section we present the formalism introduced in ref. [14] and implemented in our code to simulate impurity redistribution.

2.4.1 Phase field models of impurity trapping and full LA simulations

The kinetic states of diluted alloys in solid and liquid phases are completely different, whereas thermal fluctuations promote long range migration in the liquid phase whilst vibrations and related activated short range jumps rule atom redistribution in the solid phase. As a consequence, the impurity diffusion coefficient jumps many orders of magnitude (e.g. from $D_l \sim 10^{-4}$ to $D_s \sim 10^{-12}$ cm^2/s) from the liquid to the solid regions of an evolving solid-liquid system. The two phases are in contact during a solidification phenomenon and the solid-liquid interface marks a boundary between these regions where atoms dynamically transit between these two kinetic states, and the local alloy (impurity) density changes at the two sides of the interface. As a consequence, a fundamental parameter is the partition coefficient k^p defined as the ratio between the impurity density $k^p = c_s/c_l$ at the two sides of the interface. Phase field models show a strong potential for the accurate simulation of the non-equilibrium solute trapping.

In particular, anomalous peaks close to the melt depth region are systematically observed in shallow profiles of implanted Si-X and Ge-X (X = B, P and As) alloys after LA [15, 17, 26, 27]. The results obtained using both Fick's theory and the non-equilibrium trapping theory are not satisfactory. See in this regard the green curve of fig. 2.5 versus the green circles, which represent the experimental profile. The as implanted profile is represented by black circles. The inset shows the laser pulse used.

A particular model able to overcome this issue has been proposed in ref. [14], which does not involve the segregation behavior at the solid-liquid boundary and derives the anomalous redistribution of the impurities as an indirect effect of their diffusion mechanism in the liquid semiconductor. The underlying assumption on the basis of this diffusion mechanism is the presence of two states, with proper bonding configuration, for the solute atoms dissolved in the liquid semiconductor. These states, characterized by strongly different mobilities, are in a dynamic equilibrium ruled by the local temperature. The presence of more bonding configurations of the impurities is correlated to the atomic structures of l-Si and l-Ge [28–30] showing a mixed and fluctuating covalent and metallic bonding character: The state with low (high) diffusivity should locally trigger the formation of covalent (metallic) bonds for the surrounding Si atoms. The balance of these two components

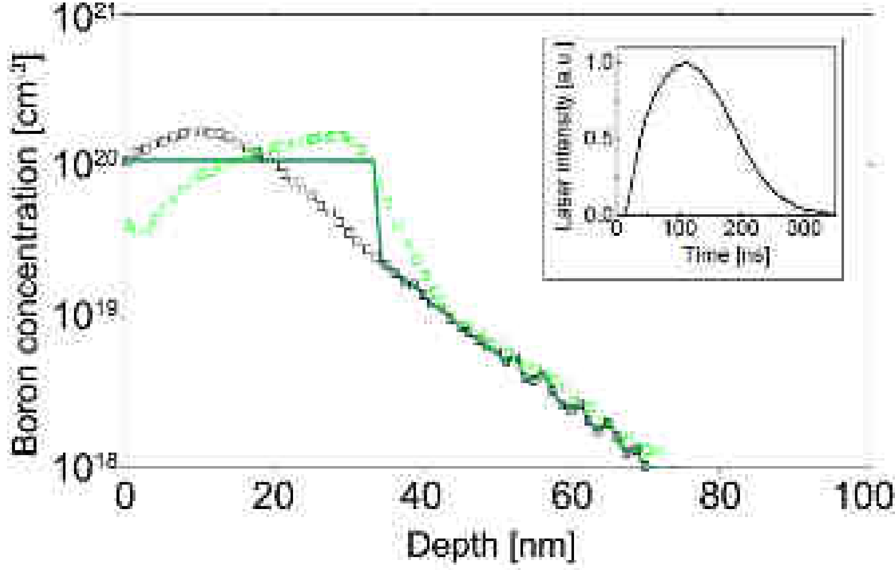

Figure 2.5: *SIMS (green squares) Boron profiles obtained after a post-implantation laser irradiation at 2.0 J/cm^2 (as implanted is shown as black squares). Simulation profile assuming $k^p = 1$ is shown as thick green lines. In the inset the laser pulse is plotted. Data from G. Fisicaro et al. ref. [14].*

of the solute density gives rise to a globally non-fickian diffusion of impurities in l-Si(Ge) which, as we are going to discuss, explains their anomalous redistribution. The diffusion model is formulated in terms of the following equations [14]:

$$\frac{\partial c}{\partial t} = \frac{\partial c^{HD}}{\partial t} + \frac{\partial c^{LD}}{\partial t} \tag{2.47}$$

$$\frac{\partial c^{HD}}{\partial t} = \nabla \left[D^{HD} \nabla c^{HD} \right] + k^{\tau} \left(c^{LD} - \bar{R} \cdot c^{HD} \right) \tag{2.48}$$

$$\frac{\partial c^{LD}}{\partial t} = \nabla \left[D^{LD} \nabla c^{LD} \right] - k^{\tau} \left(c^{LD} - \bar{R} \cdot c^{HD} \right) \tag{2.49}$$

where D^{HD} and D^{LD} are the impurity diffusivities in the higher and lower diffusivity state in liquid phase. c^{HD} and c^{LD} are the corresponding concentrations. $\bar{R}(T)$ is the average (equilibrium) ratio between low and high diffusivity states at constant T. Please note that for non-equilibrium processes the temperature in the liquid phase is not, in general, restricted to $T > T_m$. Molecular Dynamics simulations of ref. [30] have demonstrated that a covalent bond component in l-Si prevails in the under-cooled liquid state and causes a strong reduction of the l-Si self-diffusion. Consistently we can deduce that impurity atoms in the lower diffusivity state dominate

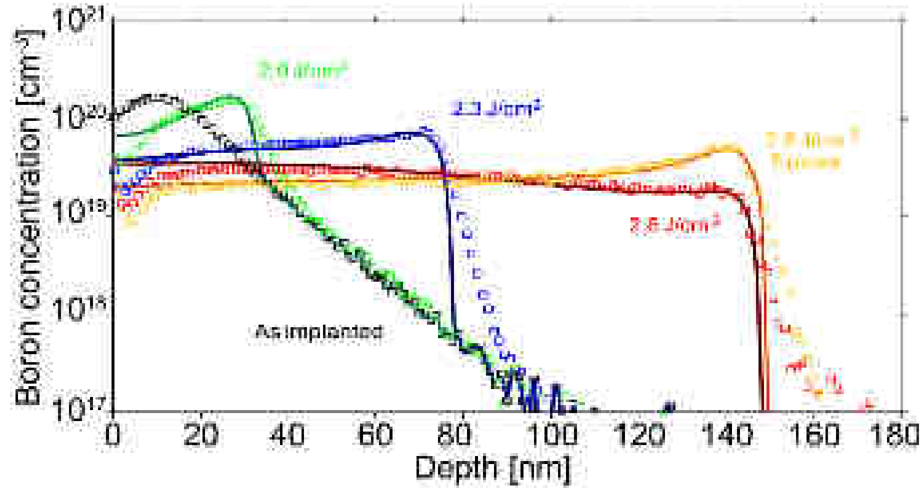

Figure 2.6: *SIMS (squares) and simulated (by means of the two-state model, eqs. 2.47-2.49, solid lines) B profiles obtained after single pulse laser irradiations at 2.0 (green), 2.3 (blue), and 2.6 (red) J/cm^2 energy densities. Multi-pulse case (5 pulses) is shown as orange curve. The value of k^τ=1.0 $\times$ 10^7[s^{-1}] is used. Data from G. Fisicaro et al. ref. [14].*

the migration in under-cooled regions and $\bar{R}(T) > 1$, whilst $\bar{R}(T) < 1$ for T well above the melting point and atoms in the higher diffusivity state characterize the impurity kinetics. In the solid phase metallic bonds are not present and $D_{sol} = D_{sol}^{HD} = D_{sol}^{LD}$ [31]. k^τ is a rate coefficient controlling the transition between the two states which should be also related to the rapidity of the bonding order fluctuations in l-Si and l-Ge. Its value has been generally fixed as a constant [14, 15], although a T dependence can be derived when additional data will be available for more refined estimates of the model parameters.

Dopant atoms in the lower diffusivity state are strongly favored in regions with $T < T_m$ whilst atoms in the higher diffusivity state characterize the impurity kinetics in the stable liquid regions.

Temperature-dependent diffusivity in the liquid phase is an obvious consequence of the two-state model. However, the anomalous redistribution is an additional effect being the impurity pile-up mechanism inherently related to the local un-balance between states with high and low mobility.

Comparisons between the model's prediction of diffusion profiles and Boron (B) density profiles measured by SIMS in implanted Si (B 3 keV energy, 5$\times$10^{14} cm^{-2} dose, black circles in the figures) after single pulse LA processes at different energy densities are shown in fig. 2.6. The post-LA B profiles predicted by the diffusion model (solid lines in fig. 2.6) are in satisfying agreement with the experimental ones.

2.5 LIAB: The Laser Innovation Application Booster

As discussed earlier, the application of the LA process in future electronic device generation is hindered by the difficulties in the process control. In particular, LA processes are highly influenced by the interaction between the electromagnetic field and complex device structures. Numerical models of laser annealing processes, based on the formalism presented previously have been developed by the team at the Consiglio Nazionale delle Ricerche (CNR) for particular limited applications and implemented in academic or commercial packages [12–14, 32]. However, several limitations remain (see e.g. discussion in ref. [33]) in the previous modeling approach for the general application in future devices, characterized by complex structures with nm wide elements made of different materials/phases.

In the framework of a collaboration between the CNR and the laser equipment provider SCREEN Semiconductor Solutions Co.-LASSE, we have developed a tool (named LIAB: Laser Innovation Application Booster) based on the FEniCS open-source package (see `https://fenicsproject.org/`) for the simulation of LA process in complex device structures. The FEniCS's project aims at providing a comprehensive set of subroutines for the solutions of stationary linear and non-linear partial differential equations using the finite elements method. Time integration (needed for LA simulations) and coding for the use in parallel machines for HPC need original implementation as well as all the support coding for the proper engineering of the formalism in order to create a unique tool in the Technology Computer Aided Design (TCAD) format i.e.: graphical interface, database setting, pre-processing to correlate the database to the structure, output, analysis of the output).

The main features of the LIAB package are:

- A versatile Graphical User Interface for the structure design, the material assignment and the simulation analysis;
- An interface with the FEniCS solver for the automatic generation of the mesh and the runtime control;
- The calibration of a number of materials (optical and thermal properties and mass transport) as a function of temperature and phases;
- The efficient coupling with Electromagnetic Simulation for the self-consistent source estimation (i.e. power dissipation) in nano-structured topographies;
- The experimental validation in nanostructured samples;
- Multiple-dopant models simulating dopant atoms redistribution, including diffusion, solubility and segregation;

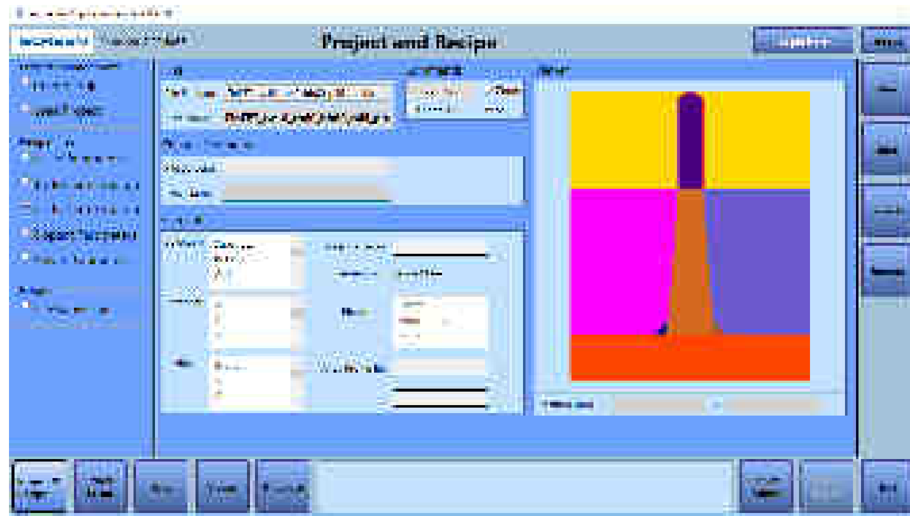

Figure 2.7: *Screenshot of the LIAB Graphical User Interface, a FinFET device is shown and the different colors indicate the domains, which can be initialized with different material properties.*

- An alloy model, e.g. SiGe (where the melting point depends on the alloy fraction);
- Multiple phases (e.g. amorphous, liquid, crystal).

An example of the GUI and the corresponding output of the simulation is reported in figs. 2.7 and 2.8, whilst the details of the tool functionality are discussed in the Appendix B.

Due to the strong non-linearity of the numerical problem, code validation cannot use analytical results apart from some trivial 1D *toy* specification of the problem. In the remaining part of the chapter, we report a survey of the validation activity in planar structures, which uses a commercial tool (COMSOL Multiphysics®) and experimental data for the comparisons.

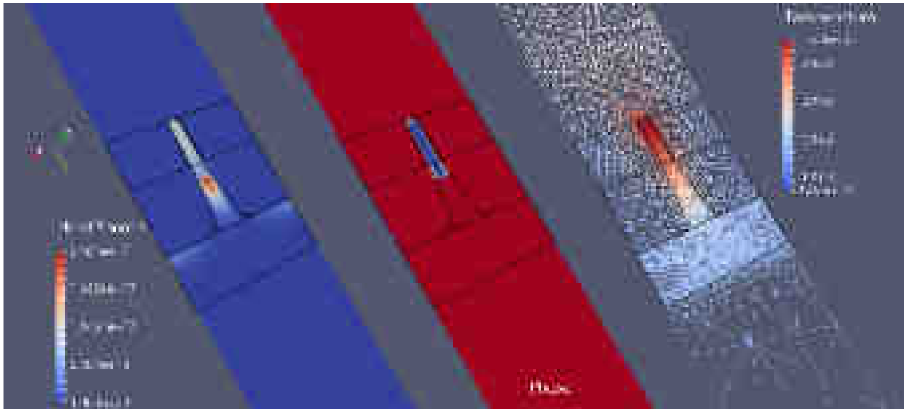

Figure 2.8: *Simulation example of the Laser Annealing process in a FinFET device structure, from left to right the heat sources, the phase (liquid phase in blue, solid one in red) and temperature. The used mesh is also shown. The correlation between phase and heat source in the figure demonstrates the role of self-consistency in the simulation. The sample at the extreme right shows also the mesh used in the simulations.*

2.6 Validation study I: 1D case silicon

The structure considered for the validation study is composed of a stack of three layers as shown in fig. 2.9. The top layer is 200 nm thick and it is composed by air, the thickness of the middle zone is 100 nm, the bottom layer is 10μm thick and it is composed of crystalline Si (c-Si) in all the tests here reported. We have performed a large number of tests considering all the materials in the calibration database presented in Appendix A. However, materials that can melt are the most interesting to consider and we limit the discussion to these cases. In this section the c-Si case is considered.

We note that the use of a thick substrate (i.e. thickness of about 10μm and above) is necessary to properly describe the thermal field decay. However, it should be considered that this choice could increase the demand for computational resources (especially for 2D systems) due to the corresponding increase of the mesh point and related degrees of freedom (DOF) of the numerical problem. Hence, a compromise has to be be found. On the other hand, even the air layer above the structure contributes to the increase of the DOFs. Anyhow, its presence and a good mesh resolution in this region are necessary to study the electromagnetic problem with the required accuracy. A size comparable to the wavelength of the laser source can be considered a reasonable indicator for the choice of the size of this layer.

The initial state of the simulation reproduces a planar Si wafer at room temperature. As a consequence, we set for the whole system a uniform temperature field $T_0 = 300$ K. The same temperature T_0 is imposed (Dirichelet boundary condition), for all the duration of the simulation to the lower

boundary, marked with a big point in the figure. A zero flux (Neumann) boundary condition is imposed on the top (Air) boundary. The phase field model used for the comparison is the one proposed by Wheeler (subsection 2.3.3) The initialization value of the phase field is $\phi = 1$ everywhere, and this value is imposed also as a boundary condition on the bottom boundary. Phase changes are inhibited in the substrate (the melt front does not reach this zone for all the simulated cases) in order to relax the mesh size in this region. The incident wave is coming from the top of the air with a descending direction.

In order to optimize the simulation performance we chose to use a nonuniform computing mesh. The mesh points in the portion of interest (i.e. the central one) are very close to each other (small cell size of the order of 0.5nm), while their distance increases far from this region (see fig. 2.10). In spite to this optimized computational box used the DOFs, for this system there are more than 15000 mesh points.

In fig. 2.11 we report the maximum temperature in the system as a function of the time for an irradiation process with an energy density of 0.5 J/cm^2, obtained using COMSOL® (blue line and triangles) and LIAB (red line and square). In this case we are considering a non-melting process. The plot shows also the laser pulse considered as a magenta line and circles. The interaction of the laser with the thermal response of the system can be divided in multiple zones:

1. from 0 to 36 ns the source is zero, so the temperature remains unchanged and equal to T_0, as imposed at the beginning of the simulation

2. from 36 to 120 ns there is the ignition of laser and consequently the heating up of the sample. The slope depends on the material and the fluence.

3. from 130 to 210 ns, despite the laser power goes down, the temperature continues to rise

4. from 210 to 320 ns the system begins the thermal quenching, since the laser is now too weak to sustain the high temperature against heat diffusion

5. from 320 to 500 ns the laser reaches again the zero value. Consequently the temperature continues to decrease (the external heat source is zero). The overall thermal inertia of the system changes the slope of this state.

6. at larger times (not shown in the figure) the system continues to reduce the temperature, and reaches again the 300 K after a couple of microseconds.

Figure 2.9: *Schematic of the simulated 1D structure. From the top to the bottom there are: 200 nm of air, 100 nm of the chosen material and 10 μm of silicon.*

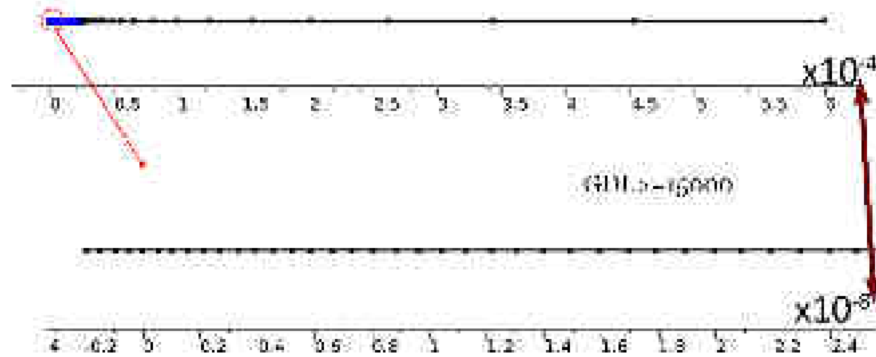

Figure 2.10: *The figure shows the mesh used in the simulation. The figure below is a zoom of the upper one, showing the graphic scale on the right.*

For all other cases here discussed the trend of the thermal field is similar apart from the particular interval of time of the different zones. In the cases with phase change, the energy absorbed (released) during this transition creates an additional feature: i.e. a plateau of the thermal field close to the melting temperature (see e.g, fig. 2.13 from 80 to 300 ns). The difference between the simulated curves of maximum temperature is very small in spite of the fact that the two simulations run on different software (different mesh and different Finite Element Method implementation). The differences are minimal also when the Enthalpy model is applied or when the heat absorption is approximated by an analytic exponential expression as usually considered in 1D simple systems (see e.g. [12]).

By increasing the fluence of the laser, the slope of the heating phase is greater and a higher value of the maximum temperature is obtained (see fig. 2.12 where the time dependence of the maximum temperature is shown for a fluence of 1 J/cm^2. The shape is similar to the previous case, and also here there is no melting. Again the agreement between the LIAB result and the reference is very good.

By increasing further the laser fluence, the system can reach the melting temperature and, as a consequence, there is a phase change and the liquid begins to appear. As discussed, we can mark the fusion with a plateau in the maximum temperature as function of time. If the fluence is high enough, the temperature can also continue to grow. Figure 2.13 shows a silicon system under a laser fluence of 2 J/cm^2, where from 120 to 320-350 ns there is the coexistence of liquid and solid phase in the system. In this case we show a comparison using the maximal difference of the internal setting of COMSOL® and LIAB. Indeed, this COMSOL® simulation is performed with the phase field and approximate analytic expressions for the heat source, whilst the LIAB one uses the Enthalpy model, setting the full self-consistent electromagnetic simulation for the source calculation. The

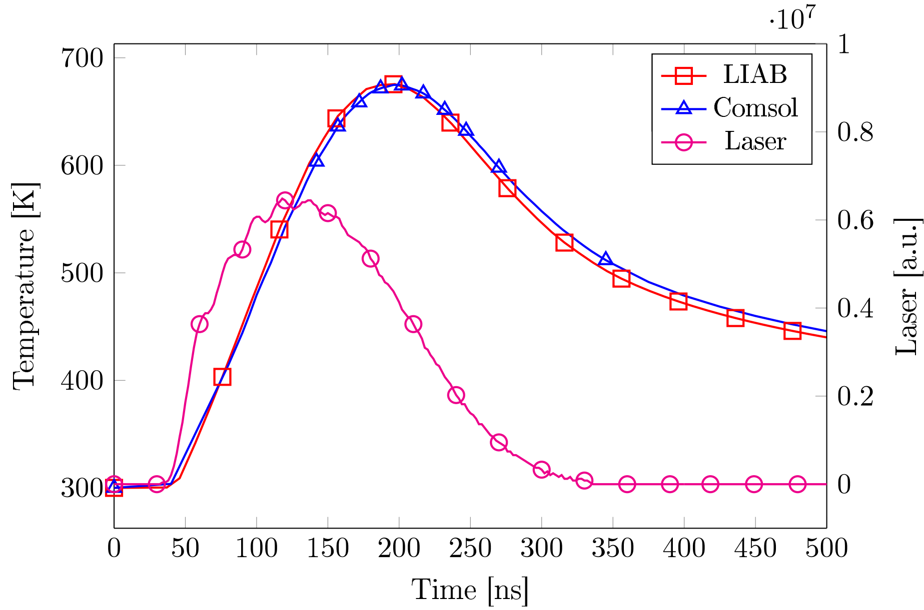

Figure 2.11: *Comparison between LIAB (red line and squares) and COMSOL® (blue line and triangles) simulated maximum temperature for a 1D structure made of silicon for a LA process with a fluence of 0.5 J/cm² (non melting case). The magenta line with circles is the normalized laser pulse.*

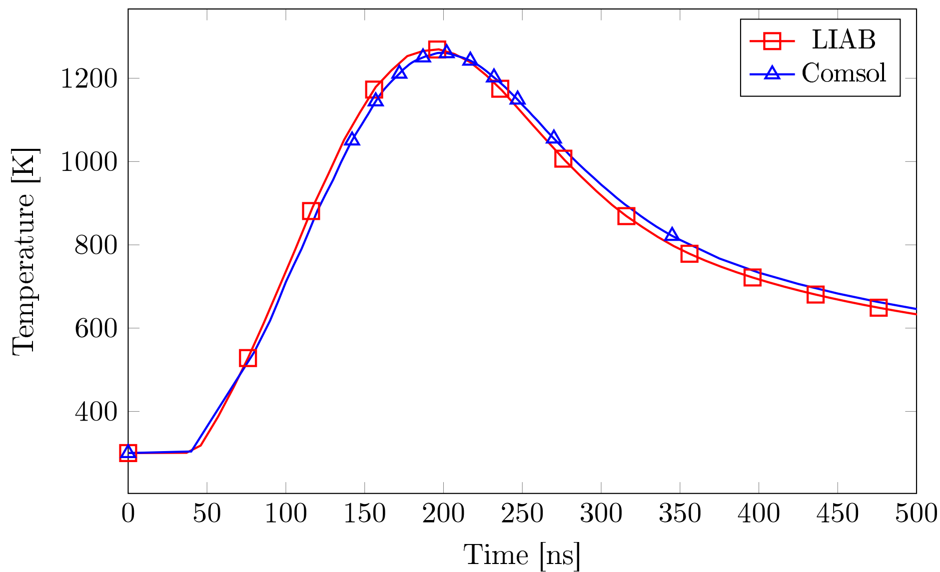

Figure 2.12: *Comparison between LIAB (red line and squares) and COMSOL® (blue line and triangles) simulated maximum temperature for a 1D structure made of silicon for a LA process with a fluence of 1.0 J/cm² (non melting case).*

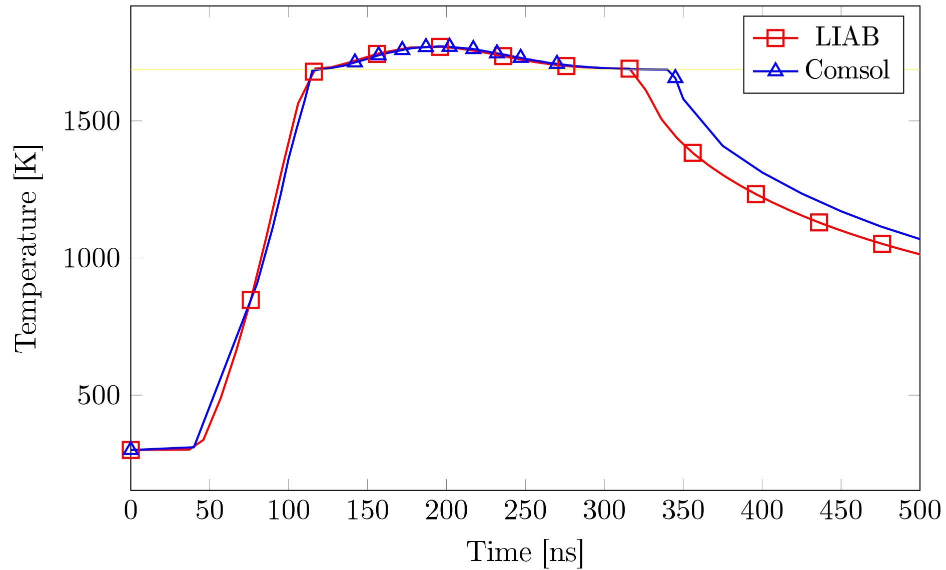

Figure 2.13: *Comparison between LIAB (red line and squares) and COMSOL® (blue line and triangles) simulated maximum temperature for a 1D structure made of silicon for a LA process with a fluence of 2.0 J/cm^2 (melting case).*

different setting for the laser-material interaction is more relevant and affects the melting evolution, since a dynamical source change is expected in the early stage of the melt front movement when the liquid film thickness is lower, or similar, to the absorption length of the light. In this case, whilst the overall agreement between simulation is very good on the left and central part of the graph, at the end of the simulation there are some more relevant differences. The simulation with LIAB has a shorter melting phase and a lower final temperature. This difference can be explained when thinking at the problem and its intrinsic complexity, including the self-consistent simulation of the heat source. The difference in the integration rules leads to some differences also when the same software is applied, since the material characteristics change in space and time. Anyhow, for a practical application, the prediction obtained with the two methods is equivalent since the maximum melt depth is similar in the two cases and global discrepancies are compatible with the different numerical schemes considered in the simulation setting. In order to confirm the above assumption, we show simulation reliability results in fig. 2.14, where we compare the melt depth in the sample (red squares) and our simulation (green line), for different laser energies, obtaining a good agreement.

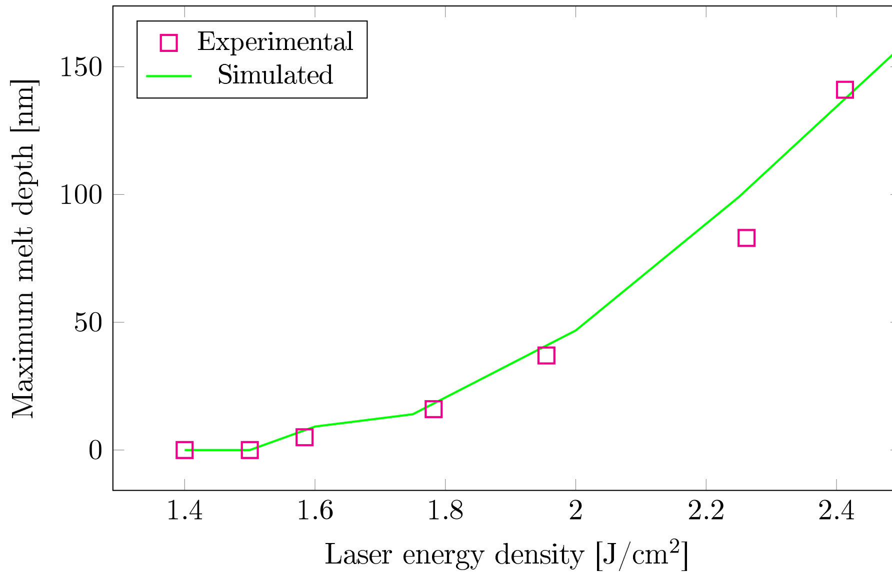

Figure 2.14: *A comparison between LIAB simulated (green line) and experimental (magenta squares) maximum melt depth. The central part of the 1D structure is made of silicon.*

2.7 Validation study II: 1D case non silicon materials

Similarly to the analysis of the previous section we have investigated the LIAB code reliability, by changing the material in the middle part of our test structure, obtaining in all cases encouraging results. As an example, we report comparison between the maximum temperature calculated by the two codes for germanium (fig. 2.15) and copper (fig. 2.16) in sub- melting conditions. All the material parameters used are reported in Appendix A.

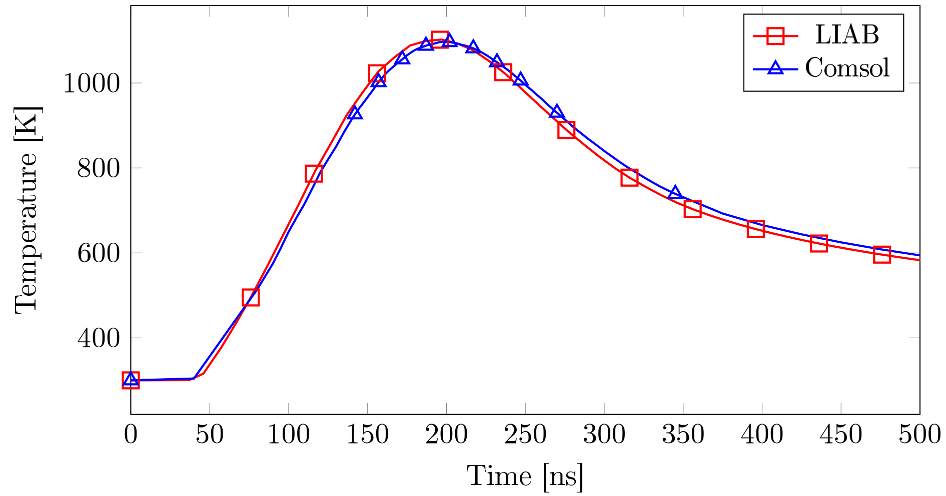

Figure 2.15: *Comparison between LIAB (red line and squares) and COMSOL® (blue line and triangles) simulated maximum temperature for a 1D structure made of germanium/silicon stack for a LA process with a fluence of 0.5 J/cm^2 (non melting case).*

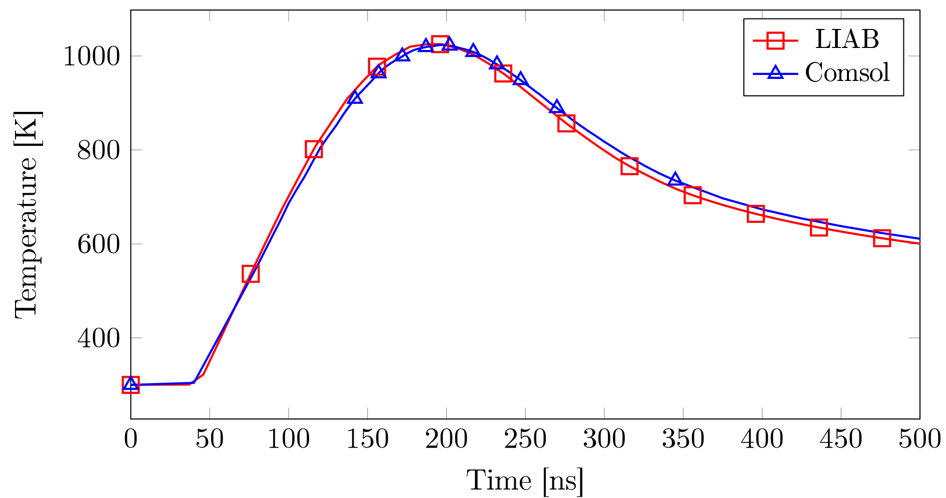

Figure 2.16: *Comparison between LIAB (red line and squares) and COMSOL® (blue line and triangles) simulated maximum temperature for a 1D structure made of a copper/silicon stack for a LA process with a fluence of 1.0 J/cm^2 (non melting case).*

2.8 Validation study II: 1D case versus 2D planar case

A probing check of the reliability of a time FEM integration is the comparison between results in "equivalent" 1D an 2D planar structures, where, passing from the 1D to the 2D discrete mesh brings crucial internal modifications in the numerical approach. As a consequence, we have replicated the 1D structure in a corresponding 2D one and we have compared the results in the two cases. We created a planar structure, with the same vertical dimensions of that shown in fig. 2.9 on page 45 and a width of 50 nm (see fig. 2.17). Of course, with this new configuration is mandatory to take into account some differences in the solver setting. The first one is the boundary conditions. In particular, we can replicate the upper and lower conditions but now we must introduce the continuity constrain for the right and left limits of the 2D system in order to simulate an infinite box which makes equivalent the 1D and 2D cases. Another strong difference is now the choice of mesh which impacts also on the comparisons. Indeed, while in 1D systems the meshes have very similar behavior for LIAB and COMSOL® (and are more easily controllable), in the 2D case we get a topologically different mesh in the two cases, even imposing the same minimum dimension, or other typical control parameters. The size and placement of mesh points are important in this problem, due to self-consistency and they can affect the result (just think about the absorption length of the light and the mesh size that can resolve it). On the other hand, in the 2D case we can not use a very refined mesh, as in the 1D case, because of the exaggerated number of resulting DOF.

Similarly to the methodology applied to the previous section, also in this case the central part includes different materials, whilst a *c*-Si substrate is included for all the cases.

All the graphs from 2.18 to 2.22 show the maximum temperature over time for different materials and laser fluences as they result from four kinds of simulation: $LIAB_{1D}$, $LIAB_{2D}$, $COMSOL_{1D}$ and $COMSOL_{2D}$. The color curve convection is: same color of the previous cases discussed for the 1D case and a lighter color for the corresponding 2D cases with different markers.

Starting with fig. 2.18 we can see the usual thermal shape for a non melting case, with a good agreement between the different four cases. Going deep with the analysis we can see that the curves 1D and 2D of each software are very close to each other, proving that in spite of mesh modification the inner software solution is consistent.

By increasing the laser fluence the sample reaches higher temperatures and, regarding a germanium sample under irradiation at 1.2 J/cm^2, fig. 2.19, we observe a melting process. The solution differences are very limited, and like the 1D case (see fig. 2.13 on page 48)) the LIAB solution has a shorter

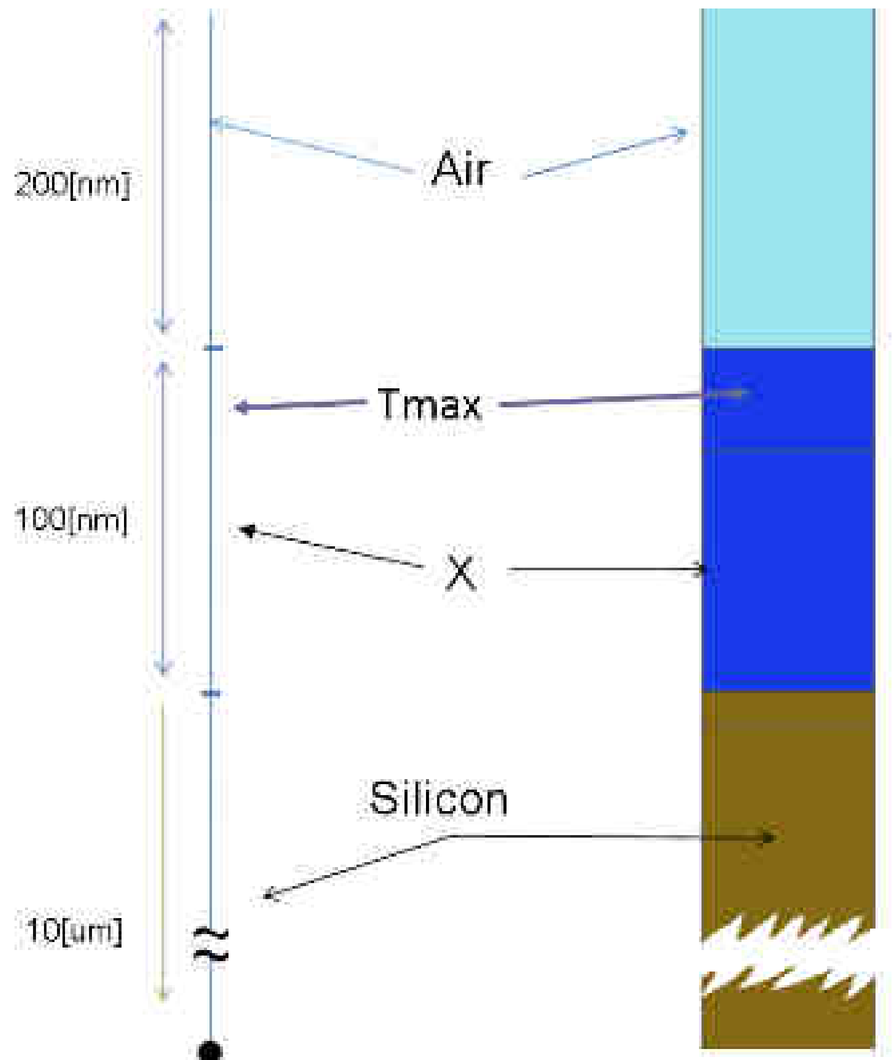

Figure 2.17: *Schematic of the 2D structure (in the right side plot) in comparison with the 1D one (in the left side plot). Again the substrate is always Silicon and the upper part is air. The middle parts are made by different materials. The width is 50 nm.*

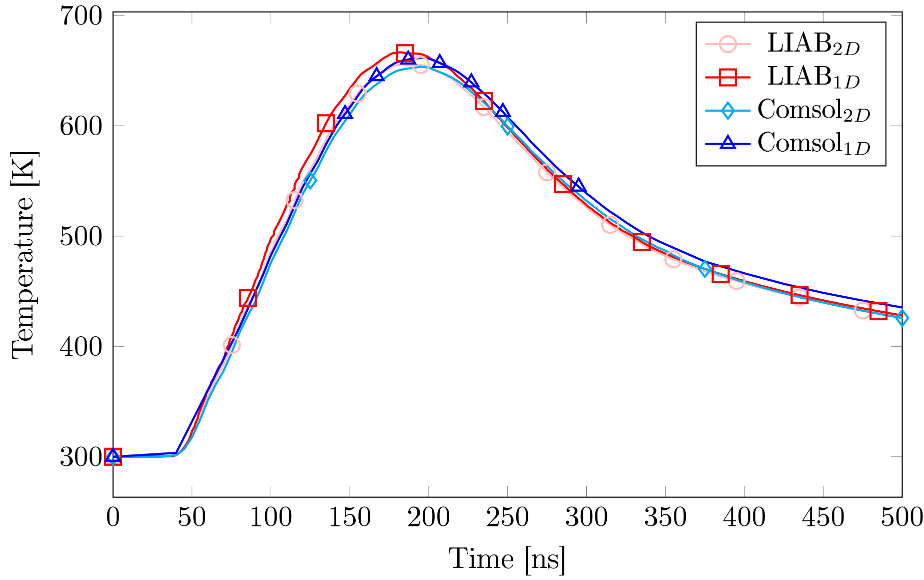

Figure 2.18: *Comparison between LIAB and COMSOL® predictions of the maximum temperature as a function of time, for the 1D and 2D cases in a structure made of germanium/silicon stack, for an irradiation process with a fluence of 0.4 J/cm^2 (non melting case).*

melting time. The internal consistency of each solver, i.e. the agreement between 1D and 2D, is optimal. Note that the horizontal orange line in the figure represents the melting temperature of the germanium.

Using copper in the central part, under a laser irradiation with a fluence of 2 J/cm^2, we obtain fig. 2.20. The violet line represents the melting temperature of copper. The melting zone is very wide with respect to the other cases. We point out that in this graph the COMSOL$_{Dd}$ curve shows convergence problems, while our LIAB code does not produce such an error. Another difference is that on the left part (the heating) COMSOL$_{2D}$ and LIAB$_{2D}$ are very close, while LIAB$_{1D}$ is different. On the right part (the end of solidification and the cooling down) LIAB$_{1D}$ and LIAB$_{2D}$ are closer. This discrepancies can be explained by the role of the mesh due to the peculiar optical properties of Cu (extremely low absorption length and reflectivity close to 1 in the liquid phase, see material properties in the Appendix A on page 139).

In the tests we have also considered the silicon/germanium alloy with the particular composition $Si_{0.5}Ge_{0.5}$. Due to the particular geometry and processes, in this chapter this alloy is considered a constant material i.e. no changes in the alloy fraction are taken in account. In fig. 2.21 we report the results for a fluence of 0.6 J/cm^2 (non-melting case) whilst fig. 2.22 shows the same system under irradiation for a fluence of 1.2 J/cm^2 (from 120 to

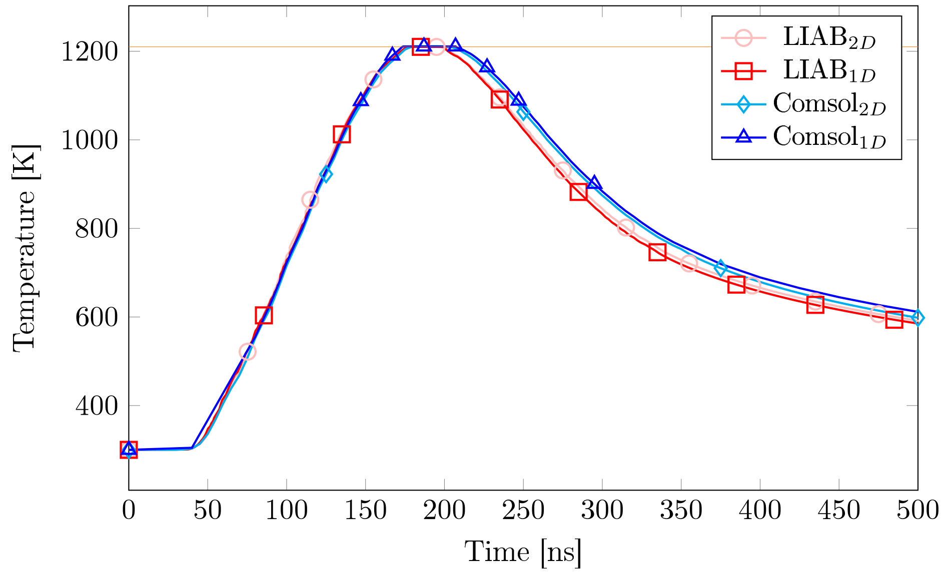

Figure 2.19: *Comparison between LIAB and COMSOL® predictions of the maximum temperature as a function of time, for the 1D and 2D cases in a structure made of germanium/silicon stack, for an irradiation process with a fluence of 0.8 J/cm^2 (non melting case). The horizontal represent the melting temperature of germanium.*

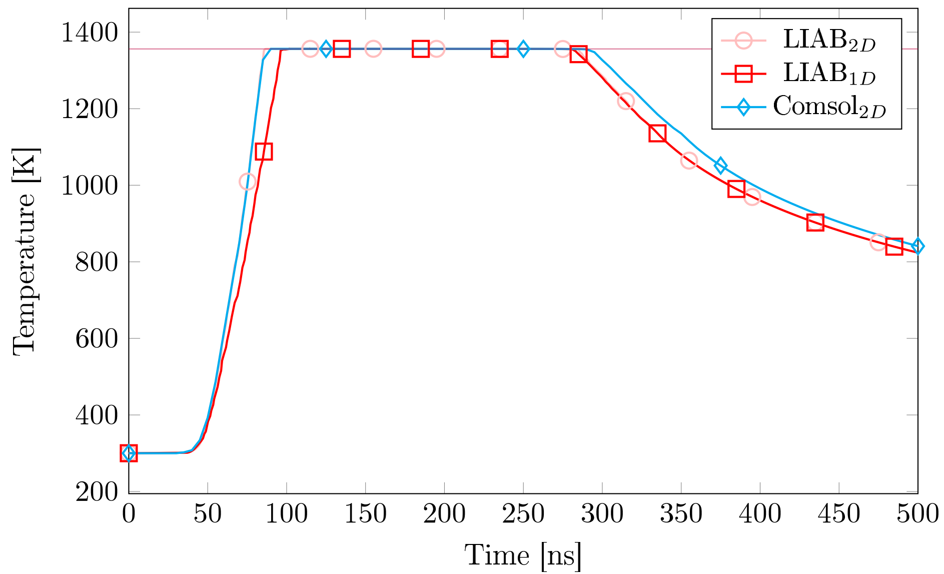

Figure 2.20: *Comparison between LIAB and COMSOL® predictions of the maximum temperature as a function of time, for the 1D and 2D cases in a structure made of copper/silicon stack, for an irradiation process with a fluence of 2.0J/cm^2 (melting case). The COMSOL1_{1D} curve is not present, see the text. The horizontal represent the melting temperature of copper.*

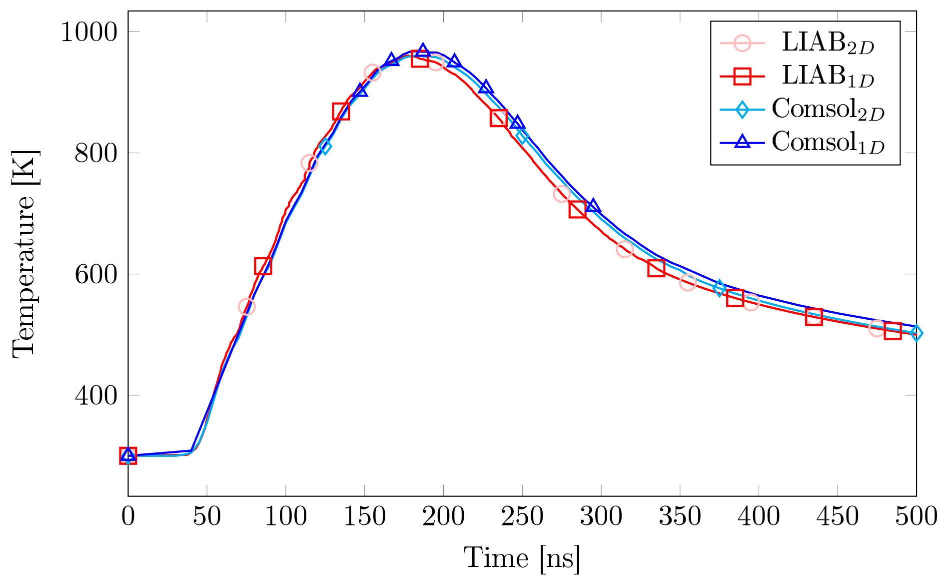

Figure 2.21: *Comparison between LIAB and COMSOL® predictions of the maximum temperature as a function of time, for the 1D and 2D cases in a structure made of SiGe/silicon stack, for an irradiation process with a fluence of 0.6 J/cm^2 (non melting case).*

250 ns we can observe the melting signature). A similar trend and agreement for the other semiconductor materials can be observed also in this case.

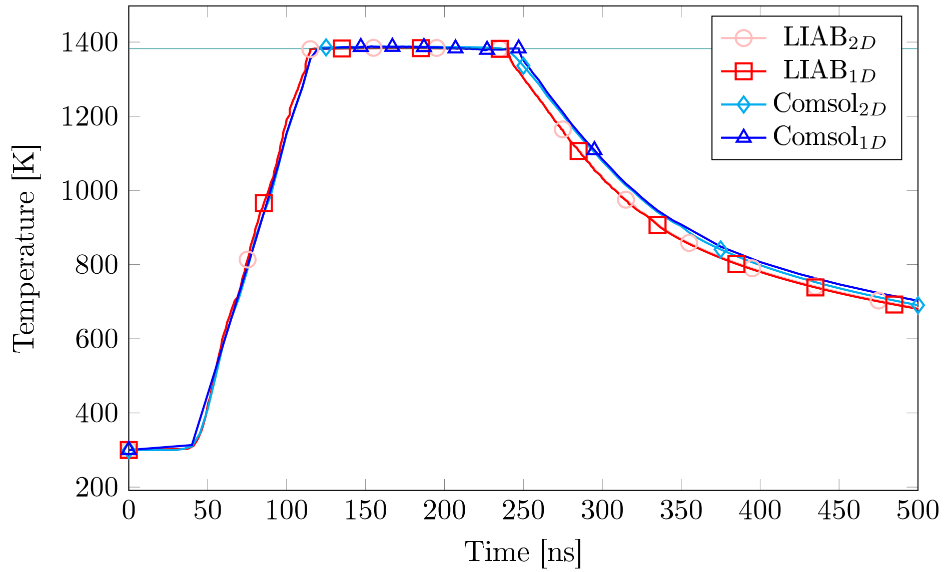

Figure 2.22: *Comparison between LIAB and COMSOL® predictions of the maximum temperature as a function of time, for the 1D and 2D cases in a structure made of SiGe/silicon stack, for an irradiation process with a fluence of 1.2J/cm^2 (melting case).*

2.9 Conclusion

In this chapter we have presented the complete theoretical framework considered for the simulation of laser annealing processes and its implementation in numerical codes. We have moreover shown a part of the validation activity performed to test the numerical results obtained with the new LIAB tool, which we have co-developed within the framework of a collaborative project. Overall the benchmarks of the new software have shown satisfactory results, while the fully self-consisted electromagnetic calculations here implemented make its accuracy even superior to results obtained with commercial software. These innovative features make LIAB a reliable instrument for the TCAD study of laser processes in ultra-scaled device structures, which is the main argument of the following chapters.

3

Laser Annealing of FinFET structures

3.1 Introduction

Vertical integration is an innovative nano-electronic device design strategy which requires the manufacturing of stacked transistor structures. The annealing processing of the superior structures should minimally affect the materials composing the inferior ones. Laser annealing provides localized heating sources that should in principle allow for the processing of the upper structures in a staking sequence of nano-transistors without promoting degradation of the lower ones. Anyhow, due to the peculiarity of the LA process already discussed in the previous section, the process design is critical and the process window difficult to determine. In this chapter we apply the developed numerical tool to the LA process design for a Fin Field Effect Transistor (FinFET). The aim of the analysis is the discussion of the predicted LA results as a function of the geometry and process parameters, especially for the use of the process in the advantageous melting regime.

The basic FinFET layout in ideal original configuration looks like the one sketched in fig. 3.1. In a fabricated device, the active gate area is the intersection of the Green-color gate and the semiconductor material forming the Fin structure of fig. 3.2, where arrows show the direction of the current flow. As a 3D structure, the layout area of a FinFET is smaller than a planar device, and the source-drain region is fully-depleted, resulting in:

- A reduced leakage compared to planar CMOS
- Less variability
- Lower operating voltages

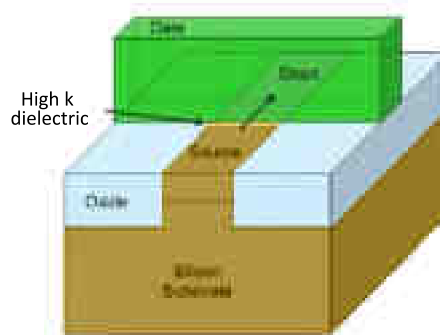

Figure 3.1: *FinFET in the original planar configuration. Not drawn in scale.*

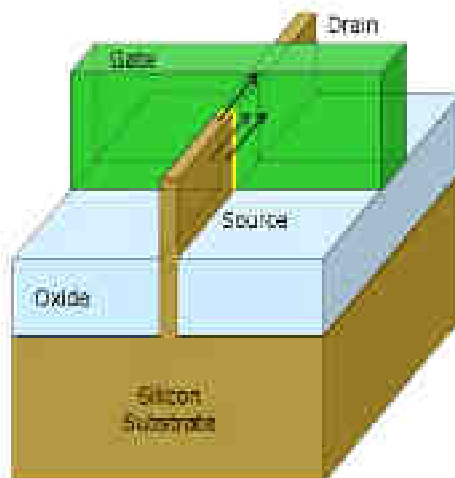

Figure 3.2: *Isolated FinFET geometry. Not drawn in scale.*

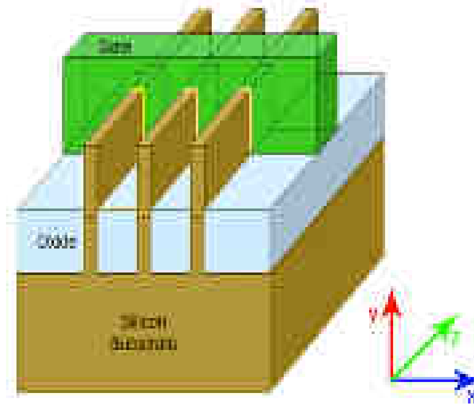

Figure 3.3: *Integrated periodic FinFET structure considered in the simulations.*

Multiple fins (see fig. 3.3) are required for the integration in a chip and they could have in principle different effective widths and pitch. However the design rule indicates that the device sizing is quantized instead of totally variable. As a consequence, on the down-side, the FinFET technology has some new circuit design trade-offs [34]:

- Quantized widths
- No body biasing to control leakage or speed
- Higher parasitic values
- Aging and self-heating effects

Some of these issues could be minimized with a proper processing, which in turn should be performed in precise geometric conditions.

3.2 Simulation settings

Looking at the fig. 3.3, we note that the FinFET structure shows a periodicity on the x axis and a symmetry along the z axis. As a consequence, it is possible to study a simplified 2D structure instead of the complete 3D one, using appropriate boundary conditions. In fig. 3.4 we show a TEM image of the FinFET devices, performed before the irradiation process, which we use as a reference for the specific TCAD geometry shown in fig. 3.5. The substrate is made of silicon with a total depth of 10 μm (not totally shown in the figure). The Fin structure is also made of silicon and is surrounded by silicon dioxide (in green). The upper part of silicon (the top-Fin) is surrounded by a cap layer of silicon dioxide of ~ 2 nm. This layer reproduces the presence of the native oxide which is simulated assuming the same properties of the

other SiO_2 layers. Please note that the LIAB tool allows for assigning easily material properties to each layer (i.e. simulation sub-domains indicated by thin black lines in the figure) uploading them from the list present in the **Database** or using user defined expressions or functions of the fields (e.g. temperature, phase), see Appendix B. As a consequence different oxide properties (due to e.g. impurity presence and the deposition method) can be considered if necessary. The system is completed with a top layer of 200 nm of air. For what concerns the temperature we impose a uniform temperature in the whole system at the beginning of the simulations with the value of $T_0 = 300$ K. We also set a constant temperature in the lower boundary of the system, fixed at 300 K and a condition of symmetry on the left and right boundaries. This condition is consistent for the periodic simulation of the surrounding FinFETs, that are considered equal. The incident wave is coming from the top of the air and is directed along the y axis in a descending direction. We start the simulation with a value of $\phi = 1$ in all the domains, which implies that the whole structure is in the solid phase. With this convention we consider the same solid condition for silicon (crystalline), for SiO_2 (amorphous), and for the air (gas). This issue is not a real problem. In fact, we assign the characteristics of the specific phase to the $\phi = 1$ value when simulating a material which does not undergo to a first order melting transition (i.e. with the release/absorption of the latent heat). The great advance of using this approach is that starting with a constant value everywhere significantly improves the simulation stability. In this case, when there is melting, there is only a change in the phase field equation (0-1) in the silicon domain, the only one that is supposed to melt, without other phase changes. We are interested in studying:

1. the influence of the pitch (that means the distance between the Fins) with fixed design values of 35-45-90-135-180-225-270 nm
2. the effect of various laser energy densities
3. the effect of different laser polarizations

In the simulation tool and also in the design rule there are no constrains on the polarization values to use. Anyhow, we concentrate our interest on the most used cases: TE, TM and some mixed value of the TE and TM components. The polarization cases considered are mainly 0, 45 and 90°. The material parameters used for the simulation are reported in Appendix A from page 139.

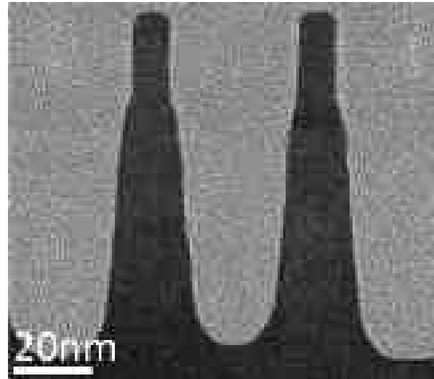

Figure 3.4: *A TEM image of the FinFET for the 45 nm pitch geometry in cross sectional mode. The silicon body (the darker one) is surrounded by silicon dioxide (in light grey).*

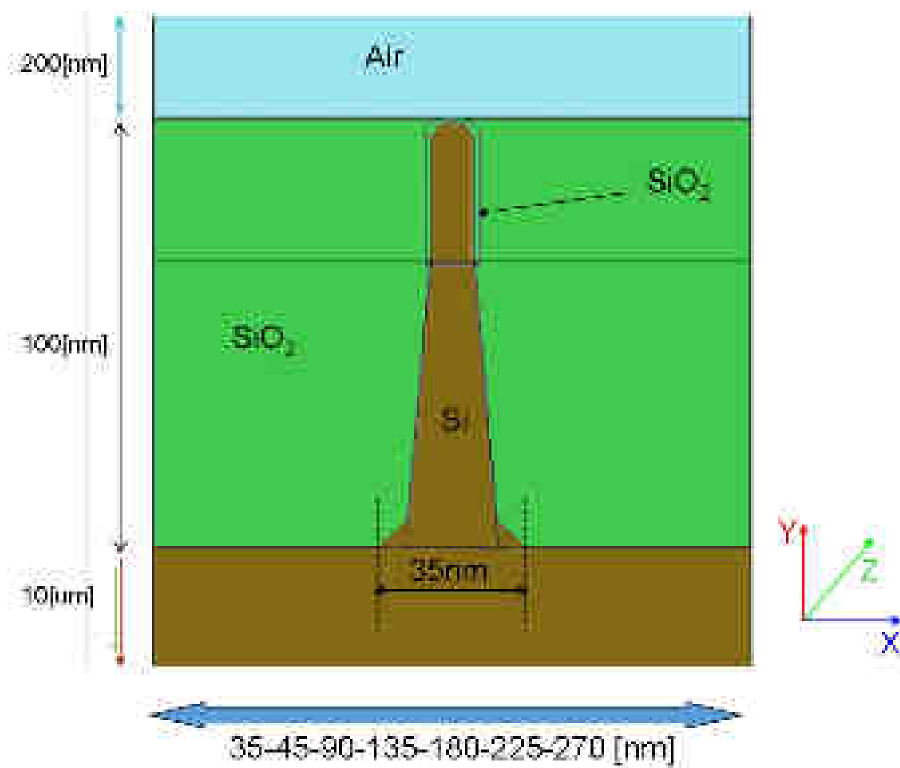

Figure 3.5: *Simulated FinFET structure which reproduces the one shown in the TEM image of fig. 3.4.*

3.3 Focused Results

We have decided to show an extended analysis for only three of the FinFET geometries (35, 45 and 135 nm). Results relative to the other geometries are discussed by means of summarizing plots showing trends of average quantities.

From fig. 3.6 to 3.12 we show the maximum temperature reached in the FinFET during the LA process for different values of pitch and fluence for the three values of polarization. For all the graphs, the conventions for indicating curves relative to the different polarization are the same. In these figures the melting area is also indicated with a lighter color than the corresponding temperature curve. The horizontal lines represent the total area of the top-Fin, in brown, and the total Fin, in black.

Figure 3.6 shows the maximum temperature in the FinFET for the 35nm geometry under an irradiation process at 0.6 J/cm^2 fluence for different polarization degrees of the laser light. The temperature function follows the trend discussed in the previous chapter (in this case there is no melting), but we can observe quantitative differences by varying the polarization. For this particular condition, the maximum difference in temperature simulated for the 0 and 90° case is ∼200 K. We underline that in all the simulations we consider the same laser energy. As a consequence, the differences in temperature arise from polarization dependent distributions of the heat source (see fig. 3.15).

When increasing the fluence, we observe an increment of the maximum temperature reached in the system, see for example figs. 3.7 and 3.8. If the temperature is high enough, the silicon melting point can be locally achieved. The SiO_2 has a higher melting temperature and is expected to remain solid or eventually to undergo to a glass transition (no latent heat release). In the 0.7 J/cm^2 fluence case, only for the 90° polarization melting is predicted. In the other polarization cases the maximum temperature is always below the melting temperature. In the 0.8 J/cm^2 case the fluence is high enough to simulate melting in all cases. We underline that the melting profile (area, depth, duration) is not the same for the three cases due to the different heat source distributions, that depends from the polarization angle.

In fig. 3.9 we show, from the left to the right panel, the temperature, heat source and phase field for 0.7 J/cm^2 at 186 ns for 90°. The temperature field shows a rather uniform distribution close to the melting temperature. The heat source field is 0 in the materials that are transparent to the radiation (in this case air and silicon dioxide) or too distant from the interaction interface with respect to the absorption length of the material (i.e. silicon in the bulk regions). While the heat source is relevant only in the FinFET region, the portion of the system shown in the figure reaches a quite constant value of temperature due to the large thermal diffusivity. The phase shown in violet is the liquid zone, while green is the solid phase. A dashed-dot line helps to

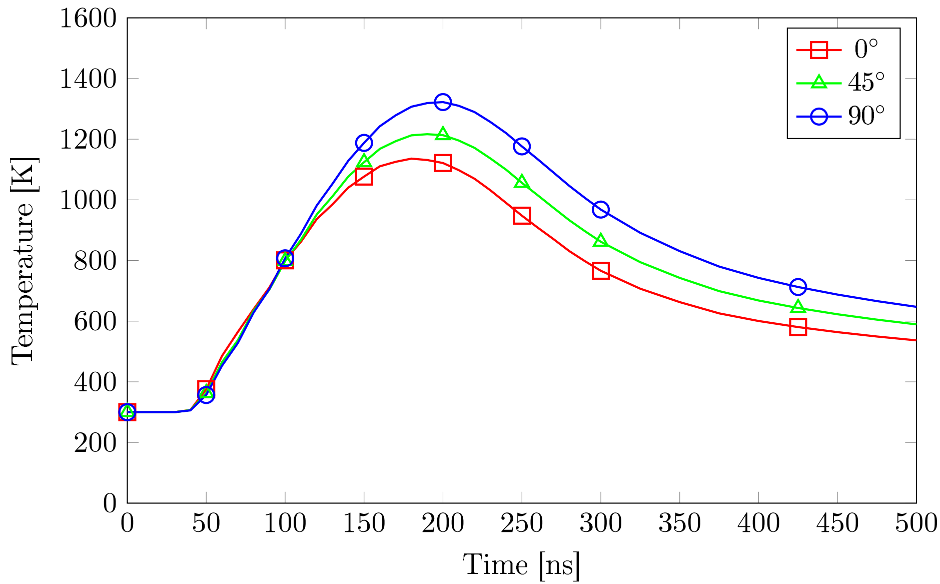

Figure 3.6: *Maximum temperature in the top-Fin region for a FinFET with pitch of 35 nm and an irradiation process with 0.6 J/cm^2 energy density for the values of 0°, 45° and 90° of the laser light polarization.*

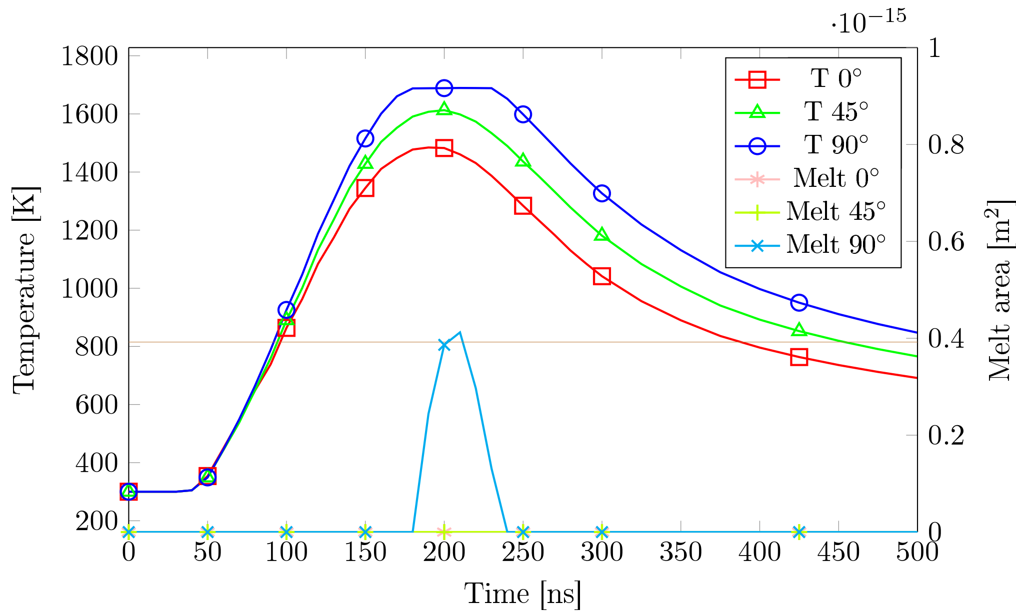

Figure 3.7: *Maximum temperature in the top-Fin region and total molten area as functions of the time for a FinFET with a pitch of 35 nm and an irradiation process with 0.7 J/cm^2 energy density for the values of 0°, 45° and 90° of the laser light polarization. Total top-Fin area is indicated by the horizontal line.*

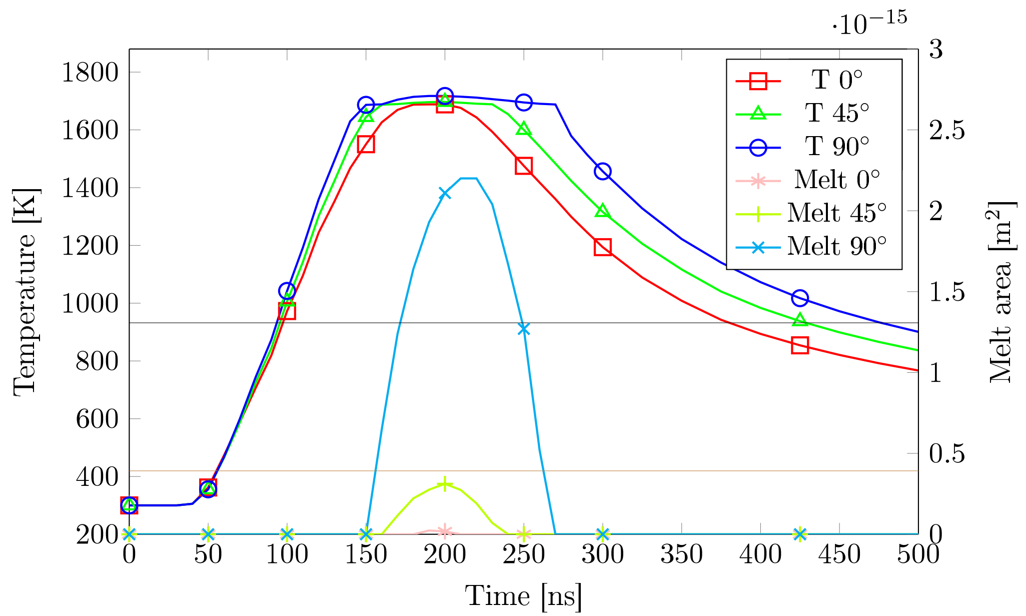

Figure 3.8: *Maximum temperature in the top-Fin region and total molten area as functions of the time for a FinFET with pitch of 35 nm and an irradiation process with 0.8 J/cm^2 energy density for the values of 0°, 45° and 90° of the laser light polarization. Total top-Fin and bottom-Fin areas are indicated by the horizontal lines*

link the change in the phase field (from liquid to solid) to the drop of the local value of the heat source. This frame shows again that the thermal, phase and EM fields are strongly coupled and by interaction they are modified self-consistently.

The figures from 3.10 to 3.12 show a similar graphical analysis as the previous ones for the 45 nm geometry. We note that, although the difference is very small in terms of geometry (in this case the pitch is only 10 nm larger), the differences in terms of thermal results are large. Comparing for example fig. 3.7 with fig. 3.11 we can observe that:

- the shape of the heating curve is similar
- the overall temperature is lower in the 45 nm geometry
- there is no melting in the 45 nm case
- there is an inverted behavior of the polarization dependent temperature curves. In the 45 nm case the 90° is the "coldest" case
- in the 45 nm case the polarization dependent temperature curves are closer to each other

The complex trend of maximum temperature and melt area which are not trivially related to each other can be understood considering the effects due to the different heat source distributions when varying the polarization. In fig. 3.12 (i.e. the 0° polarization), the heat source is more concentrated on the upper wedge of the Fin and the temperature is higher in this region. If the temperature is high enough to melt it, the liquid phase has a higher reflectivity and consequently reduces the absorbed heat source, not allowing the further expansion of the melted region. Contrary, in the 90° case, the heat source is widespread, so the maximum temperature is closer to the average temperature. When there is melting, a wider part of the material (than in the previous case) is closer to the melting temperature so it is more prone to melt. In this case, the heat source absorbed by the system and not reflected by the liquid surface is sufficient to obtain a larger melting area.

Figure 3.13 shows the maximum temperature for different degrees of polarization for a larger structure (135 nm pitch). In this case we can see strong differences with respect to the previous simulations. Indeed we simulate melting also for the lowest value of the energy density (0.6 J/cm^2) for the 0° value of the polarization angle. Moreover the differences between the temperature curves are more pronounced, $\sim$ 1000 K, and the influence of the polarization is similar to the 45 nm case.

Snapshots of the temperature, phase and source for the 135 nm case are shown in in fig. 3.14. In this case it is easier to see the more uniform absorption of the electromagnetic radiation in the substrate in the FinFET

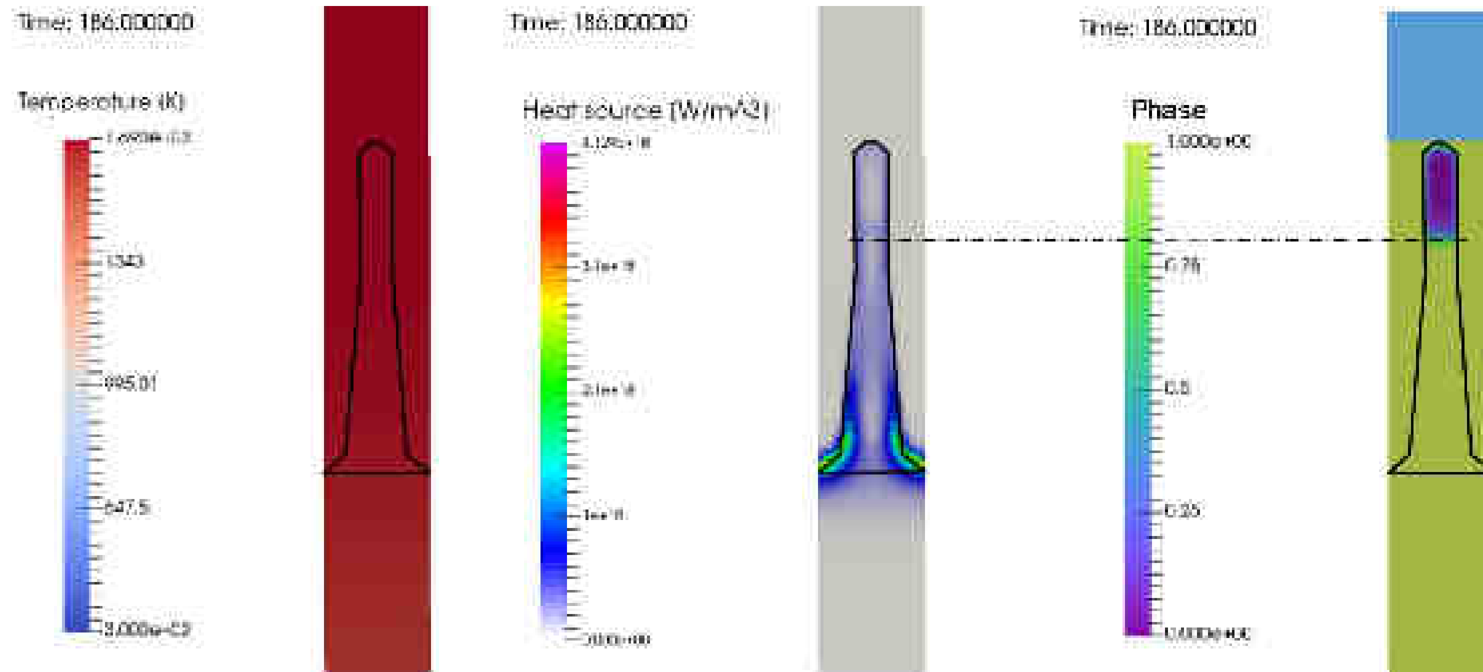

Figure 3.9: *From left to right, snapshots of temperature, heat source and phase field for a FinFET with a pitch of 35 [nm], irradiated at the fluence of 0.7 J/cm^2 and 90° of polarization at t=186 ns. In the phase field section green represents the solid domains, while violet is the liquid part. A dashed line helps to visualize the interaction between heat source and phase. The black line is the shape of the FinFET structure.*

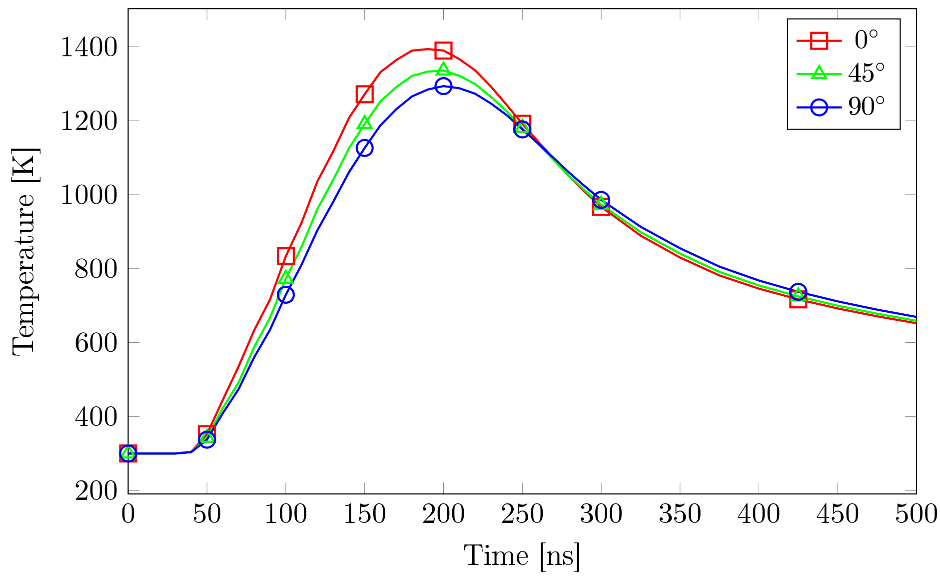

Figure 3.10: *Maximum temperature in the top-Fin region as a function of time for a FinFET with a pitch of 45 nm and an irradiation process with 0.6 J/cm^2 energy density for the values of 0°, 45° and 90° of the laser light polarization.*

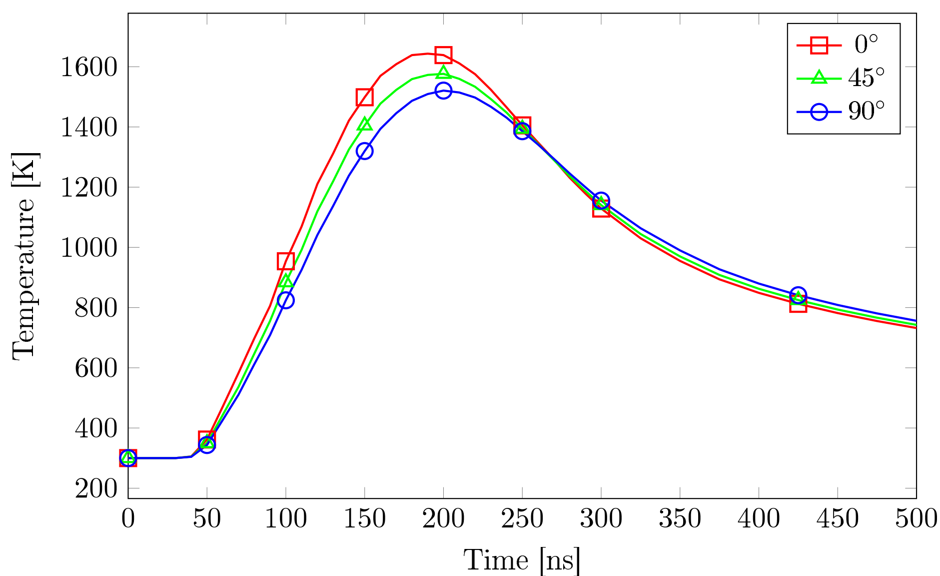

Figure 3.11: *Maximum temperature as a function of time in the top-Fin region for a FinFET with a pitch of 45 nm and an irradiation process with 0.7 J/cm^2 energy density for the values of 0°, 45° and 90° of the laser light polarization.*

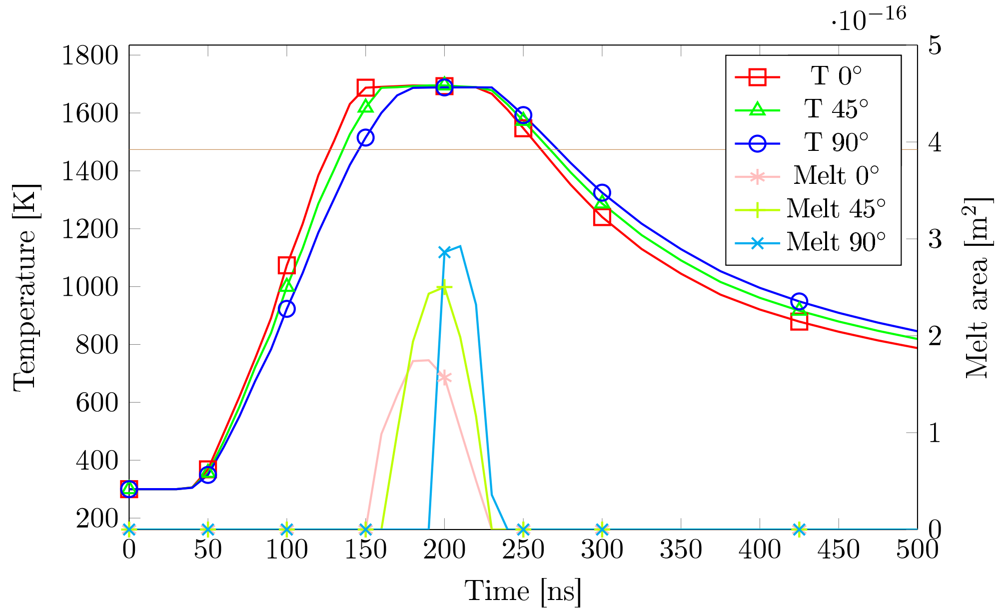

Figure 3.12: *Maximum temperature in the top-Fin region and total molten area as functions of the time for a FinFET with a pitch of 45 nm and an irradiation process with 0.8 J/cm^2 energy density for the values of 0°, 45° and 90° of the laser light polarization. Total top-Fin area is indicated by the horizontal line.*

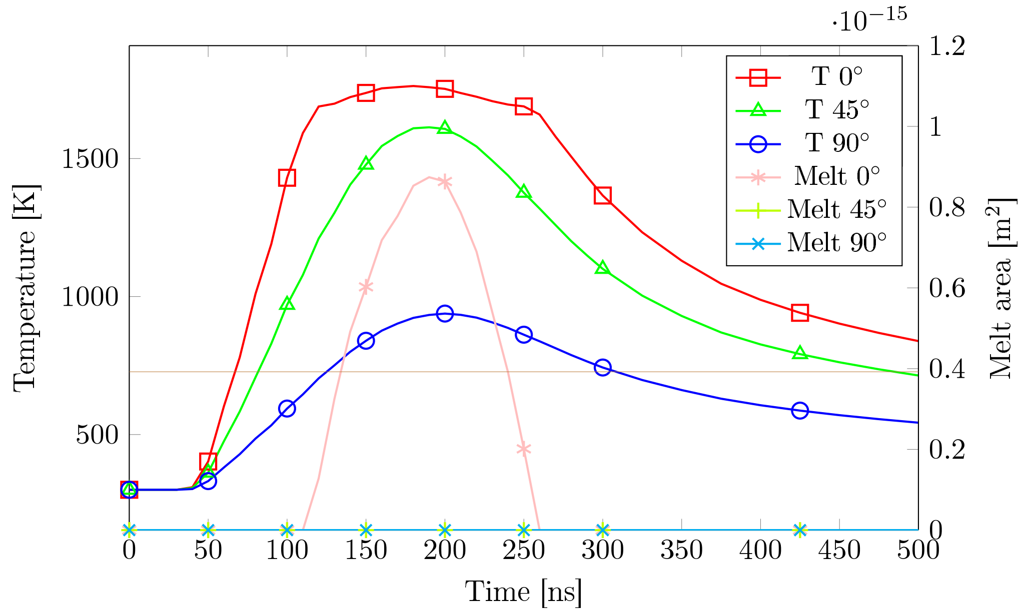

Figure 3.13: *Maximum temperature in the top-Fin region and total molten area as functions of the time for a FinFET with pitch of 135 nm and an irradiation process with 0.8 J/cm^2 energy density for the values of 0°, 45° and 90° of the laser light polarization. Total top-Fin area is indicated by the horizontal line.*

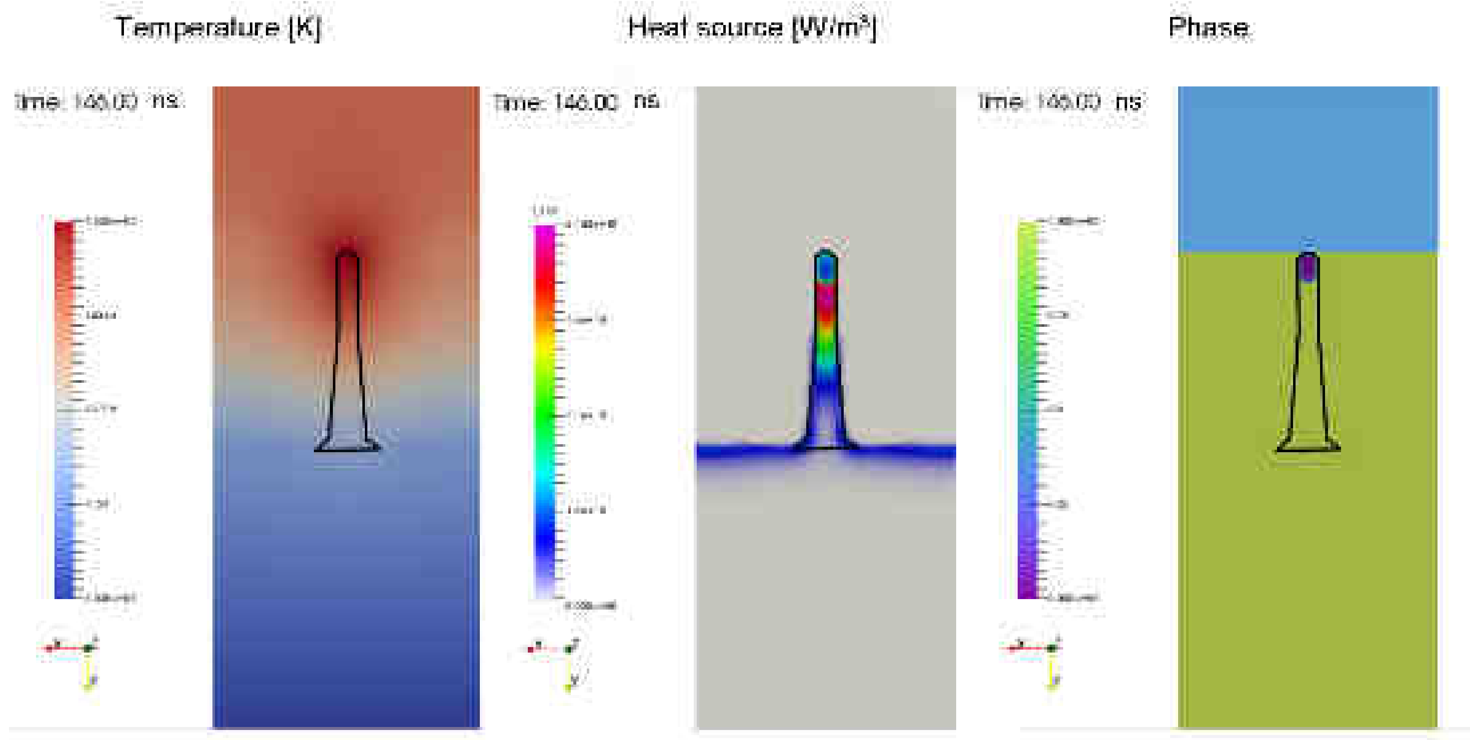

Figure 3.14: *From left to right, snapshots of temperature, heat source and phase field for a FinFET with a pitch of 135 nm, irradiated at the fluence of 0.6 J/cm^2 and 90° of polarization at t=186 ns. In the phase field section green represents the solid domains, while violet is the liquid part. A dashed line helps to visualize the interaction between the heat source and the phase. The black line is the shape of the FinFET structure.*

structure. Also in this case there is a strong relation between the phase and the heat source.

Figure 3.15 shows the heat source at 106 ns, 0.7 J/cm^2 for different polarizations and geometries (35 and 135 nm). All the samples are solid and the color scale is the same so they are directly comparable.

From the comparison of two cases, with small and large pitch, we can observe the following indications

- for a higher degree of the polarization, the source involves mainly the substrate than the top wedge;
- the larger pitch is globally more absorbing;
- the substrate under the Fin is shielded by the Fin structure itself;
- in the middle of the Fin there is a reduction of the source intensity;

3.3.1 Analysis of temperature geometry dependence

In fig. 3.16 we plot the maximum temperatures obtained in the whole simulation for different geometries and polarization angles. We report with an horizontal yellow line the melting temperature of silicon. Regarding the values obtained for the 35 nm case we have already shown that the temperature's highest value is obtained for 90°. Following the curves (which we could consider only as a simple guideline) we have the 45 nm case, with the inversion of the polarization trend, and so the lowest temperature is obtained for 90°. It is possible to see, as discussed, that for a pitch of 45nm the temperatures reached in the FinFET for the three polarization cases are closer to each other than those obtained for a pitch of 35 nm. For all the other cases starting from the 90 nm one (not shown so far) the polarization has the same qualitative result trends as the 45 nm case (i.e. 90° is the "coldest" case). However, there is a huge spread between the temperature reached in the FinFET for different polarization angles for a pitch interval between 90nm and 180 nm. It is obvious to note that the behavior of the system does not scale linearly with the polarization angle (strongly non linear for the 135nm case). The 0° is a melting case starting from 135 nm. The 180 nm case shows an overall decrease of the temperature for all polarization cases and a initial significant reduction in the temperature spreading with respect to the 135 nm pitch. In this case there is no melting for any polarization. Following the curves, there is the 225 nm case where the temperature continues to decline and there is a strong reduction in the temperature spreading. Starting from the 225 nm case, there is a stabilization of the trend. In fact, the following 270 nm case is very similar to the previous one. From the geometry of 225 nm and above the influence of polarization is very low and the temperatures are almost equal. This is explained by the similarity between the pitch value

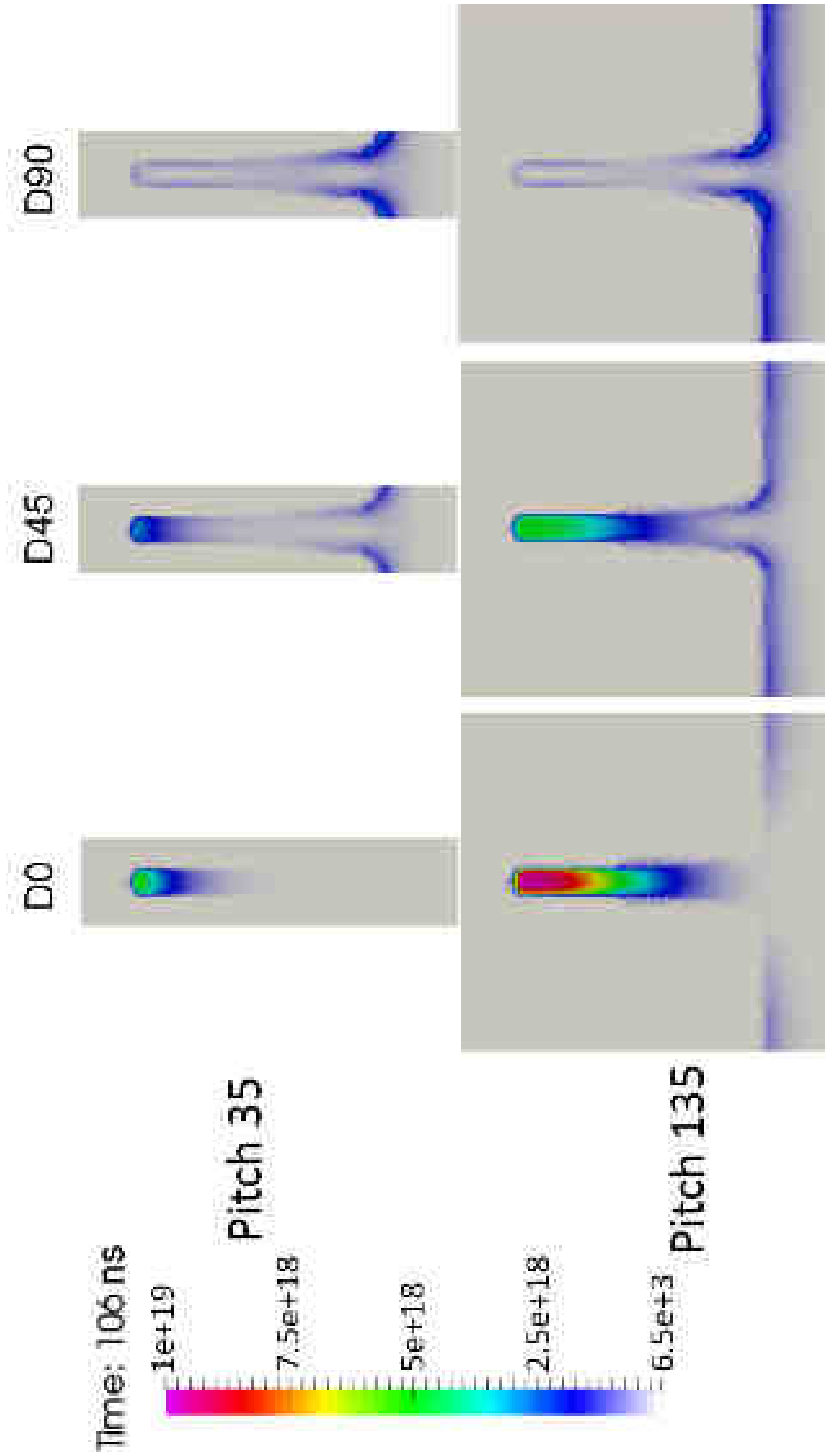

Figure 3.15: *Comparison for different values of pitch and polarization of the heat source, showing a time snapshot at t=106 ns. The plots share the same colorscale and are calculated with the same laser energy. The whole system is solid for all the cases shown.*

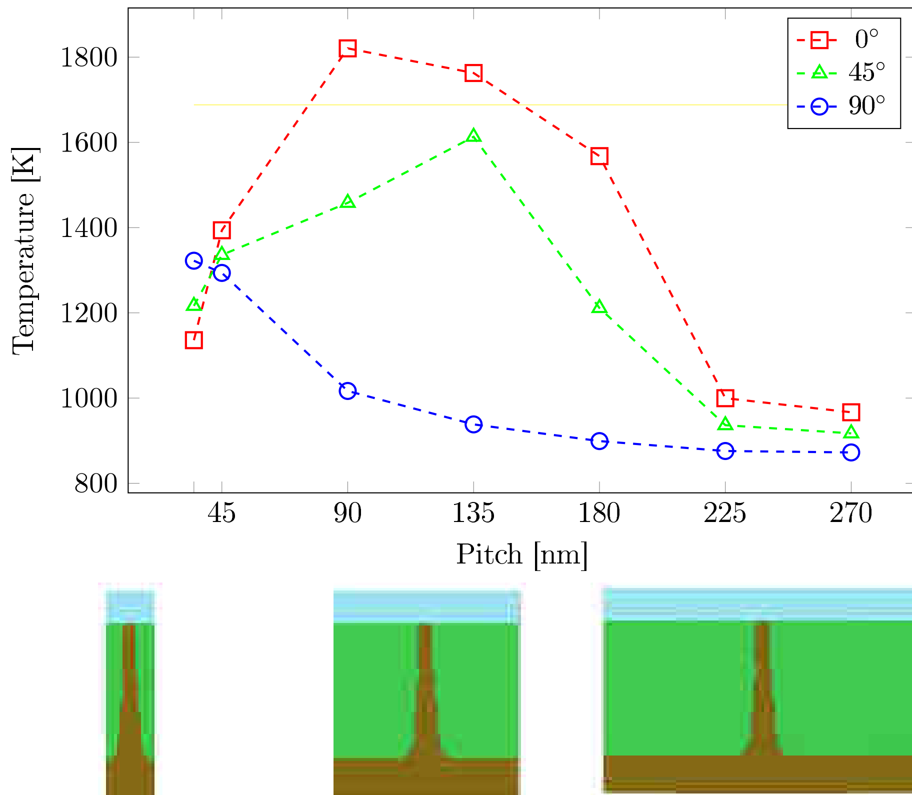

Figure 3.16: *Maximum temperature in the FinFET for different pitch and polarization values for the 0.6 J/cm² fluence case.*

and the wave length of the laser (308 nm), so mutual interactions are less important. The maximum temperature for the larger pitches is lower since the concentration effect of the Fin structure is missing and the Fin is heated with a similar modality as the substrate, see also fig. 3.15.

The 0° polarization (see fig. 3.17) case shows a complex response to the process with the dimension of the pitch. The increase of the laser fluence increases the temperature. Small and large geometries reach lower temperatures than intermediate ones.

The 45° polarization case shows a similar behavior as in the previous case (see fig. 3.18), with a particular interaction between temperature and pitch value. In this case there is no switching in temperature and, as expected, increasing the fluence leads to an increase in temperature. A yellow horizontal

For the 90° polarization angle (see fig. 3.19 where we plotted the maximum temperature in the FinFET for different pitch values and laser energies), the heating affects more the substrate, so the behavior when increasing the pitch is driven by the larger heating dispersion on the substrate for larger pitches. Increasing the energy monotonically increases the temperature over

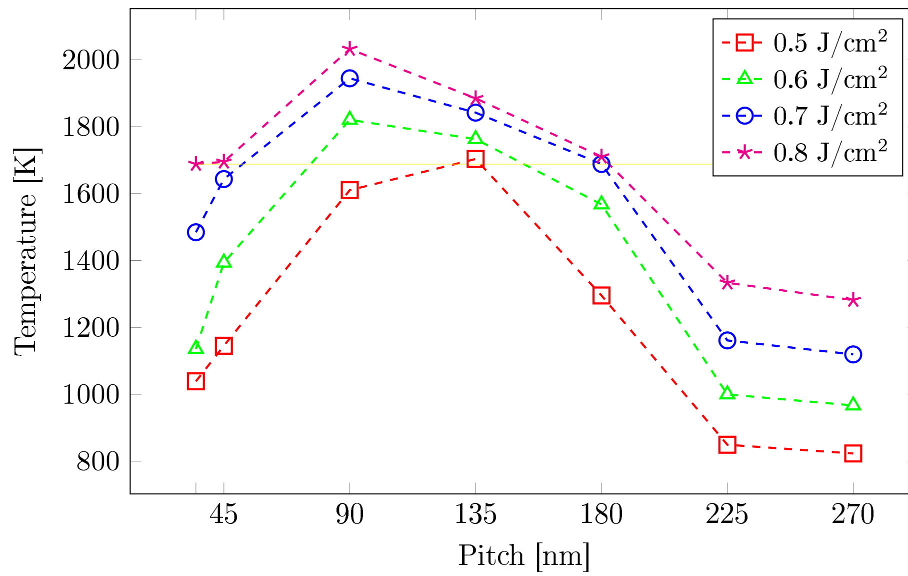

Figure 3.17: *Global maximum temperature for different laser energies, for the 0° polarization case. A yellow horizontal line represents the melting temperature of silicon.*

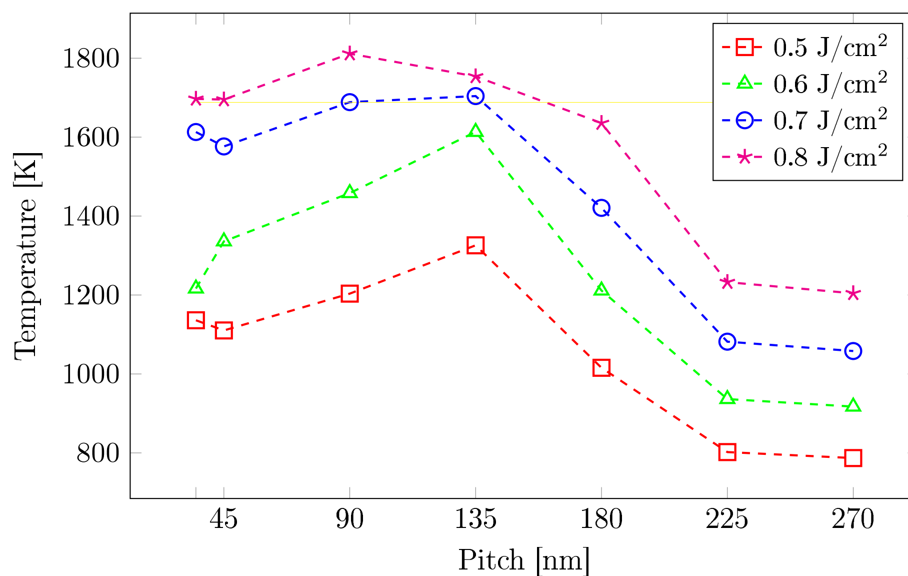

Figure 3.18: *Global maximum temperature for different laser energies, for the 45° polarization case. A yellow horizontal line represents the melting temperature of silicon.*

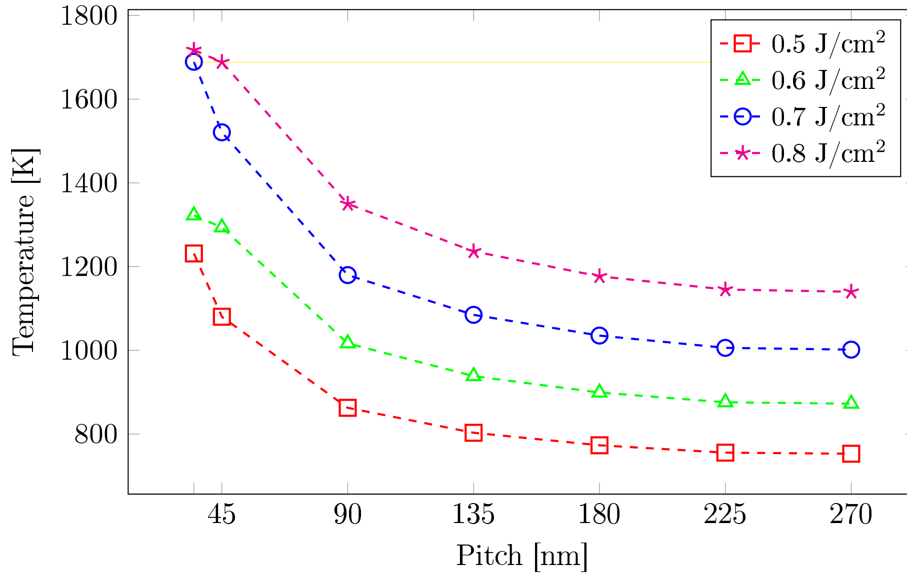

Figure 3.19: *Global maximum temperature for different laser energies, for the 90° polarization case. A yellow horizontal line represents the melting temperature of the silicon.*

all pitch values. Only the thinner geometries, under hight fluence have melting, in fact, the temperature is above the melting temperature of the silicon (the yellow horizontal line).

3.3.2 Analysis of molten area versus geometry dependence

From fig. 3.20 to 3.22 we plot the melt area for different geometries and laser fluences fixing the polarization angle. We plot the total top-Fin and bottom-Fin areas with horizontal lines, in brown and black, respectively. In the 0° case, the first of the series, for the 35 nm case and all the cases above 225 nm there is no melting for all fluences. For the other cases there is no clear trend (due to again to the strong non-linearity) so we have to study each curve individually. For the 0.5 J/cm^2 there is only a slight melting in the 135 case. For the 0.6 J/cm^2 case, the melting occurs only in the 90 and 135 nm cases and with a greater area in the 90 nm case with respect to the 135 nm one. The melted area involved is intermediate between the first and the bottom, brown and black horizontal lines, respectively. Increasing the fluence to 0.7 J/cm^2, there is an increase in the molten area for the 90 nm case, a reduced increase for the 135 nm and also the 180 nm case begins to melt. For the last case studied we begin to have melting also for the 35 and 45 nm cases.

In the case of 45°, the second graph of the series (fig. 3.21), in the cases of 0.5 and 0.6 J/cm^2, there is no melting for any geometry. In the 0.7 J/cm^2

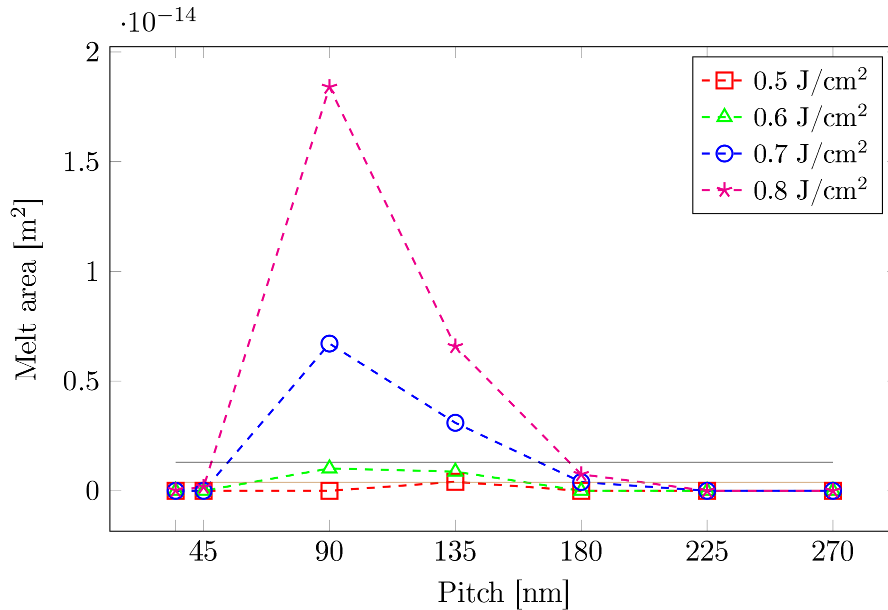

Figure 3.20: *Global maximum melt area for different laser energies, for 0° polarization case. Total top-Fin and bottom-Fin areas are indicated by the horizontal lines.*

case only the 90 nm and 135 nm geometries show melting. In the 0.8 J/cm^2 35 and 45 nm case begin to melt. The 90 nm case now has the greater melting area than the 135 nm case. For all fluence values the 180, 225 and 270 geometries show no melting.

In the 90° polarization case, the last of the series (fig. 3.22), all the geometries for all fluence values have no melting except for the 35 and 45 nm cases. In the 0.5 and 0.6 J/cm^2 cases there is no melting for all the geometries. For the 0.7 J/cm^2 case, the 35 nm geometry has a melted area equal to the top-Fin, represented by the brown horizontal line. For the latter case, 0.8 J/cm^2, there is a full melting of the 35 nm geometry (well over the bottom-Fin, represented with a horizontal black line) and the 45 nm case begins to melt.

In fig. 3.23 we plot the melt area in the 0.7 J/cm^2 case for different polarizations and geometry values. In the 0° case there is no melting for the 35 nm and 45 nm geometries, an increased melted area for 90 nm and a decrease for 135 nm and 180 nm cases. The 225 and 270 nm cases do not show melting at all. In the 45° case there is no melting for 35 nm and 45 nm and the geometries above 180 nm. The 90 nm and 135 nm show melting, and in particular in this case the 135 nm has a greater area with respect to the 90 nm one. The 35 nm geometry shows some melting in the 90° polarization case, while the other geometries have no melting. For the 35 nm geometry we can pass thought no melting in the 0° case to a complete melting of

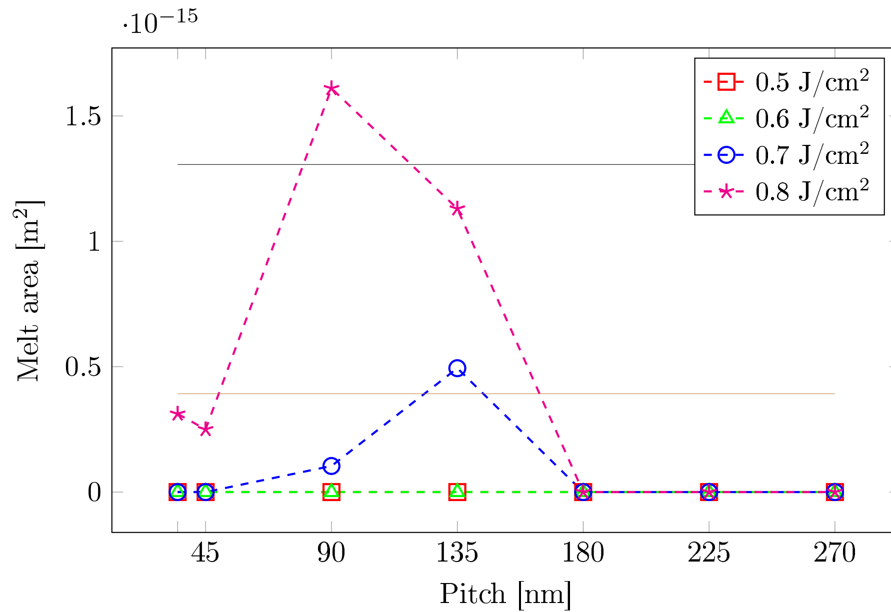

Figure 3.21: *Global maximum melt area for different laser energies, for the 45° polarization case. Total top-Fin and bottom-Fin areas are indicated by the horizontal lines.*

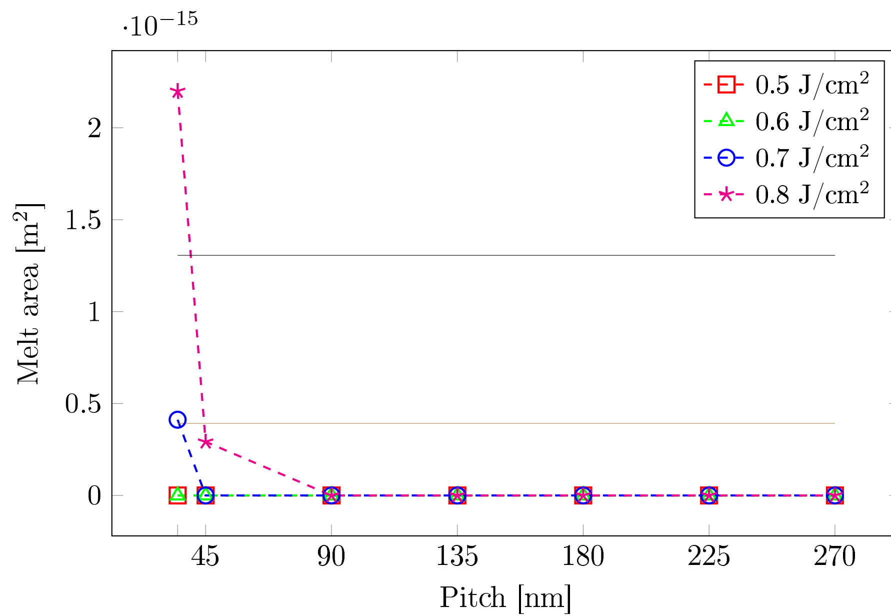

Figure 3.22: *Global maximum melt area for different laser energies, for the 90° polarization case. Total top-Fin and bottom-Fin areas are indicated by the horizontal lines.*

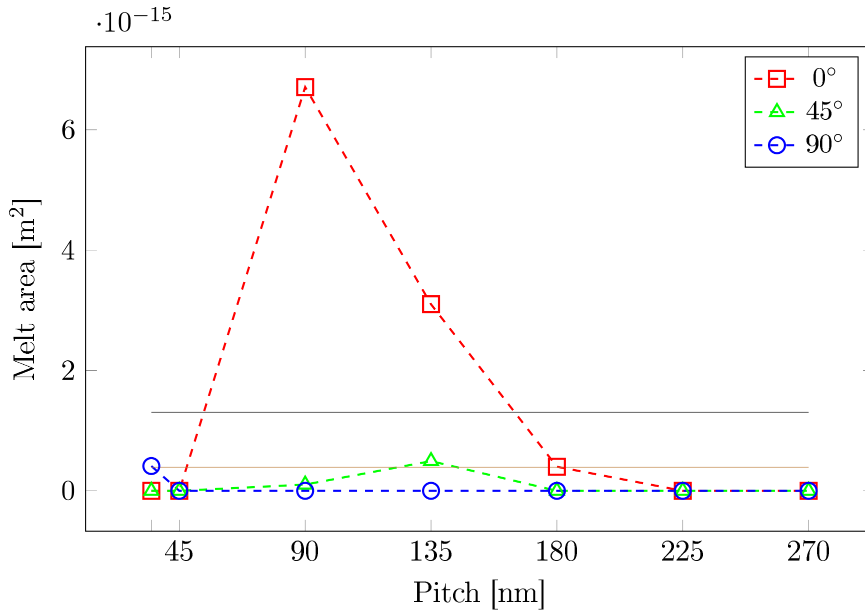

Figure 3.23: *Melt area over time for different polarization values, for the 0.7 J/cm^2 case. Total top-Fin and bottom-Fin areas are indicated by the horizontal lines.*

the FinFET for the 90° case. In the 45 nm case all the simulation leads to a melting area around the top-Fin. For the 90 and 135 nm geometries in all cases where melting occurs is well over the whole Fin area. The 35 nm geometry shows melting only for the 90° of polarization case, while the 45 nm one never shows melting with this fluence. The 90 nm and the 135 nm geometries can pass from no melting (90°) to the deep melting of the substrate (the area of the whole Fin is represented by the black horizontal line), while the 180 nm can reach only the melting of the top-Fin (the brown horizontal line). The 225 nm and 270 nm geometries never show melting.

3.4 Tuning selectivity through polarization

In the modern semiconductor manufacturing is often important to localize the heating and/or the melting only on a wanted area, leaving the other part of the sample less involved [35]. With the LA combining geometry and polarization this task can be achieved. The figures from 3.24 to 3.27 show the maximum temperature over time for different polarization angles and for different domains. We concentrate our interest in the top of the fin (TF) and in the substrate (Sub) region.

Starting with fig. 3.24, that reports a FinFET structure of 35 nm under 0.7 J/cm^2, the temperature shape is the usual one, the 90° is the hottest.

In this case the importance of the graph is in the relation between similar color curves. The difference in the 0° case for the FinFET and the substrate is 176 K, for the 45° case is a little less while in the 90° the difference is very low. In the latter case we underline that there is a melting in the top-Fin (the temperature plateau), while the substrate continues to grow up the temperature. For all the curves at the end of the simulation the temperature of the top-Fin and the substrate are the same due to the thermal diffusivity. The following fig. 3.25 shows the 45 nm case 0.7 J/cm^2. In this case increasing the polarization, we observe a decrease of the TF temperature and an increase of the Sub-temperature, that means that for the 0° case the difference TF-substrate is 235 K, while in the 90° is only 49 K. Figure 3.16 shows the maximum temperature of the top of the FinFET and of the substrate, geometry 135 nm, 0.7 J/cm^2 case for different polarization angle. The use of the 90° is useful for a uniform heating of the sample. The use of 0° leads to the melting of the whole top-Fin while the substrate remains 230 K colder. We underline that the height of the Fin, so the maximum distance from the top to the substrate, is only 100 nm. At the end of the simulation the temperatures, for each polarization value, reach the same value due to the thermal conductivity. The difference in the 90° case is the lowest of this series.

Increasing the pitch value we obtain that the differences are less visible, see fig. 3.27 where the maximum differences are 76 K and 28 K, for the 0° and 90° cases, respectively.

In fig. 3.28 we plot the maximum temperature in the top-Fin (TF) and in the substrate(Sub) under 0.8 J/cm^2 case for different polarizations and geometry values. The top-Fin curves are drawn with filled marks and intense color, while the substrate one with empty marks and lighter color. We report with a horizontal yellow line the melting temperature of silicon. With the 0° value of polarization there is, for all geometries, a great difference between the TF and the substrate, also in the cases where there is melting. In the case of 45° of polarization the difference between TF-Sub is, also in this case, very high. With this polarity there is no melting. In the last case of polarization, the 90°, the curves TF-Sub are, for all geometries, very close, which indicates a uniform heating of the sample. Regarding the values obtained for the 35 nm case we have already shown that the temperature's highest value is obtained for 90°. Following the curves (which we could consider only as a simple guideline) we have the 45 nm case, with the inversion of the polarization trend, and so the lowest temperature is obtained for 90°. It is possible to see, as discussed, that for a pitch of 45nm the temperatures reached in the FinFET for the three polarization cases are closer to each other than those obtained for a pitch of 35 nm. For all the other cases starting from the 90 nm one (not shown so far) the polarization has the same qualitative result trends as the 45 nm case (i.e. 90° is the "coldest" case). However, there is a huge spread between the temperature reached in the FinFET for different

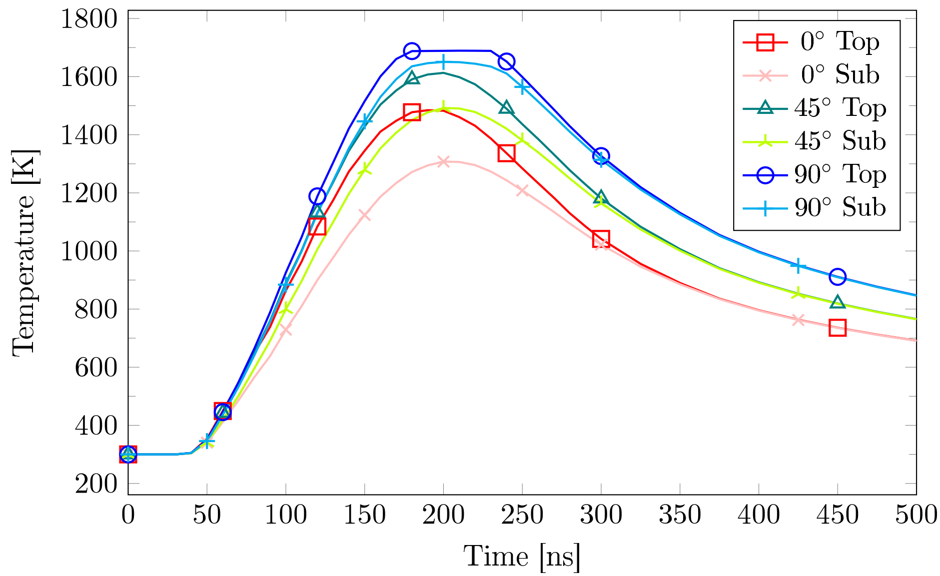

Figure 3.24: *Comparison between the maximum temperature in the top of the Fin (TF) and in the substrate (Sub), pitch value of 35 nm and 0.7 J/cm^2 of laser fluence.*

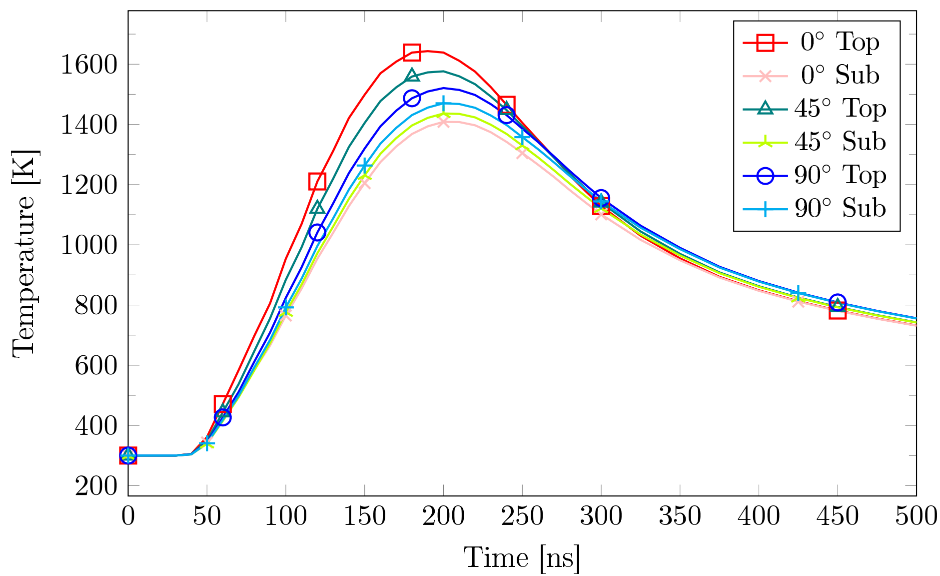

Figure 3.25: *Comparison between the maximum temperature in the top of the Fin (TF) and in the substrate (Sub), pitch value of 45 nm and 0.7 J/cm^2.*

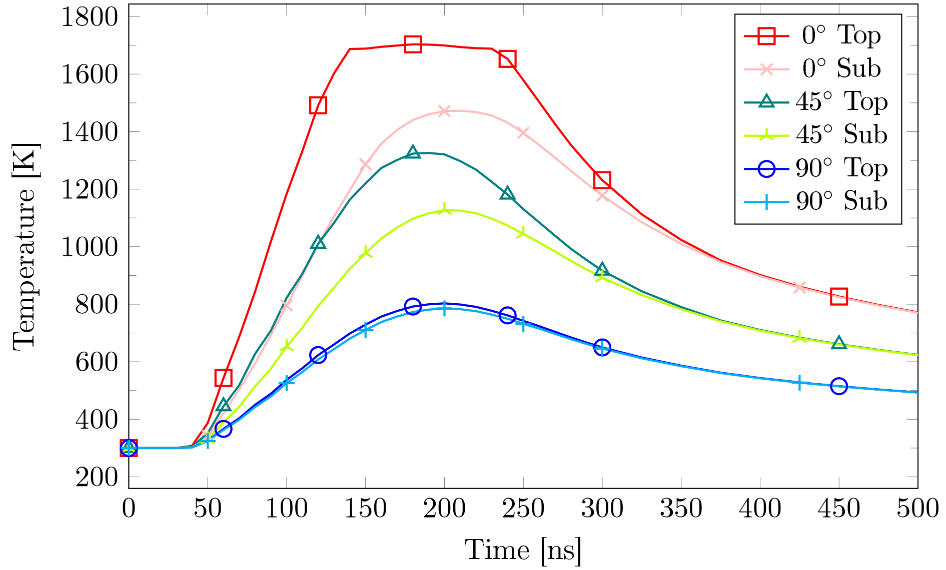

Figure 3.26: *Comparison between the maximum temperature in the top of the Fin (TF) and in the substrate (Sub), pitch value of 135 nm and 0.5 J/cm^2.*

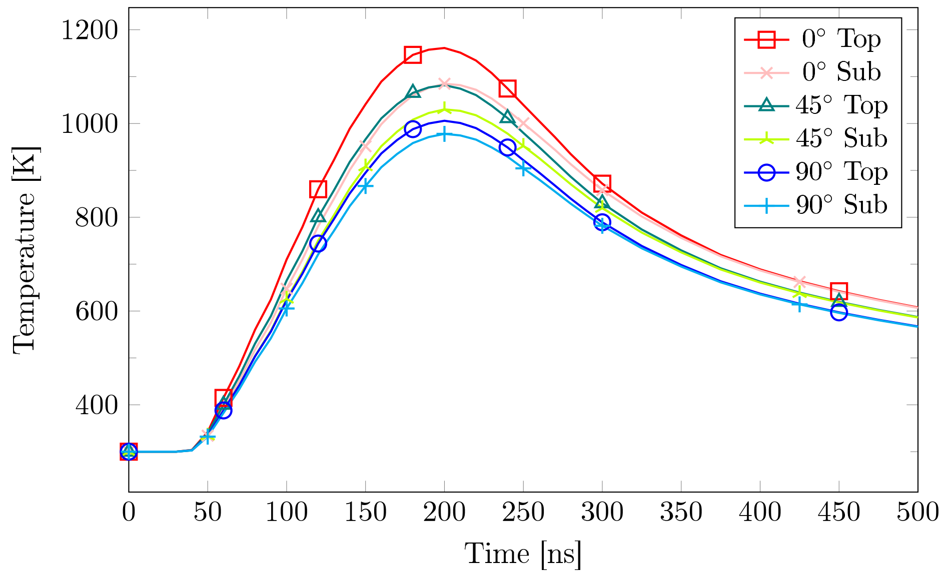

Figure 3.27: *Comparison between the maximum temperature in the top of the Fin (TF) and in the substrate (Sub), pitch value of 225 nm and 0.7 J/cm^2.*

polarization angles for a pitch interval between 90nm and 180 nm. It is obvious to note that the behavior of the system does not scale linearly with the polarization angle (strongly non linear for the 135nm case). The 0° is a melting case starting from 135nm. The 180 nm case shows an overall decrease of the temperature for all polarization cases and a initial significant reduction in the temperature spreading with respect the 135nm pitch. In this case there is no melting for any polarization. Following the curves, there is the 225 nm case where the temperature continues to decline and there is a strong reduction in the temperature spreading. Starting from the 225 case, there is a stabilization of the trend. In fact, the following 270 nm case is very similar to the previous one. From the geometry of 225 nm and above the influence of polarization is very low and the temperatures are almost equal. This is explained by the similarity between the pitch value and the wave length of the laser (308nm), so mutual interactions are less important. The maximum temperatures for large pitch is lower since the concentration effect of the Fin structure is missing and the Fin is heated with a similar modality as the substrate, see also fig. 3.15.

In the 45° case there is melting for 35 nm and 45 nm, an increase for 90 nm and a slight decrease for the 135 nm case. The cases above show no melting. The 35 and 45 nm geometries show some melting in the 90° polarization case, while the others have no melting. For the 35 nm geometry we can pass thought no melting in the 0° case to a complete melting of the FinFET for the 90° case. In the 45 nm case all the simulation leads to a melting area around the top-Fin. For the 90 and 135 nm geometries in all cases where melting occurs is well over the whole Fin area.

The figures from 3.29 to 3.31 show the maximum temperature in the top-Fin (TF) and in the substrate (SUB) for different fluence and pitch values for various polarization angles. With respect to each energy fluence, the curve uses a color with filled marks for the top-Fin and a lighter color with empty marks for the corresponding substrate (SUB) curve. The 0° polarization case shows a complex behavior with the dimension of the pitch. The differences between the top-Fin and substrate temperature have generally an increase for the intermediate pitch value. With high value of fluence the differences are less consistent due to the thermal plateau of the melting that occurs in the top-Fin while the substrate continues to heating up reducing the difference, see fig. 3.29.

The 45° polarization case is quite similar to the previous one, the differences in term of temperature between the topFin and substrate are remarkable for the mean pitch values. See fig. 3.30 where is plotted the maximum temperature in the FinFET for different pitch value and laser energy for the top-Fin and the Substrate.

The 90° polarization case affects more the substrate and almost all the simulations remain under the melting threshold. The differences between the top-Fin and the substrate are always low, with a total average value of 45

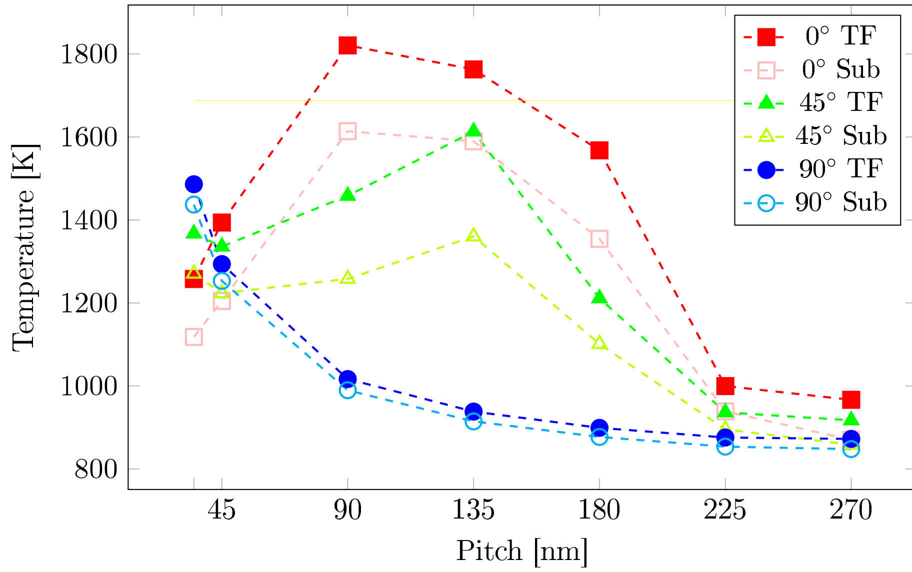

Figure 3.28: *Maximum temperature in the FinFET for different pitch and polarization values, in the 0.6 J/cm² case. A yellow horizontal line represents the melting temperature of the silicon.*

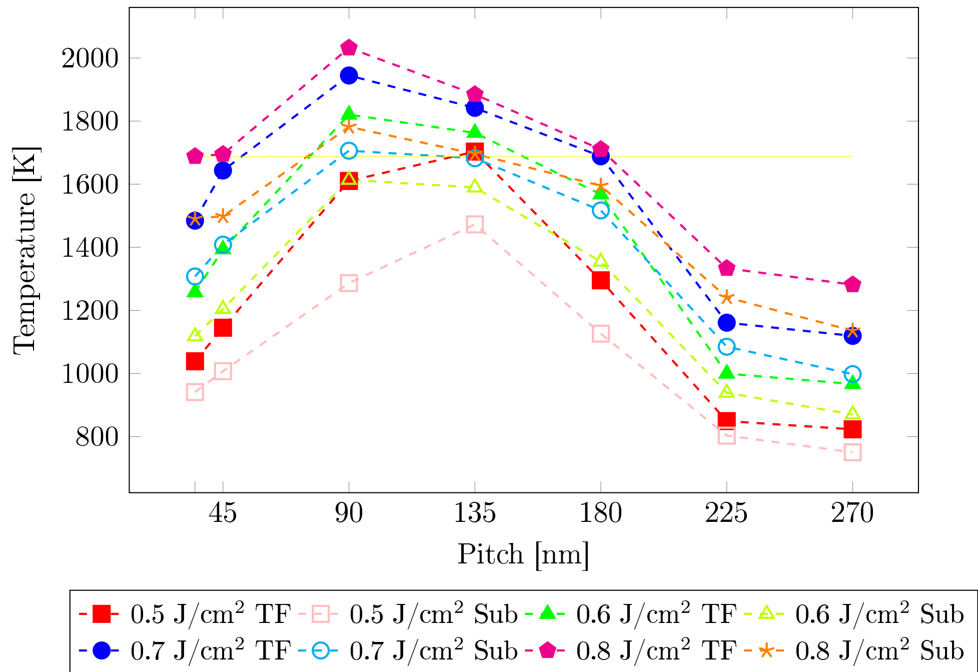

Figure 3.29: *Maximum temperature over time for different laser energies, for 0° polarization. A yellow horizontal line represents the melting temperature of the silicon.*

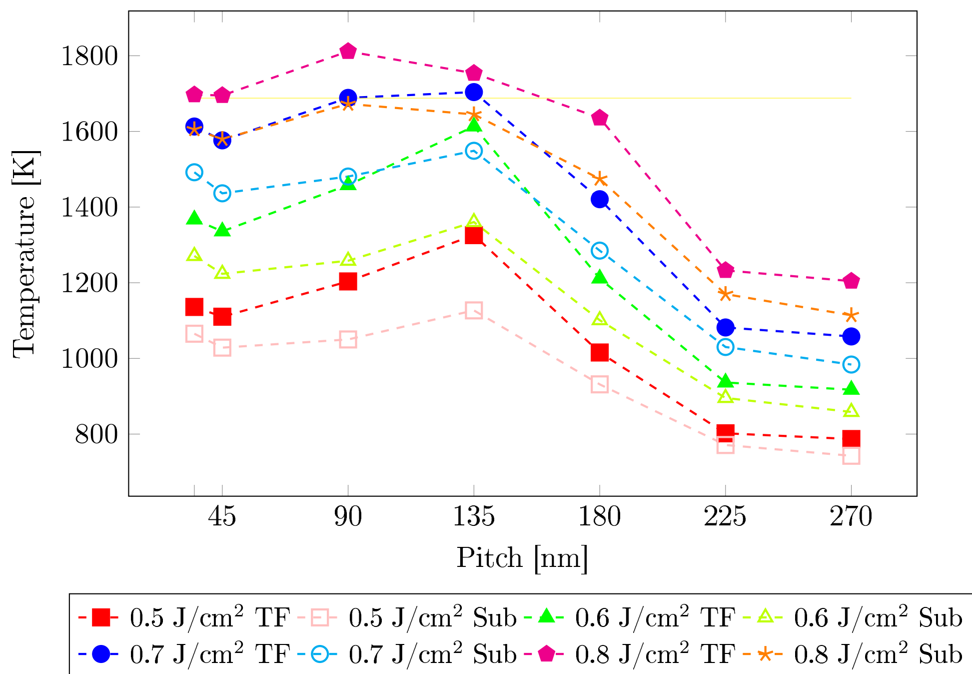

Figure 3.30: *Maximum temperature over time for different laser energies, for 45° polarization. A yellow horizontal line represents the melting temperature of the silicon.*

K. See fig. 3.31 where is plotted the maximum temperature in the FinFET for different pitch value and laser energy for the top-Fin and the Substrate.

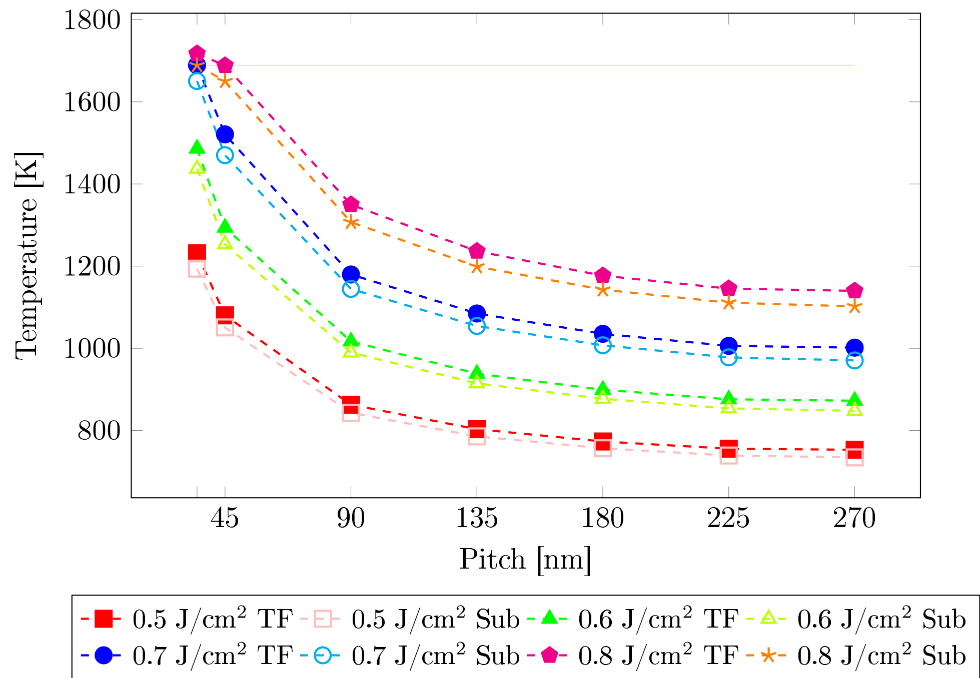

Figure 3.31: *Maximum temperature over time for different laser energies, for 90° polarization. A yellow horizontal line represents the melting temperature of the silicon.*

3.5 Validation tests

In this section we compare our results with the experimental data obtained in a campaign of tests performed by our partner SCREEN LASSE and specifically designed to validate the code. In particular, we decided to use global information on a large set of periodic structures and to apply Scanning Electron Microscopy (SEM) in planar configuration to investigate the quality of the samples dividing a large number of SEM analyses into three sets corresponding to increasing levels of damage induced by the irradiation.

- In **level 0** the structures remained unchanged with respect to the pre-LA configuration. This category corresponds to samples where melting did not occur in any zone of the irradiated structure, and therefore the temperature did not reach high values, (fig. 3.32 left panel shows an example of the structure after the LA process classified with this level).
- For samples in the **level 1** category, as shown in the middle of fig. 3.32, we notice that the main structure remains unchanged. However, some surface limited imperfections emerge, so we can imagine that fusion occurred (which would explain the small imperfections due to solidification) but that is limited to the Fin's areas: the temperature did not reach high values (close and above the melting point) in the substrate and the regrowth in some cases did not cause defects).
- For **level 2** category the structure during the process has undergone major structural changes, probably due to thermal stresses and the regrowth from not fully epitaxial conditions, and hence as seen in fig. 3.32 (right panel) the visual analysis indicates an empty and an asymmetric shape. In this category we have included cases where the substrate has melted and as a consequence high temperatures have been reached.

With this experimental technique we have to connect the damage with the evolution of the process and this is not so trivial. The SEM image only says if there are defects, but quantitative values on how, when or why these defects are present are not accessible with this technique. The intermediate cases have not distinctive features so a slight melting or a full melting of the FinFET could lead to the same damage value. However, global information on a large area is valuable, as early tests, whereas local point to point variations need statistics of data in cross section configurations (i.e. also using most expensive TEM analyses). This is part of the future planned experiment activity. Considering these issues we could also expect some difference between simulations and experiments. Figure 3.33 reports the comparison between experiment and simulation for the three laser polarization cases (0° on the left panel, 45° in the middle panel and 90° in the right panel), as a function of the laser energy density for a geometry of 45nm pitch. In the y

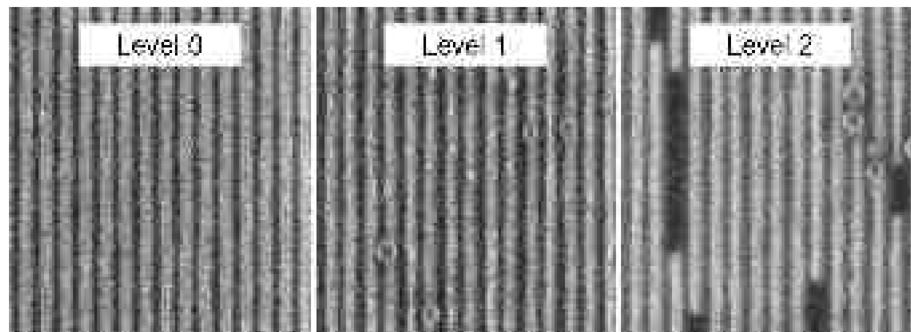

Figure 3.32: *SEM images representative of the meaning of the level of damage.*

scale we report the level of damage already discussed. We note that in spite of the possible strong variance of the experimental procedure of the damage classification the agreement is overall very good with important positive feedback also for the sensitivity to the polarization changes.

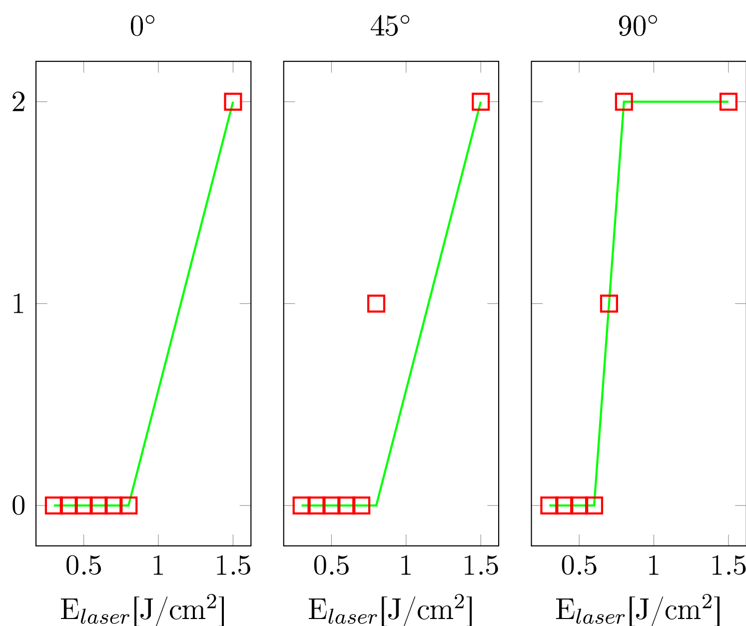

Figure 3.33: *Comparison between experimental (red square) and simulated (green line) melting threshold for the case 45 nm.*

3.6 Conclusion

In this section we have discussed a fully TCAD procedure for the design of the LA process in a FinFET device. We discussed the influence of the geometry and polarization in the simulated laser treatment of the sample. In particular it is not always simple and easy to understand from a black approach to the process design how:

- the geometry has a huge impact on the results;
- different pitch values change completely all the process effects;
- the polarization allows to focus the light on different parts of the system;
- the material choice is important to fine-tuning the process

Our model is able to simulate properly all these feature interactions allowing to bypass the major problems of a process optimization performed on a pure experimental basis.

4

Advanced modeling: Explosive Crystallization Phenomenon and Alloys

4.1 Introduction

In many of the applications to the semiconductor technology, LA is preceded by a process (e.g. impurities' implantation or low temperature deposition) producing strongly disordered or amorphous (pure or alloys) thin film materials. Moreover, for the majority of the proposed conditions, LA induces localized melting and the ultra fast recovering of the crystalline order. This process promotes the material modifications (e.g. the transition of the amorphous regions in nano/micro crystalline ones or the redistribution of the alloy relative concentration) within a few tens of nanometers thick region close to the sample surface. In melting conditions, the Explosive Crystallization (EC) phenomenon occurs almost ubiquitously during these processes due to the formation of a strongly under-cooled liquid layer. This phenomenon usually hinders the process control and, as a consequence, the material properties and its quality after the irradiation are difficult to predict. This difficulty is also caused by the lack of a consistent model able to simulate the concurrent kinetics of the amorphous-liquid and liquid-crystal interfaces.

Another difficult task is to control and simulate the LA in an alloy (e.g. SiGe) when alloy fraction varies in time and space, and as a consequence, the thermodynamic parameters change. In this chapter we discuss the extension of the formalism in order to consider explosive crystallization and alloys effects in the simulations. The modeling results will be also validated by means of wide comparison with in-situ and ex-situ characterization of

processed samples.

The explosive kinetics is recovered naturally by the model solutions since the unbalance of the thermodynamic parameters of the three concurring phases can be rightly implemented.

4.2 The Mechanism of Explosive Crystallization

The EC mechanism in covalent elemental semiconductors (Si and Ge) is known (see e.g. Ref. [36] and references therein) as the result of a significant larger (negative) latent heat for the liquid to crystal phase transition with respect to the one (positive) for the amorphous to liquid transition. Without loss of generality, the mechanism is explained in fig. 4.1 for a particular initial state (amorphous layer on the top of the crystal bulk) which is a schematic of the experimental samples we will analyze in the following, fig. 4.1a. Due to e.g. the laser pulse heating, the temperature in the sample grows up and the amorphous layer can melt and interface kinetics is governed by the energy and mass balance laws of liquid-amorphous inter-phase (fig. 4.1b). In particular, the velocity of the melting front is of the order of few m/s. The temperature field in the liquid phase is close to melting point of the amorphous phase, i.e. the liquid is in an under-cooled condition with respect to the crystalline phase which in turn is the more stable in this temperature range. As a consequence the liquid portion tends to spontaneously solidify. After the nucleation time, which depends on many factors like the local temperature and the presence of impurities, the liquid solidifies and there is the creation of a second transition front (from liquid to crystalline) which is governed by crystal-liquid inter-phase characteristics. The latent heat of the solidification of the crystal is larger than the one for the melting of the amorphou. Hence, there is an excess of heat that leads to the melting of the amorphous layer that can self-sustain the phenomenon: i.e. due to this positive feedback the process is self-propagating (fig. 4.1c). In this condition the velocity of the two self-sustaining melting fronts is about one order of magnitude larger with respect to the single interface case. The fusion process ends when the energy released is insufficient to melt more amorphous material or when the polycrystalline-liquid front reaches the crystalline bulk (fig. 4.1d). At the end of the EC there is a poly-crystalline layer that replaces the amorphous one, upon the unchanged crystalline bulk, see fig. 4.1e. In a 3D real system the nucleation of the polycrystalline is a random phenomenon in space, as a consequence the melting front spreads all over the specimen, with multiple fronts so the process could stop before reaching the amorphous/crystal interface. We would like to underline that after the first solidification event the power released by the laser is less relevant with respects to the evolution of the system, since the process is governed only by the melting-solidification evolution. At the end of the EC phenomena there

is a nano- poly-crystalline layer upon a crystal bulk. Three possible scenarios arise also depending on the laser energy density:

1. The fluency of the laser is insufficient to increase further the sample temperature which then tends to decrease by means of diffusion. In this case the sample experiences EC only;

2. if the laser source is sufficiently intense a secondary melting of the new polycrystalline layer can occur in the case that the maximum of the temperature field reaches the crystal melting point, see fig. 4.2a. This evolution is characterized by the fact that the melting front does not reach the amorphous/crystalline initial interface. At the end of the process we found a polycrystalline layer upon the unmodified original crystal bulk, like in fig. 4.2b.

3. if the laser source was even more intense than the previous case, the secondary fusion front could overcome the original A/C interface, see fig. 4.3a. At the end of the process, the sample solidification would be resumed following the order of the crystalline phase, see fig. 4.3b.

In the 2 and 3 cases the secondary liquid-solid melt front evolves conventionally since, after the EC, the system presents only crystal thermal properties.

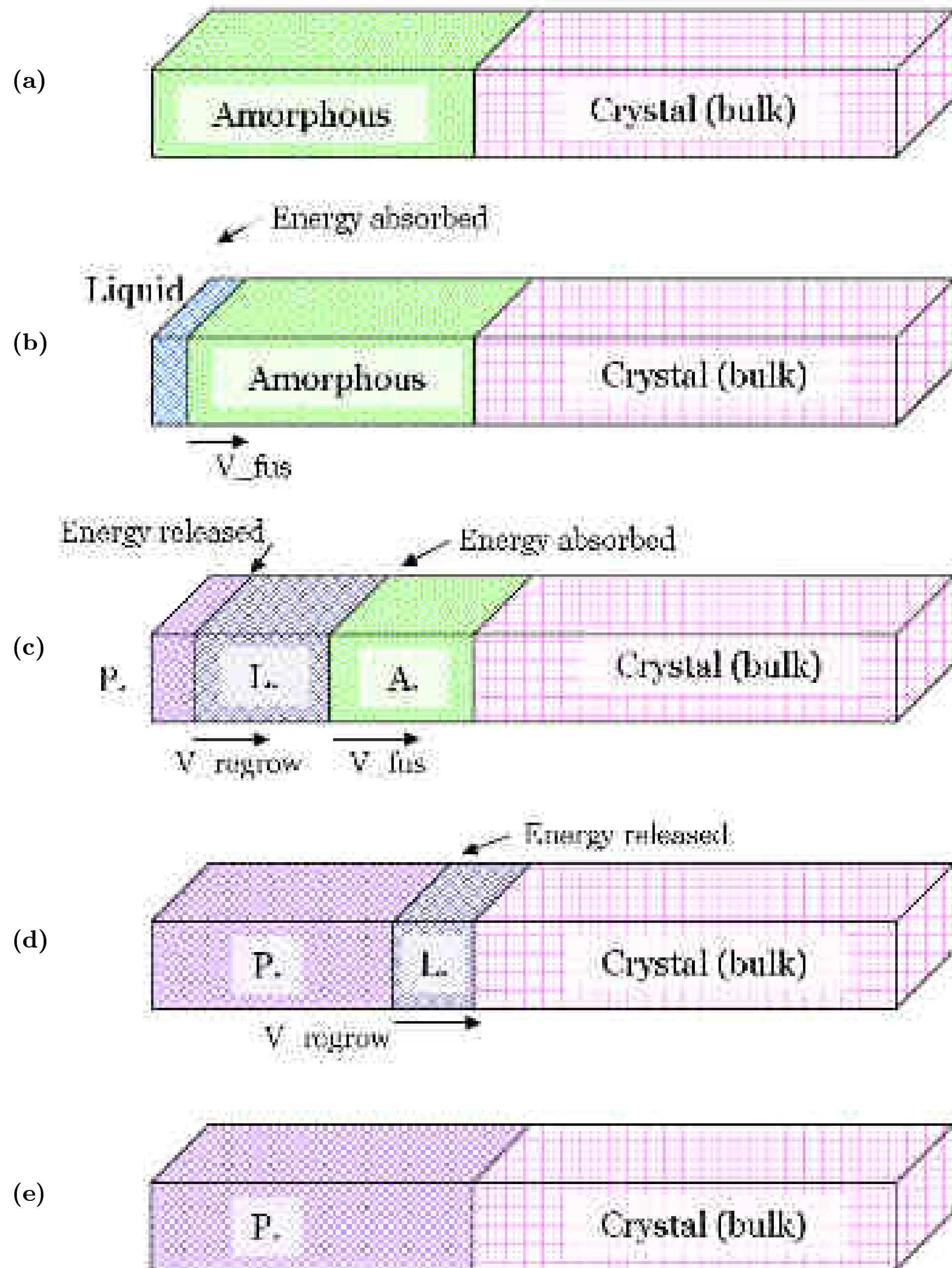

Figure 4.1: *Schematic of the main evolution stages of the explosive crystallization. The laser source heats the sample from the left.*

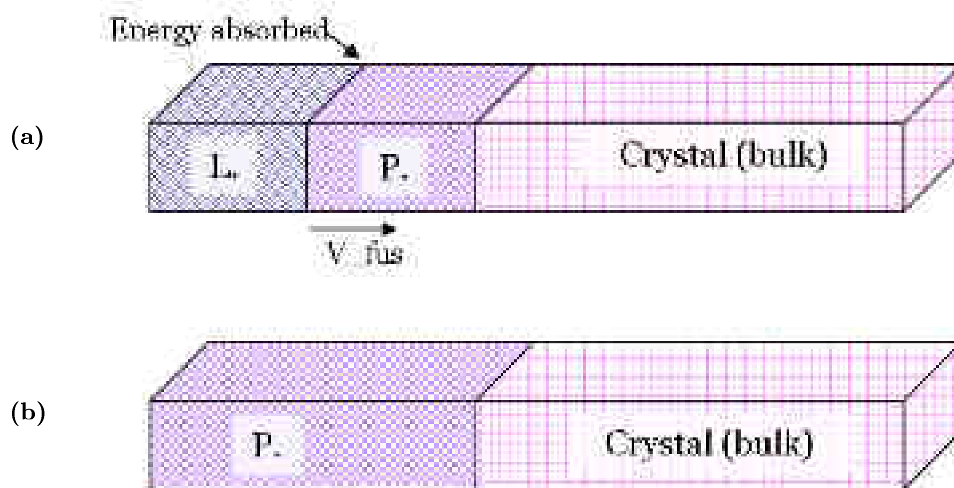

Figure 4.2: *Schematic of the secondary melting evolution for a low fluence case. The laser source heats the sample from the left. The secondary melting front does not reach the A/C interface, subfigure a. At the end of the process a polycrystalline layer is the surface layer, subfigure b.*

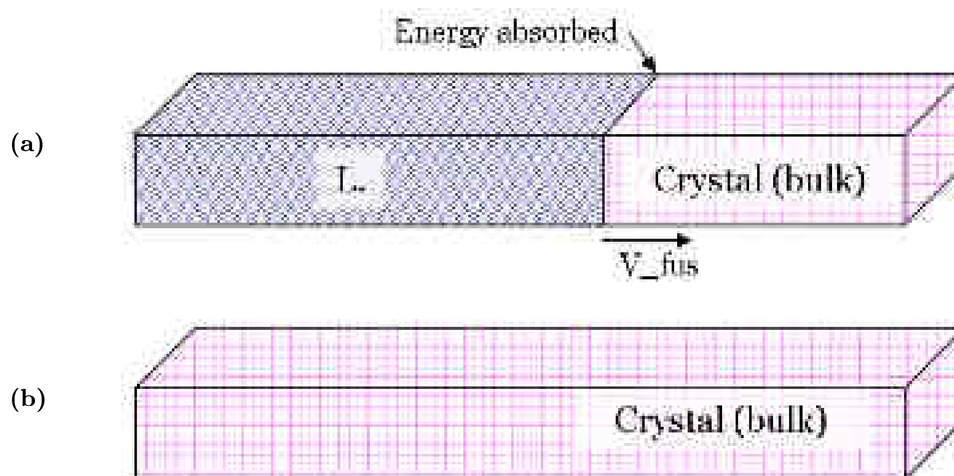

Figure 4.3: *System evolution after E.C, when the fusion front goes beyond the initial A/C interface, subfigure a, leaving a reconstructed crystal with no defects at the end of the process, subfigure b.*

4.3 A phase field model for the Explosive Crystallization

The quantitative modeling of the EC phenomenon should allow the computation of the contemporary kinetics of the crystal-liquid and liquid-amorphous front on the basis of the thermodynamic parameters of the substance in study. In the following we formalize a phase field EC model where the Phase Field variable ϕ assumes multiple values related to the three phases involved in the EC. We start from the derivation of Wheeler et al. [11, 25] already discussed in subsection 2.3.3 on page 36. This formulation is capable of describing the co-presence of two phases only in the system (e.g crystal/liquid or amorphous/liquid) using the positive sector of the phase values $\phi \geq 0$. The idea behind our extension to the three phase case is the use of both negative and positive sectors of the phase field whereas negative values rule the amorphous/liquid inter-phase while the crystal/liquid one is governed by positive values. In order to suitably modify the Phase Field equation we first change the expression for the potential energy density (eq. 2.42 on page 36) as it follows:

$$f(\phi) = -\phi^2 (1-\phi)^2 \rightarrow \widetilde{f}(\phi) = -\phi^2 (1-|\phi|)^2 \tag{4.1}$$

consistently the derivatives of the drift terms of the phase and temperature equations are replaced by:

$$\frac{\partial \widetilde{g}}{\partial \phi} = 8\phi^2 (1-|\phi|)^2 \tag{4.2}$$

and

$$\frac{1}{2}\frac{\partial \widetilde{h_2}(\phi)}{\partial t} = 30\phi^2 (1-|\phi|)^2 \frac{\partial \phi}{\partial t} \tag{4.3}$$

This formulation exploits three local minima of the potential energy density at $-1, 0, 1$ (see the red curve in the fig. 4.4 compared to the potential energy of the original two phase formalism shown as a blue line). One of these minima (the global minimum of $F(\phi, \lambda u)$) is related to the stable phase while the other two are related to the metastable ones, where the stability of one phase with respect to the others is ruled by the local temperature through the modified eq. 2.21 for the total free energy density.

The last part of the modelling extension is related to the modifications of the expressions for the thermodynamic parameters of the model which now implements a two sectors (negative and positive ϕ) dependence to consider properly the values for the amorphous/liquid and crystal/liquid case. Consequently the complete Phase Field for the EC reads:

$$\tau\frac{\partial \phi}{\partial t} = W^2\nabla^2\phi - \frac{\partial \widetilde{f}}{\partial \phi} - \lambda(\phi)\, u\frac{\partial \widetilde{g}}{\partial \phi} = W^2\nabla^2\phi - \\ - 2\phi(1-|\phi|)(1-2|\phi|) - 8\lambda u\phi^2 (1-|\phi|)^2 \tag{4.4}$$

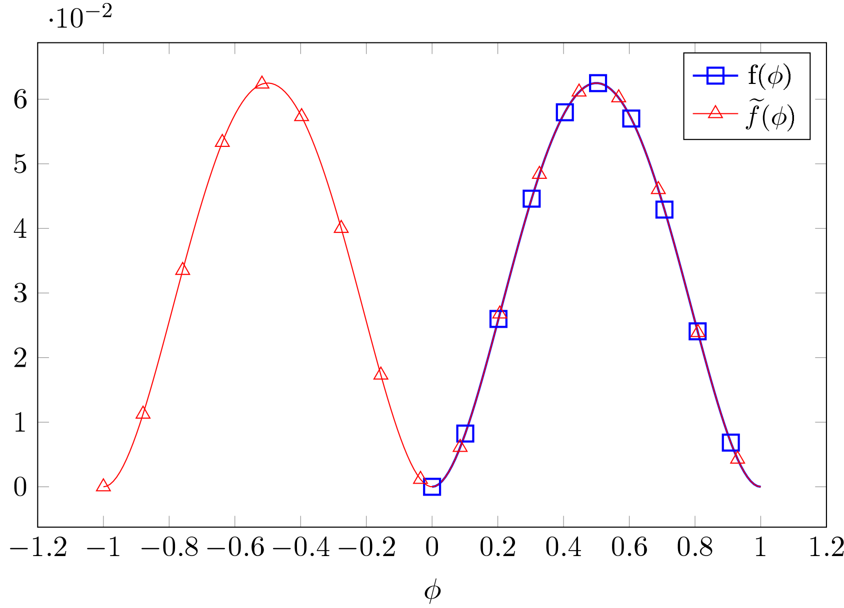

Figure 4.4: *Free energy function $f(\phi)$ of the Wheeler formulation with two minima (blue curve and squares) and the one used in our extension with three minima (red curve and triangles). In the region 0-1 the curves are identical.*

$$c_p \frac{\partial T}{\partial t} = \nabla \left[K(\phi, T) \nabla T \right] + 30 L(\phi) \phi^2 (1 - |\phi|)^2 \frac{\partial \phi}{\partial t} + S \tag{4.5}$$

where S is the heat source which has to be self-consistently evaluated by coupling the Maxwell equation with the model while the expressions for the coupling parameter, latent heat, melting temperature, specific heat, thermal conductivity are respectively:

$$\lambda(\phi) = \theta(\phi) \lambda_c(T) + [1 - \theta(\phi)] \lambda_a(T) \tag{4.6}$$

$$L(\phi) = \theta(\phi) L_c - [1 - \theta(\phi)] L_a \tag{4.7}$$

$$T_M(\phi) = \theta(\phi) T_{Mc} + [1 - \theta(\phi)] T_{Ma} \tag{4.8}$$

$$C_p(\phi, T) = \theta(\phi) C_{pc}(T) + [1 - \theta(\phi)] C_{pa}(T) + C_{pl}(T) [1 - |\phi|] \tag{4.9}$$

$$K(\phi, T) = \theta(\phi) K_c(T) + [1 - \theta(\phi)] K_a(T) + K_l(T) [1 - |\phi|] \tag{4.10}$$

where $\theta(\phi)$ is the Heaviside step function while the c, a, l subscripts indicate crystal, amorphous and liquid phases respectively. Note that the minus sign in the latent heat expression eq. 4.7 is related to the opposite time derivative of the phase in the amorphous to liquid and crystal to liquid phase transitions.

4.3.1 Dopant/Impurity field

Comparisons between experimental and simulated dopant profiles is a reliable method for the model validation. In particular, implanted impurities redistribute due to the high diffusivity in the liquid state and are trapped in the solid phase by the rapid re-growth [37]. As a consequence, in order to accurately simulate impurity redistribution during EC we have coupled this multi-phase field model with the two components diffusion model of ref. [14], already discussed in section 2.4 on page 37. The total diffusivity function is temperature and phase dependent through the followings equations

$$D^{LD}(\phi, T) = \theta(\phi) D_c(T) + [1 - \theta(\phi)] D_a(T) + D_l^{LD}(T) [1 - |\phi|] \quad (4.11)$$

$$D^{HD}(\phi, T) = \theta(\phi) D_c(T) + [1 - \theta(\phi)] D_a(T) + D_l^{HD}(T) [1 - |\phi|] \quad (4.12)$$

where D_l^{HD} and D_l^{LD} are the impurity diffusivity in the higher and lower diffusivity state in liquid phase. $\bar{R}(T)$ is the average (equilibrium) ratio between low and high diffusivity states at constant T.

In the solid phase metallic bonds are not present and $D_{sol} = D_{sol}^{HD} = D_{sol}^{LD}$; We assume that the diffusivity in the solid phase D_{sol} is the same for the crystal and amorphous case [31].

Out-diffusion from the surface to the air could also occur with some relevance during the interval dominated by the liquid phase. In our model out-diffusion is governed by the following equation for the boundary condition at the surface position

$$\left.\frac{\partial C}{\partial x}\right|_0 = k \cdot C \quad (4.13)$$

In Appendix A on page 139 we report the parameters used in the simulation. We note that some parameters depend on T and they all are phase dependent.

4.4 Experimentals

In order to properly present the model results by means of a real application case, we apply the formalism to the study of LA processes in implanted amorphous Ge (α-Ge) on crystalline Ge (c-Ge). The experimental procedure begins with a standard cleaning on high resistivity (0.059-0.088 $\Omega\cdot$ cm)

p-type Ge wafers (100), then continues with an Phosporous (P) implantation process at the energy of 15 keV up to the dose of 1×10^{15} cm^{-2}. The implantation creates an amorphous layer, about 30-35 nm thick, as shown by the Transmission Electron Microscopy (TEM) analysis in section view in fig. 4.5. We note that an amorphous film with a non perfectly flat amorphous/crystal (A/C) interface is visible as different contrast with respect to the underlying crystal substrate.

After the implantation, a single pulse Laser Thermal Annealing is performed. The fluences considered for the process are 0.55, 0.8 and 1.2 J/cm^2. We note that, as we will discuss in the following, the 0.55 J/cm^2 case is the threshold energy for the melting of the α-Ge. The coverage area of the laser spot is $\sim 1 \times 1$ cm^2 over $\sim$ 160 ns of exposure time of the samples to the laser pulse.

In situ time-resolved reflectivity (TRR) analysis, using a laser probe at a wavelength λ_{probe} =635 nm, has been applied to analyse the surface optical response during the laser irradiation. After all the LA processes, the samples have been investigated by Scanning Electron Microscopy (SEM) to control for the surface quality. SEM analysis (not shown) does not reveal any particular surface features like wrinkles or ripples. TEM has been applied to control the quality of the crystal before and after the LA. Secondary Ion Mass Spectrometry (SIMS) measurements of P chemical profiles before and after LA have been performed using a Cameca IMS-4f instrument with a Cs+ 5.5 keV primary beam.

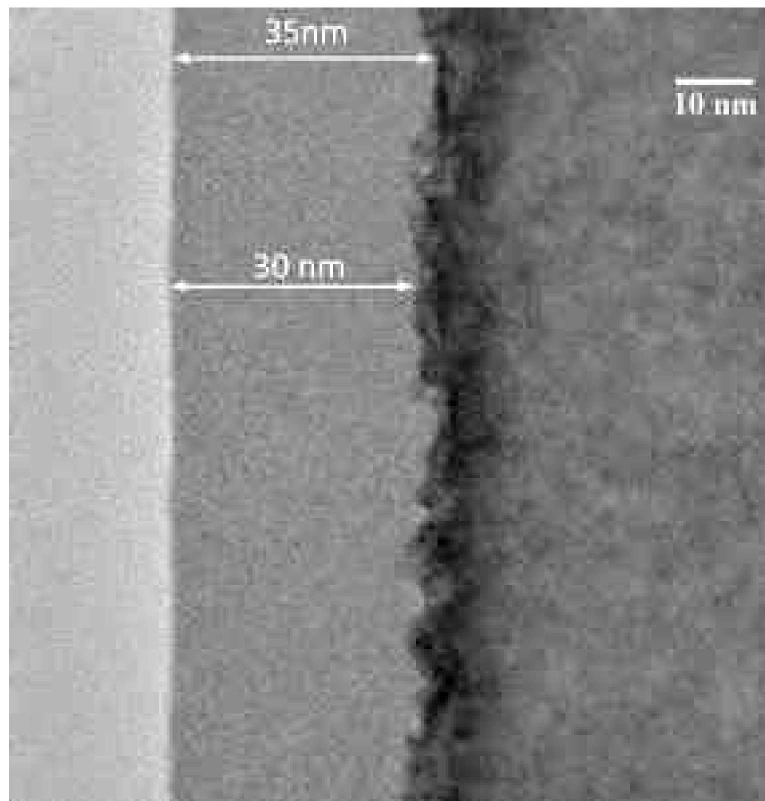

Figure 4.5: *TEM image of the sample before laser process. The amorphous layer ranges between 30-35 nm.*

4.5 Three phase simulations

In this section we discuss in the detail one dimensional (1D) simulations of the experimental processes presented in the previous section. The simulation represents a 1D line section of the sample with the surface on the left. The initial phase variable (see fig. 4.6) matches the TEM section of as implanted sample in fig. 4.5: The top layer of 35 nm is in the amorphous phase, with value $\phi = -1$ of the phase variable in our method, upon a crystalline bulk up to 50 μm (the substrate thickness) with a value of 1 of ϕ. We note that we have initialized the thickness of the amorphous film at the maximum value visible from the contrast in fig. 4.5, i.e. we assume that the crystal phase is positioned below the strongly damaged zone evidenced by TEM. The inset in fig. 4.6 represents the laser power pulse used in all the simulations. The initial temperature of the sample is set at the value of 300 K in the whole simulation box. The as-implanted P SIMS profile is also shown in fig. 4.6 and it is used for the initialization of the impurity density field in the LA simulations.

From fig. 4.7 to fig. 4.10 we plot, in the same figure for different times, snapshots of phase, temperature and dopant fields obtained in the simulation of LA at a fluence of 1.2 J/cm^2 (similar conventions are used in these figures for indicating field types and values). The nucleation radius r_n of the (poly)crystal phase nucleating in the undercooled liquid Ge is assumed as $r_n = 5$ nm for the three cases. Figure 4.7 shows the simulation results after t= 155 ns before the occurrence of the EC nucleation event. We can observe the simulated evolution at this time reflects the situation showed in fig. 4.1b (i.e. the initial melting of the amorphous film): There is the liquid phase on the left side ($\phi = 0$), the amorphous one in the middle ($\phi = -1$) and the crystalline in the bulk ($\phi = 1$). The temperature exhibits the typical diffuse decay in the bulk and a plateau (at temperatures slightly larger than the melting point of α-Ge) close to the surface due to both the latent heat absorption and the presence of the liquid phase with its hight thermal conductivity.

In fig. 4.8 we show a snapshot corresponding to the situation of fig. 4.1c. From left to right the black curve (the phase) starts with value 1, i.e. the crystal phase, then it drops to the 0 value that is the cushion of liquid phase (this layer is about 15 nm thick) and after the liquid layer the value -1 is reached for the remaining part of the amorphous phase. The last part of the phase function is the original crystalline bulk ($\phi = 1$). We note that the real morphology of the crystal arising from the primary EC event is of poly-crystalline type. However, the current model setting does not distinguish the crystal from the poly-crystal: they share the same thermodynamic parameters and phase ($\phi = 1$) values. The red curve represents the temperature of the specimen in this stage and it shows (from left to right): a significant higher value with respect to the melting point of α-Ge due to the solidifi-

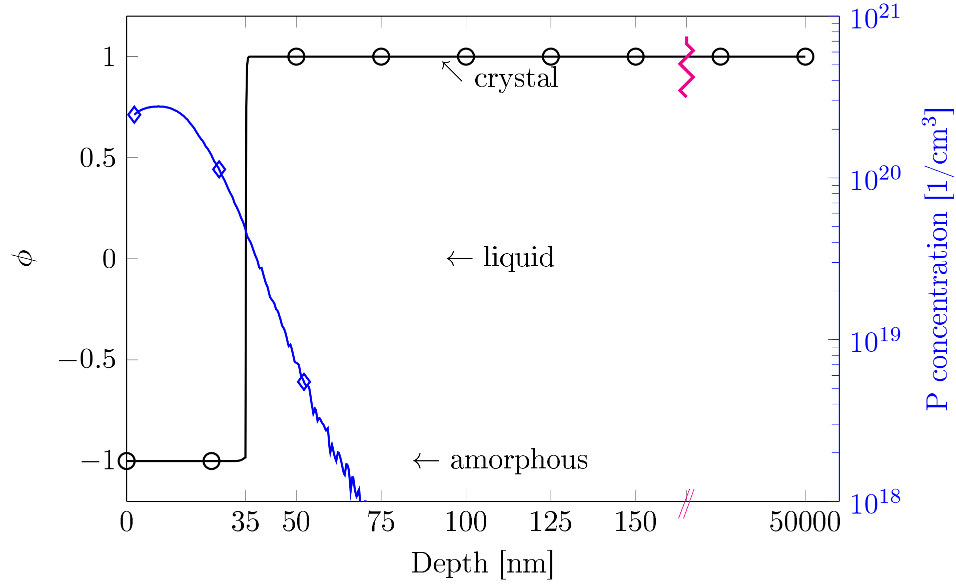

Figure 4.6: *Simulation $t = 0ns$. The black curve with circle indicates the initial phase field with the value $\phi = -1$ that represents the amorphous layer while the value $\phi = 1$ is the crystalline phase. The amorphous layer is 35 nm. The blue curve with rhombus is the as-implanted phosphorous concentration.*

cation on the surface (i.e. the heat is released); a descending value in the liquid layer; a lower value close to the liquid amorphous/interface (where heat is absorbed) and beyond the amorphous/crystal interface due to the typical diffusion decay. The primary front activated by the EC consumes the amorphous (see fig. 4.2a) film which is replaced by a nano-crystalline one at the end of the three phases EC phenomenon after a very short time interval ($EC_{time} \sim 1$ ns).

If fluency is sufficient to reach the crystalline melting temperature it is possible to create a second melting front, see fig. 4.2a. No simulation snapshots are here reported.

The condition of the schematic at fig. 4.3a is reproduced by the simulated evolution at t=210 nm (see fig. 4.9). A secondary (two phases) front starts to evolve as soon as the (poly)crystal surface reaches the c-Ge melting point and for these irradiation conditions it reaches a melt depth beyond the original A/C interface.

Figure 4.10 shows the simulation at t=500 ns when the evolution of the phase and dopant fields is practically quenched. Here the sample is fully crystalline ($\phi = 1$), see fig. 4.2b and fig. 4.3b (poly-crystalline and crystalline are equivalent in the method). The temperature, the red curve in the figure, shows a rather uniform value in the region of interest and it continues to decrease with time recovering the 300 K value after few tens of μs.

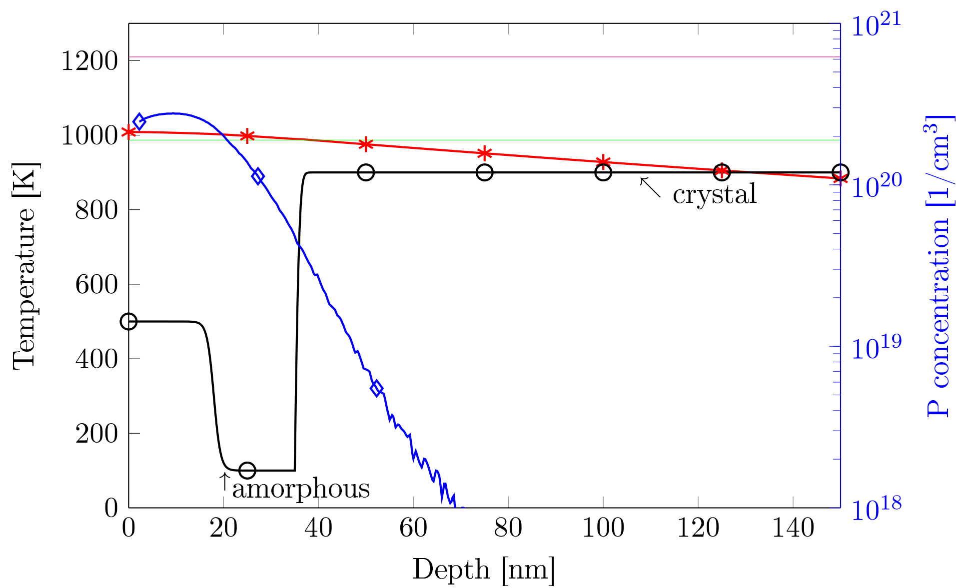

Figure 4.7: *Snapshot of the simulation at t=155ns (before the EC event) for a LA process at 1.2 J/cm^2. The scale on the left is for the temperature values (red solid line and asterisk), the one on the right for the dopant density (blue solid line and rhombus) and a text description is reported for the phase (black solid line), representing the 3 main values of the ϕ function: -1, 0 and +1 corresponding to to the amorphous, liquid and crystalline phases respectively. The melting temperature of the amorphous (green line) and of the crystal phase (magenta line) are also indicated.*

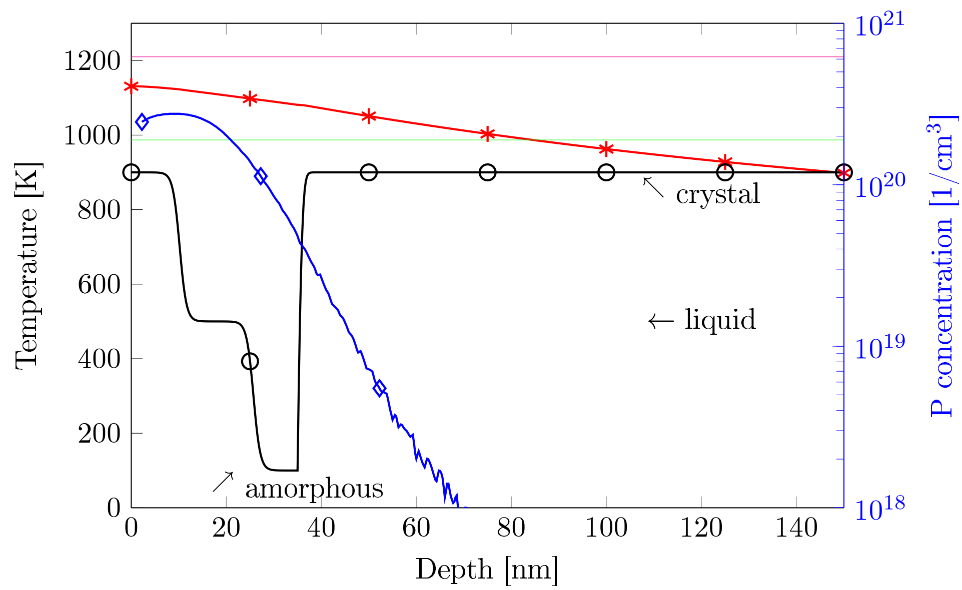

Figure 4.8: *Snapshot of the simulation at t=156ns (EC event) for a LA process at 1.2 J/cm^2. The scale on the left is for the temperature values (red solid line and asterisk), the one on the right for the dopant density (blue solid line and rhombus) and a text description is reported for the phase (black solid line), representing the 3 main values of the ϕ function: -1, 0 and +1 corresponding to to the amorphous, liquid and crystalline phases respectively. The melting temperature of the amorphous (green line) and of the crystal phase (magenta line) are also indicated.*

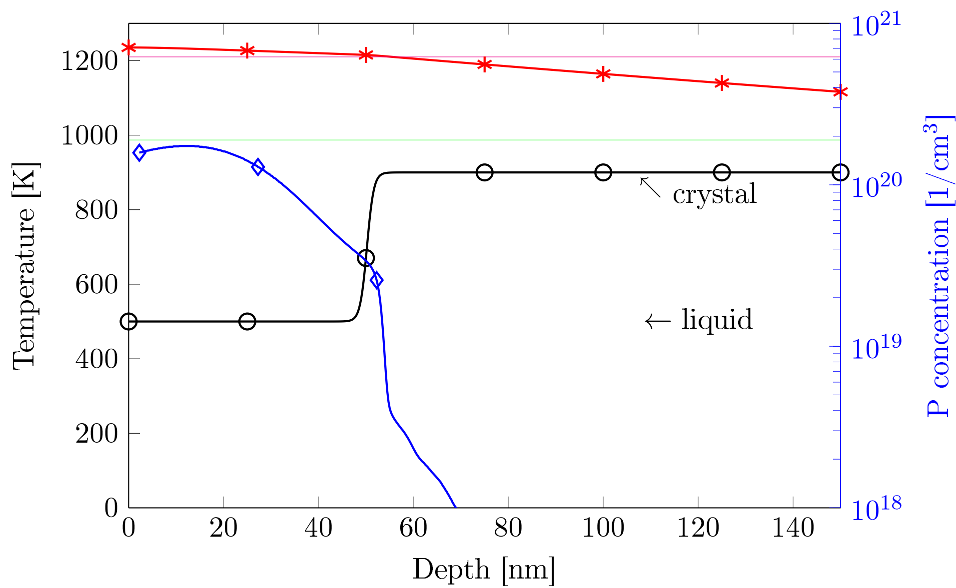

Figure 4.9: *Snapshot of the simulation at t=210ns (secondary melting) for a LA process at 1.2 J/cm^2. The scale on the left is for the temperature values (red solid line and asterisk), the one on the right for the dopant density (blue solid line and rhombus) and a text description is reported for the phase (black solid line), representing the 3 main values of the ϕ function: -1, 0 and +1 corresponding to to the amorphous, liquid and crystalline phases respectively. The melting temperature of the amorphous (green line) and of the crystal phase (magenta line) are also indicated.*

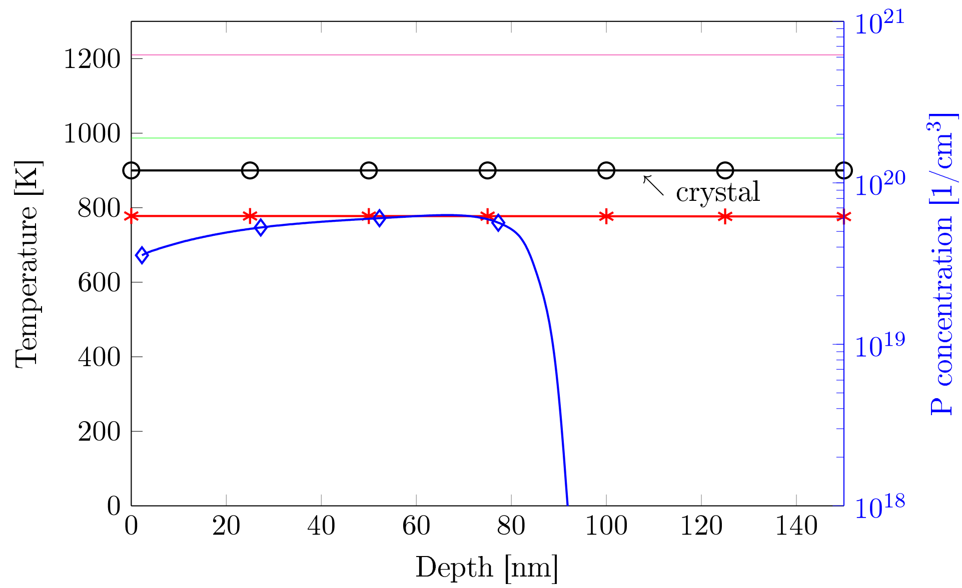

Figure 4.10: *Snapshot of the simulation at t=500ns (final state) for a LA process at 1.2 J/cm^2. The scale on the left is for the temperature values (red solid line and asterisk), the one on the right for the dopant density (blue solid line and rhombus) and a text description is reported for the phase (black solid line), representing the 3 main values of the ϕ function: -1, 0 and +1 corresponding to to the amorphous, liquid and crystalline phases respectively. The melting temperature of the amorphous (green line) and of the crystal phase (magenta line) are also indicated.*

We underline that key-features shown by the larger fluence case are also present in the other cases, which are not presented here for brevity. Of course, the secondary front evolves only if the laser energy density is large enough to heat the surface at the c-Ge melting point. Otherwise only EC is activated as it can be inferred by fig. 4.11 which shows the temperature at the surface as a function of the simulated time for the 0.55, 0.8 and 1.2 J/cm^2 case in red, green and blue, respectively. Two guideline are also present in the plot that indicate the melting temperature of the α-Ge and c-Ge, magenta with crosses and cyan with vertical lines, respectively. The curves share the same left part, where there is the heating (with a slope depending on the laser fluence) and the plateau due to amorphous melting. After the nucleation time in all the cases the EC occurs with the typical signature of its spike of heating due to its extremely fast kinetics. For the lower fluence case (0.55 J/cm^2 after the explosive there is only a redistribution of the heating and then the cooling. In the 0.8 and 1.2 J/cm^2 cases after the EC the temperature continues to rise due to the higher fluence, and there is the creation of a secondary melting. In these cases another melting condition happens at the c-Ge melting point because now the surface layer has crystalline characteristics. For the 1.2 J/cm^2 case the temperature increases at the surface in secondary melting and the liquid state is more pronounced whilst for the 0.8 J/cm^2 case T stays close to the T_M(c-Ge)=1210 K value. After the melting there is the cooling of the sample, like in the previous case. The maximum melt depth of the secondary melt front is 15 and 84 nm for the 0.8 and 1.2 J/cm^2 case respectively, i.e. in the first case this value is lower than the original α-Ge/c-Ge interface see figs. 4.2a and 4.3a. We underline that the duration of the plateau during the melting of the amorphous is different in the 3 cases, in particular it is smaller for higher fluence. This difference is due to the different nucleation time that depends essentially on the temperature. Higher (lower) temperature, resulting from higher (lower) fluence, leads to a smaller (larger) nucleation time.

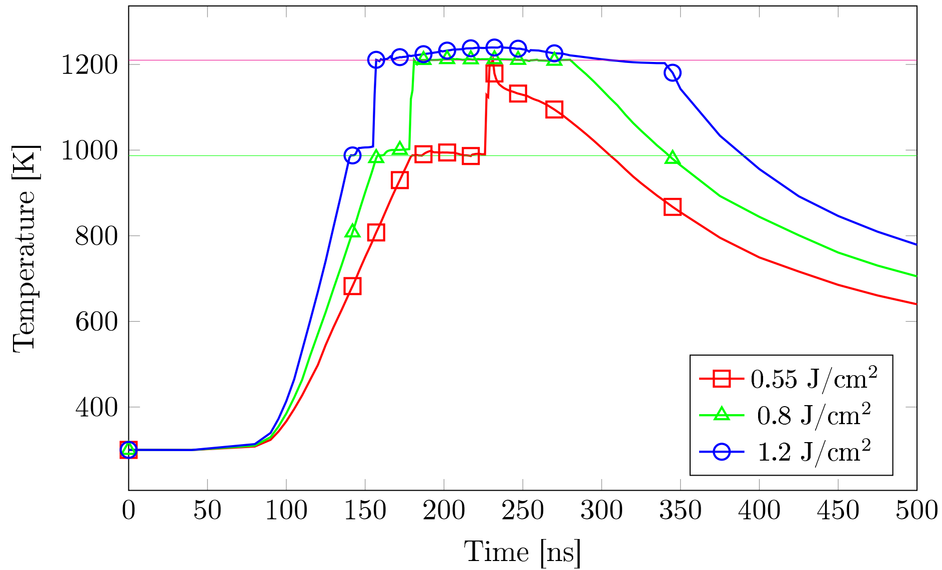

Figure 4.11: *Temperature at the surface for 0.55 (red line and squares), 0.8 (green line and triangles), 1.2 (blue line and circles) J/cm^2 case. Heating, fusion and EC are present in all curves, secondary melting in the 0.8 and 1.2 J/cm^2 cases only. The horizontal lines represent the melting temperature of the amorphous phase (in green) and of the crystal one (in magenta).*

4.6 Model Validation

In order to demonstrate the reliability of the multi-phases field EC model we will discuss in this section the comparisons between the simulation predictions and the in-situ and ex-situ experimental analyses of processed samples.

4.6.1 In-situ transient reflectivity and Micro-structural analysis

In fig. 4.12 we compare our simulation with in situ-reflectivity and TEM for the three fluences (upper panel 0.55 J/cm^2, middle panel 0.8 J/cm^2, lower panel 1.2 J/cm^2). The reflectivity is measured with a laser probe with a wavelength of 635 nm. As a consequence we have calculated the (multi layer) system reflectivity at this wavelength using the time dependent phase function in order to distinguish the amorphous, liquid and crystal layers' thicknesses. In the graphs we plot the measured reflectivity (blue line), the calculated reflectivity (red line) whilst on the right axes the relative values of reflectivity of amorphous, crystal and liquid Ge at 635 nm are also reported. We note that the experimental instrumentation can measure only the relative value of the reflectivity. As a consequence, the left scale is in arbitrary units. Moreover, the probe spot is non fully aligned and focused to the region heated by the main laser, so the measured value is an average of

the reflectivity on a probe surface area (mm scale diameter) and not a point wise value. As a consequence, we also expect some case to case variance of the reflectivity modulation if all the probed surface region does not undergo instantly to the phase transitions. In the case of figs. 4.12a-4.12b (0.55 J/cm^2) the simulation predicts a pure EC event and, indeed, reflectivity and TEM measurements clearly indicate that this is the case. Both simulation and measurements show a single asymmetric peak of the reflectivity due to the α-Ge melting (smooth increase) and ultra fast EC (sharp decrease) while the difference between the left and right plateau are related to the two different reflectivity values of the initial (α-Ge) and final (c-Ge) phases. In this and in the other cases the shape of simulated and measured reflectivity peak is different. However, these differences can be understood in terms of the lateral propagation of the phase transition phenomena in the surface probed by the 635 nm laser. Indeed, while the 1D simulation assumes a single global transition event and that the propagation of the conventional melting and EC phenomena occurs only in depth, in real samples an additional concentric propagation of the front seen by the probe at the surface should occur (also due to point to point variation of the surface temperature). This lateral propagation could explain the delays observed in the experimental peaks in all the cases considered. Figure 4.12b shows the TEM image of the specimen at the end of the 0.55 J/cm^2 process: A polycrystalline layer with very small grains and a rather smooth surface replaces the original amorphous one as we expect for a pure primary EC event.

In figs. 4.12c-4.12d the experimental analysis refers to the case where a secondary melting front starts but it does not reach the original a/c interface. Again the comparisons are fully consistent. The experimental and simulated reflectivity show a double feature related to the primary and secondary melting and the agreement is good in consideration of the delayed increase and decrease of the experimental curve already discussed. The TEM image at fig. 4.12d shows a polycrystalline layer with large and inhomogeneous grains and a rough surface as we could expect from a secondary slower melting of a nano-crystalline film which does not reach the ordered crystal surface of the substrate.

Figures 4.12e-4.12f report the case with the higher value of fluence and we observe a spike related to the EC and a subsequent longer ($\sim$ 180 ns) secondary melting phenomenon. In this case the simulation predicts that the melt depth is behind the initial amorphous/crystalline interface. As a consequence, we could expect an epitaxial regrowth after the secondary melting. Indeed, the agreement is good also in this case since the TEM image shows a total defect free crystal regrowth and an extremely flat surface. In all the cases at the end of the LA the sample shows always a crystalline (epitaxial or polycrystalline) structure everywhere and this is again in agreement with our simulations.

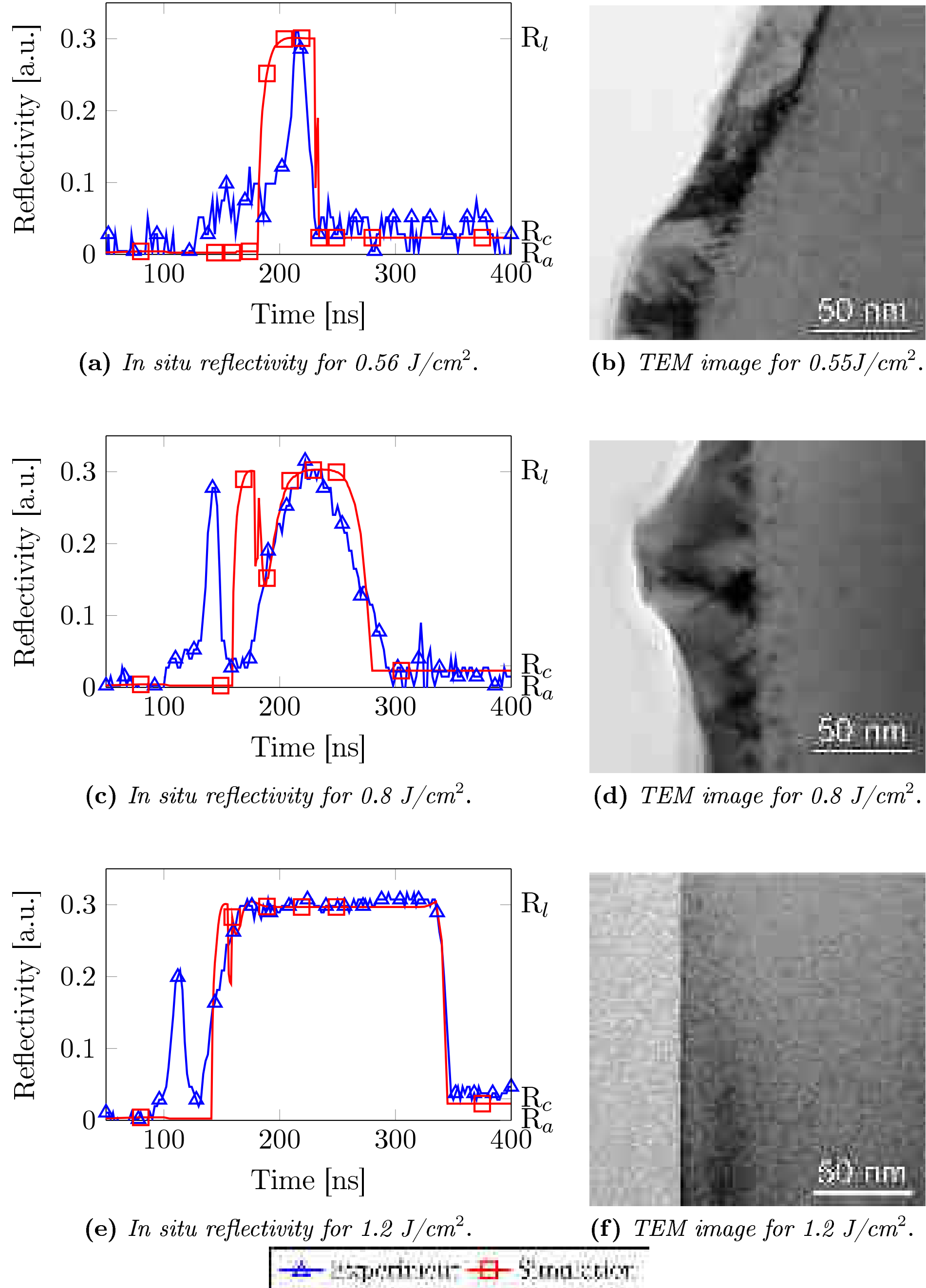

(a) *In situ reflectivity for 0.56 J/cm^2.*

(b) *TEM image for 0.55J/cm^2.*

(c) *In situ reflectivity for 0.8 J/cm^2.*

(d) *TEM image for 0.8 J/cm^2.*

(e) *In situ reflectivity for 1.2 J/cm^2.*

(f) *TEM image for 1.2 J/cm^2.*

Figure 4.12: *Comparison between in situ reflectivity and simulation on the left and the corresponding TEM images on the right. From the top to the bottom 0.55, 0.8 and 1.2 J/cm^2 case are shown respectively.*

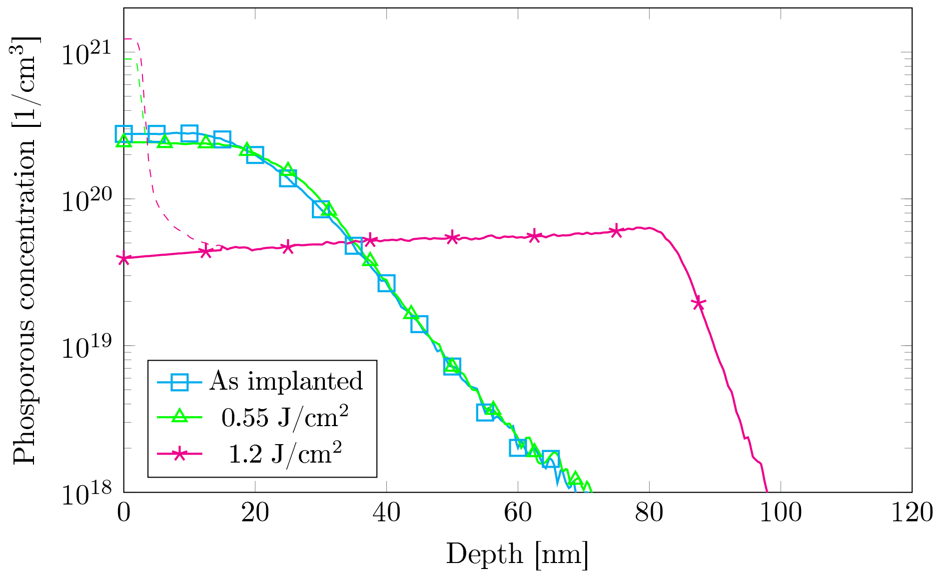

Figure 4.13: *Second ion mass spectroscopy measurement on Germanium doped with Phosphorus. The as implanted profile is plotted as cyan line and squares, the profile processed with pulse at 0.55 J/cm^2 as green line and triangle, the one processed with pulse at 1.2 J/cm^2 as magenta line and stars. The as implanted and the 0.55 J/cm^2 are very close.*

4.6.2 Chemical analysis

Here we discuss by comparison with EC model predictions the phosphorus redistribution in germanium due to the process and the experimental analysis presented in section 4.4. We use the P/Ge calibration of the two species diffusion model of Ref. [19] reported in the Appendix A on page 139.

In fig. 4.13 the P profile of the implanted sample (cyan and squares) and that obtained for the lower (green with stars) and higher fluences (magenta with triangles) cases (0.55 and 1.22 J/cm^2) are shown. The diffused profile obtained for the 1.22 J/cm^2 (case) shows an *against gradient* behavior close to the maximum melt depth position which justifies the use of the two species model specifically suited to predict anomalous redistribution of impurities during LA. Figure 4.14 shows the comparison between experimental and simulated profiles for the 0.55 J/cm^2 case. The plotted curves are the as implanted profile (cyan and squares), the experimental diffuse profile at end of the process (green line and stars) and the simulated diffuse profile (blue line and rhombus). In this case, as we have already discussed, only a primary EC occurs and the dopant profile beyond the initial amorphous/crystalline interface is unchanged, since the movement of liquid layer driving the EC stops at this boundary. A limited but detectable diffusion can be observed caused by the ultrafast sweeping of the liquid layer during the EC and this

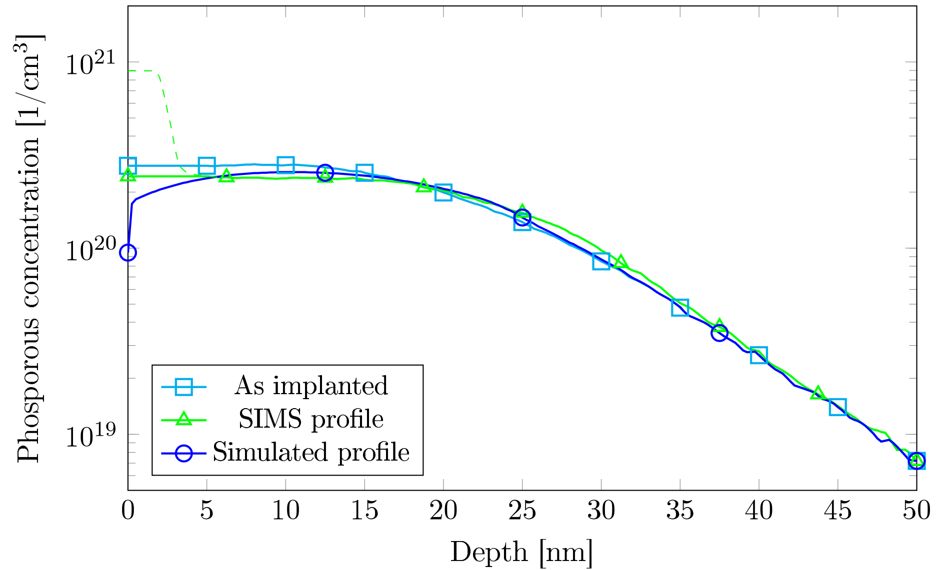

Figure 4.14: *Comparison between SIMS and simulation for the 0.55 J/cm^2 case. Cyan and squares is the as implanted profile, green with triangles is the SIMS, solid blue and rhombus is the simulated concentration.*

impurity diffusion is also predicted by the simulation. The agreement between the simulated and SIMS profiles is good except in the surface region (about ~ 5 nm from the air/sample boundary) where SIMS measurement looses reliability. Figure 4.15 shows a similar analysis for the higher fluence case with in cyan and squares the as implanted profile, in magenta and triangles the experimental diffuse profile at end of the process, and in blue with rhombus the simulated diffuse profile. In this case secondary melting occurs at a melt depth well beyond the original A/C interface. Both SIMS resolution near surface and surface roughness may compromise the comparison with simulation results.

The combination of our model for EC and the two-state model for the impurity diffusion permits to obtain a good agreement between the simulated and experimental curves. Also for the intermediate case the model is able to predict the distribution of the dopant (not showed). Anyway the limited SIMS resolution makes the comparison between measured and simulated profile unfeasible.

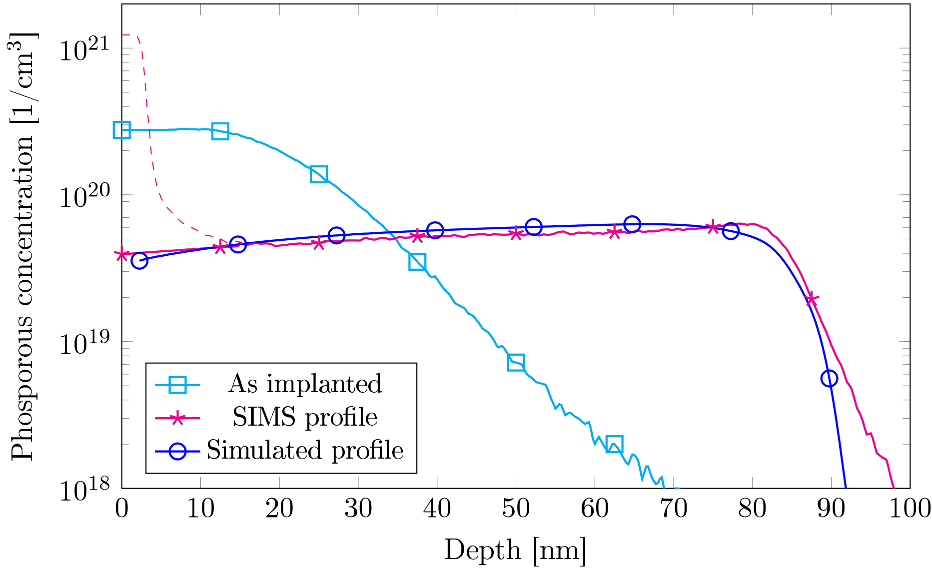

Figure 4.15: *Comparison between SIMS and simulation for the 1.2 J/cm^2 case. Cyan with squares is the as implanted profile, magenta with stars is the SIMS measurement, solid blue and rhombus is the simulated dopant curve.*

4.7 Advanced modeling for LA simulation of alloys

The presence of an alloy can be modeled introducing a new "natural" variable that represents the fraction of one dissolved material in another X_a. If we consider, for example, the silicon germanium in the composition $Si_{0.7}Ge_{0.3}$, i.e. in a Si-rich configuration, the alloy fraction, considering germanium as the second material, is 0.3. Obviously the sum of the components can not be greater than the unit, and the extremes, 0 and 1, represent the phases as well, in this case of silicon or germanium. The fraction of the alloy influences all thermodynamic parameters of the system that now depend on X_a. Without loss of generality, in this chapter we assume that they can be obtained in a first approximation as a linear interpolation of the temperature functions knows for the pure element. As a consequence, the equations of subsection 2.3.2 at page 2.33 are modified in the model of the alloy as :

$$\begin{aligned}\rho\left(\phi,T,X_a\right) = {} & X_1\left[\theta\left(\phi\right)\rho_{sol}\left(T\right)+\theta\left(-\phi\right)\rho_{liq}\left(T\right)\right] \\ & +\left(1-X_a\right)\left[\theta\left(\phi\right)\rho_{sol}\left(T\right)+\theta\left(-\phi\right)\rho_{liq}\left(T\right)\right]\end{aligned} \tag{4.14}$$

$$\begin{aligned}C_p\left(\phi,T,X_a\right) = {} & X_a\left[\theta\left(\phi\right)C_{psol}\left(T\right)+\theta\left(-\phi\right)C_{pliq}\left(T\right)\right] \\ & +\left(1-X_a\right)\left[\theta\left(\phi\right)C_{psol}\left(T\right)+\theta\left(-\phi\right)C_{pliq}\left(T\right)\right]\end{aligned} \tag{4.15}$$

$$\begin{aligned}K\left(\phi,T,X_a\right) = {} & X_a\left[\theta\left(\phi\right)K_{sol}\left(T\right)+\theta\left(-\phi\right)K_{liq}\left(T\right)\right] \\ & +\left(1-X_a\right)\left[\theta\left(\phi\right)K_{sol}\left(T\right)+\theta\left(-\phi\right)K_{liq}\left(T\right)\right]\end{aligned} \tag{4.16}$$

Of course any other dependence can be in principle used although a general functional dependence is difficult to achieve due to the limitations of experimental data for sufficient values of X_a and T. We underline that also latent heat and melting temperature also depend on the fraction of the alloy.

$$L(\phi, X_a) = X_a [\theta(\phi) L_c - [1 - \theta(\phi)] L_a] + (1 - X_a) [\theta(\phi) L_c - [1 - \theta(\phi)]] \tag{4.17}$$

$$\begin{aligned} T_M(\phi, X_a) = X_a [\theta(\phi) T_{Mc} + [1 - \theta(\phi)] T_{Ma}] \\ + (1 - X_a) [\theta(\phi) T_{Mc} + [1 - \theta(\phi)] T_{Ma}] \end{aligned} \tag{4.18}$$

This dependence is the difficult part of the numerical approach to the alloy problem since the local alloy fraction changes with continuity at the melting front influencing the latent heat release. This strong nonlinearity could create great problems to the stability of the solution. However, front tracking methods allow for suitable schemes of integrating the X_a dependence naturally, thus minimizing these issues.

The evolutionary model for calculating the alloy concentration evolution is similar to that used by the dopant and is a typical diffusive model that follows Fick's law.

$$\frac{dX_a}{dt} = -\nabla (D_a(\phi, T) \nabla X_a) \tag{4.19}$$

where X_a is the alloy fraction, D_a is the diffusion coefficient, that in principle could depend from the phase and temperature. For X_a in LIAB we have also implemented the model for the anomalous segregation presented in the subsection section 2.4 However, due to the lack of data for the calibration for all the cases here discussed we apply the simple diffusive model. The allocation of the alloy is only significant in the liquid phase, so for non melting systems there are no significant changes with respect to the previous model.

The fraction of alloy evolves with the system so it is not a fixed value, and as we will see below, this often leads to a type of system that melts evolves and finally solidifies with features different from the initial one.

In this section we present some benchmark results in a 1D structure with 50 nm of $Si_{0.5}Ge_{0.5}$ on top of a silicon bulk deep 6 μm. The material parameters are reported in the the Appendix A.

In the figures from 4.16 to 4.19 we plot the temperature and the alloy fraction for different simulation times. In particular fig. 4.16 reports the snapshots at 50 ns. The temperature shows the usual decay and, since the system is all solid, the fraction alloy is unchanged.

At 100 ns, shown in fig. 4.17, the temperature is higher than the previous case, we have a liquid phase in the surface (the melting front is indicated by a vertical sign in the temperature curve) with a melt depth $\sim$ 31nm.

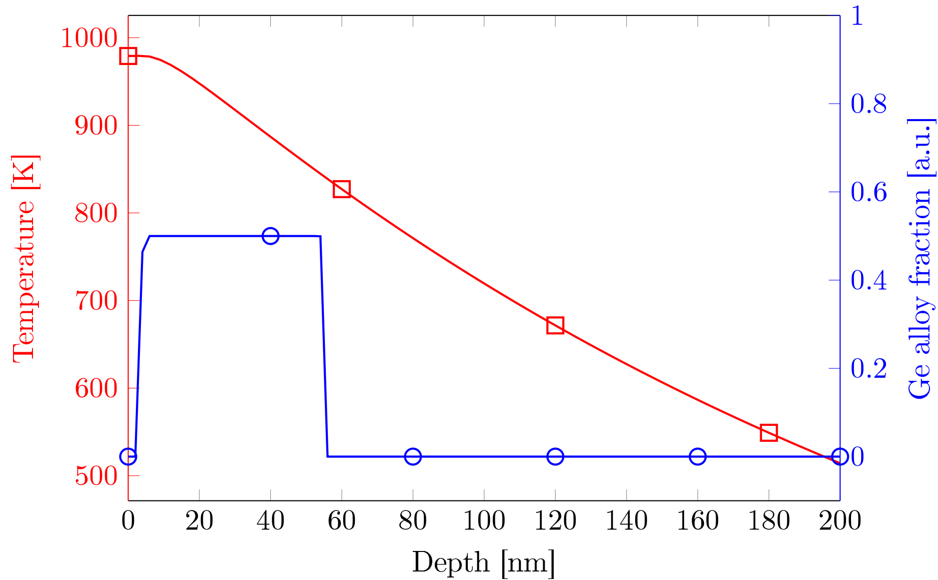

Figure 4.16: *Snapshot of the simulation for t=50 ns. Temperature (red line and squares) and Germanium alloy fraction (blue line and circles) are shown.*

The alloy fraction continues to be constant because the melting front is well inside the SiGe layer.

Figure 4.18 reports the system condition at 160ns. The temperature shows a little slope in the liquid zone, and the usual thermal decay in the solid phase (the melting depth corresponds again to the vertical sign on the temperature curve). The alloy fraction is now diffusing all over the liquid phase, and as a consequence the value is a bit lower with respect to that in the original SiGe layer. The alloy fraction diffuses in the liquid phase and acquire a lower value with respect to the 0.5, that represent the system prior to melting.

In the last figure, fig. 4.19, we can see the system at the end of the simulation, i.e. 500 ns. The temperature is roughly constant and the system is all solid. The alloy fraction is diffuses and acquire a lower value with respect to the 0.5 value, that represents the system prior to melting.

The alloy fraction has a sharp jump, as expected, in correspondence of the maximum melting depth due to the high diffusivity in the liquid phase and the low diffusivity in the solid phase.

In fig. 4.20 we plot the maximum temperature reached in the system and the corresponding melt depth for different laser fluences. The 0.9 J/cm^2case is a non melting case. Indeed the melt depth is zero, and the alloy composition remains unchanged during the process. The case 1.4 J/cm^2 shows melting only in the SiGe region. Indeed the temperature remains constant close to the melting temperature, and the corresponding melt depth remains

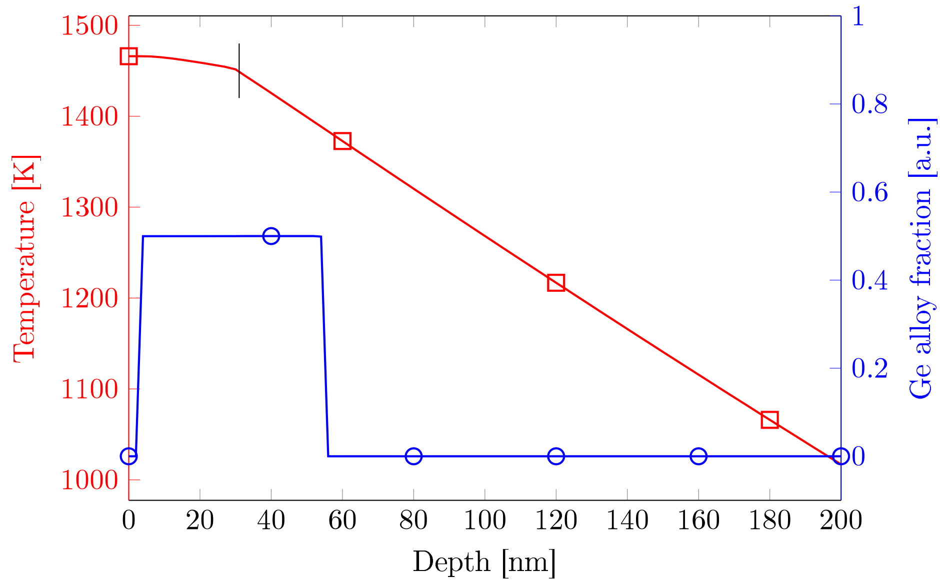

Figure 4.17: *Snapshot of the simulation for t=100 ns. Temperature (red line and squares) and Germanium alloy fraction (blue line and circles) are shown. A vertical black line over the temperature curve indicates the melt depth.*

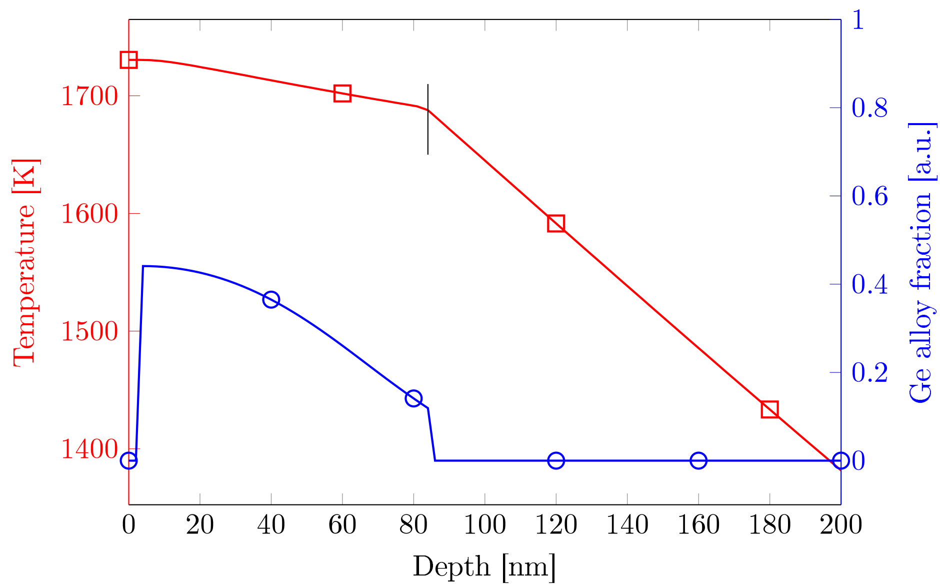

Figure 4.18: *Snapshot of the simulation for t=160 ns. Temperature (red line and squares) and Germanium alloy fraction (blue line and circles) are showed. A vertical black line over the temperature curve indicates the melt depth.*

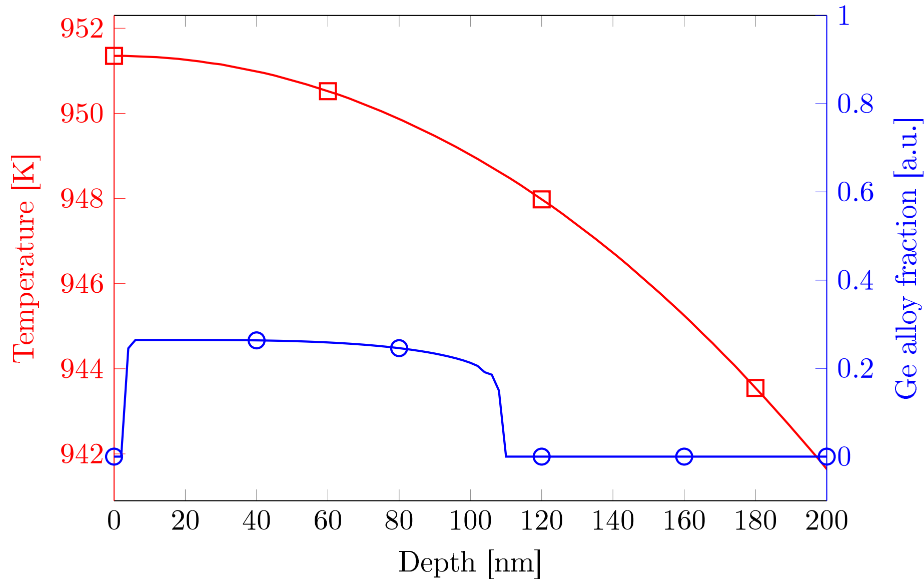

Figure 4.19: *Snapshot of the simulation for t=500 ns. Temperature (red line and squares) and Germanium alloy fraction (blue line and circles) are shown.*

lower than the brown horizontal line. The 1.6 J/cm^2 case shows initially the increase of the temperature, and then the melting of the SiGe layer in the 80-140 ns region. After that the temperature grows up and begins to melt the silicon layer (pure silicon has a higher temperature with respect to SiGe). Indeed, the melting area continues to increase till 200 ns. After that the temperature begins to decrease and there is the solidification of the alloy. In this scenario, the liquid alloy has a different composition than when it was melted, so now the melting front that goes from about 60 nm to the surface meets an alloy with a higher value of Si and, as a consequence, the solidification temperature is now higher than the melting one. Above 350 ns the system is all solid and it starts the thermal decay.

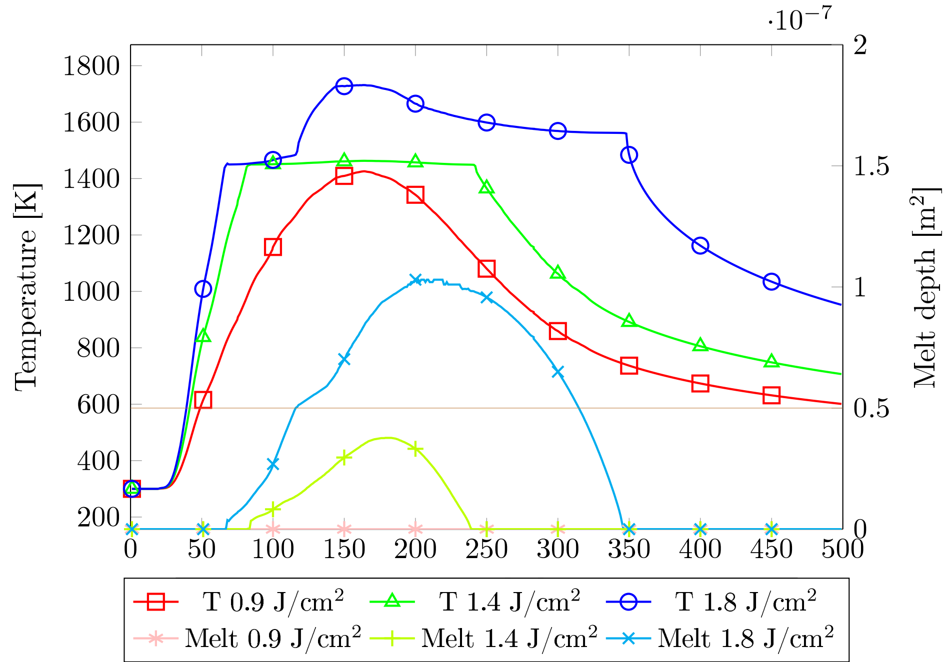

Figure 4.20: *Maximum temperature in the 1D alloyed system and total molten area as functions of the time for different laser energy densities.*

4.8 Conclusion

In this chapter we presented the two main advanced code features: An extended formulation of the phase field method applied to the problem of the explosive crystallization, and the model modification to consider a self-consistently alloy fraction reshaping. In both cases we obtained a rather robust, reliable and efficient method for the study of melting processes, without introducing additional ad-hoc variables. Our results have been compared with experiments in order to ensure an accurate calibration and verification of the numerical tool.

Even in this case, we found some difficulty in finding all the necessary parameters (optical parameters in the first place), and this is an issue for a self-consistent method due to the strong interaction and correlation between the laser heating and the structure local properties (geometry temperature, phase and dopant/alloy distribution).

Moreover, the future implementation of the formalism in numerical tools able to simulate two and three dimensional geometries will give the possibility to simulate the lateral propagation (especially for the EC phenomenon) extending the potential prediction power of the method. As a practical application of these advancements, in the next chapter we will discuss a TCAD study of a device structure presenting a SiGe region.

5

Advanced modeling of an industrial semiconductor element

5.1 Introduction

The semiconductor fabrication of modern chips traditionally includes three main stages: Front-End-Of-The-Line (FEOL), Middle-Of-The-Line, (MOL), and Back-End-Of-The-Line (BEOL). The typical FEOL processes include wafer preparation, isolation, well formation, gate patterning, spacer, extension and source/drain implantation, silicide formation, and dual stress liner formation. We have already discussed the possible application of the laser annealing as a FEOL process in the Chapter 3. The MOL process flow is applied mainly to the gate contact (CA) formation, which is an increasingly challenging part of the whole fabrication flow, particularly for lithography patterning. Successful fabrication and qualification of modern semiconductor chip products requires a deep understanding of the intricate interplay between materials and processes. A state-of-the-art technology unifies, in order to reduce size, the MOL with the BEOL, obtaining the (Middle End Of the Line) MEOL. Again LA could aid manufacturing, providing local heat sources also for the annealing of high level lines. The scope of this chapter is a TCAD analysis of LA, similar to that presented in Chapter 3, applied to the MEOL structures.

5.2 Simulation setting

The simulated structure is the two-dimensional geometry, shown in fig. 5.1, which as in the case of the FinFET is a reliable approximation of the whole

3D geometry of the Line due to the large width in the third dimension. The substrate is made of silicon up to 10 μm deep (not shown totally in the figure). Above the silicon bulk, there are two columns made of silicon, each of which supports a diamond-shaped structure made of $Si_{0.5}Ge_{0.5}$. Around these structures there are three columns of silicon dioxide with a height exceeding the diamonds-like one. Trenches in silicon dioxide are created to leave the higher portion of the diamonds exposed to the air. The simulation box is completed with a top layer of 200 nm of air above the maximum height of the silicon dioxide. From a thermal point of view we impose an initial uniform temperature in the whole system at $T_0 = 300$ K and a constant temperature in the lower boundary of the system fixed at 300 K. Moreover, we impose the symmetry (Neumann zero flux) condition on the left and right boundaries. This condition is consistent for simulating the surrounding channels, that are considered equal. No convective flow is considered in the air. The incident wave is coming from the top of the air and is directed along the y axis in a descending direction.

We start the simulation with a value of $\phi = 1$ in all the domains, which implies that the whole structure is in the solid phase. This choice improves the simulation stability, in a similar way as in the FinFET study (see discussion in section 3.2 on page 59).

In this case the materials that are supposed to melt are the SiGe diamonds and the silicon region below them. Specifically, the $Si_{0.5}Ge_{0.5}$ has an average melting temperature between Si and Ge so it is supposed to be the region where melting nucleation should take place.

We are interested in the study of :

1. the influence of the pitch (that means the distance between a repetitive structure with values of 35-55-75-100 nm);

2. the effect of various laser energies;

3. the effect of different laser polarizations.

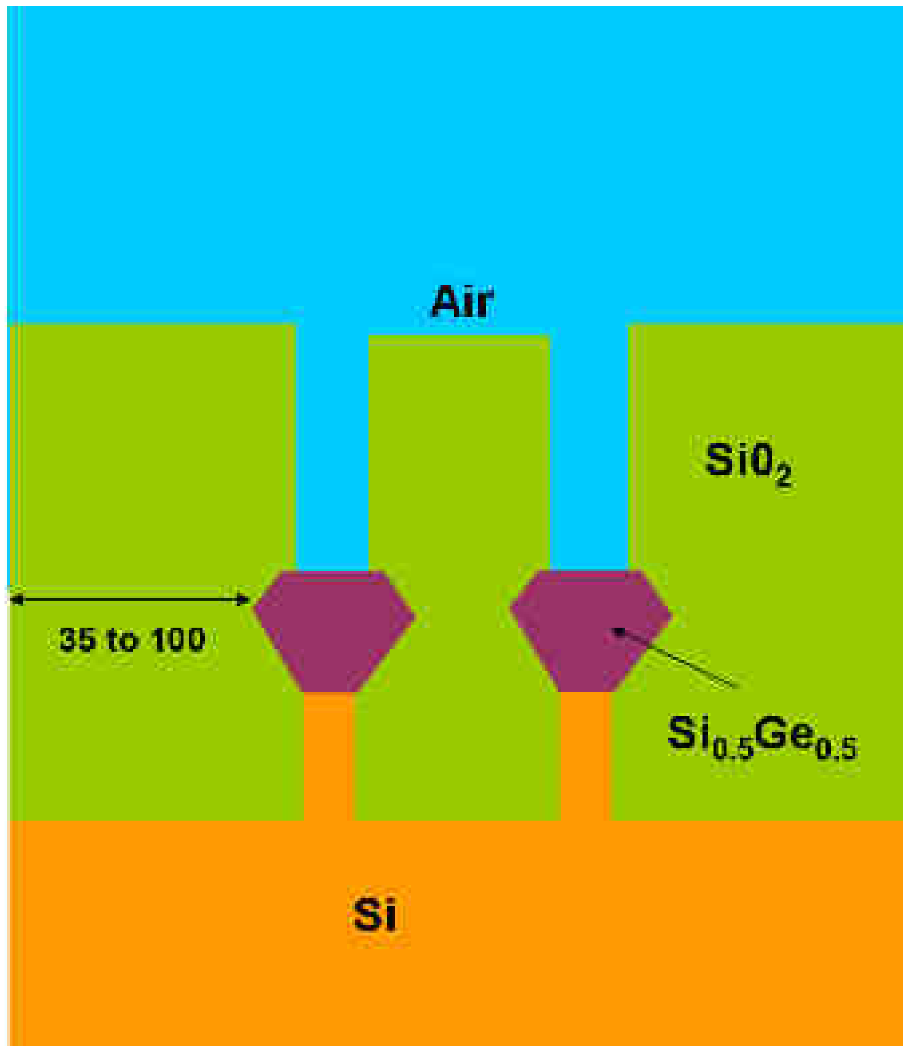

Figure 5.1: *MEOL structure made by two symmetric $Si_{0.5}Ge_{0.5}$ diamonds located upon two silicon columns on a silicon substrate. This structure is surrounded by silicon dioxide. The simulated system is completed with two channels of air above the diamonds and 200 nm of air on the top.*

5.3 Simulation results

From fig. 5.2 to fig. 5.7 we plot the global maximum temperature of the system for different laser polarization values.

For low laser fluence, like in fig. 5.2 where we plot the 35 nm case irradiated at 0.4 J/cm^2 energy density for different polarization values, we can see the usual heating shape. The left part shows that the temperature curves have similar initial trends for all the polarization values, then in the middle stage of the process there is a splitting. The 0° polarization value results in the "coldest" case, while the highest temperature is reached for 90° polarization angle. At this fluence, there is no melting for any polarization value. We have to consider that we have plotted the maximum temperature in the system and this is usually achieved in the diamond regions, although the thermal dissipation rule by the material's thermal properties could modify the "hottest" region especially in the quenching stage of the LA process.

Increasing the fluence, like in fig. 5.3 where the maximum temperature and melting area of a 35 nm geometry under 0.5 J/cm^2 irradiation is shown, we can see an overall increase of the temperature and a plateau typical of the melting scenario. In this case, with the 0° value there is the partial melting of the diamonds, in the 45° there is a more pronounced melting, while the 90° case shows the full melting, easily visible compared to the curves with the horizontal line that represents the area of the diamonds. In particular with the 90° case, in the region $\sim$ 130-170 ns there is a melting plateau that involves all the area of the diamonds. When all the diamonds are liquid the temperature can grow, without absorption of latent heat, since there are not other materials that can melt at this thermal level. In fact, silicon has T_M =1688 K and silicon dioxide has T_M =1986 K, while we have slightly calibrated the dependency of the SiGe melting on the alloy fraction with respect to the linear interpolation considered in the previous chapter and $Si_{0.5}Ge_{0.5}$ has T_M =1381.9 K. Of course, during this stage the molten area remains constant and equal to the area of the diamonds, which motivates the plateau. For the case considered in fig. 5.3 after a while, depending on the laser fluence, the temperature decreases (without reaching the melting temperature of silicon) and after that, around $\sim$ 260-280 ns there is the solidification of the diamonds and so the ending of the thermal plateau. After that there is the well-discussed quenching.

Increasing further the fluence, like in the case shown in fig. 5.4 where the maximum temperature and the melting area of a 35 nm geometry under 0.6 J/cm^2 irradiation are plotted, we can see an overall increase of the temperature. All the polarization values lead to the full melting of the diamonds. The 90° polarization curves show a temperature higher than the melting temperature of silicon (yellow dashed line in the plot) and a molten area bigger than the diamonds, and this means that there was the partial melting of the silicon columns under the diamonds of the melting scenario

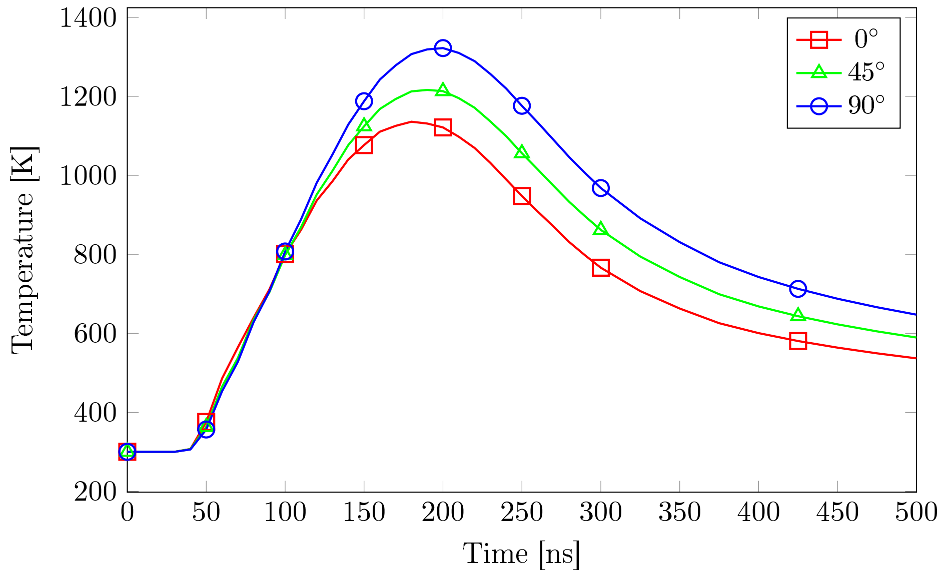

Figure 5.2: *Maximum temperature as a function of time for a MEOL geometry with a pitch of 35 nm and an irradiation process with 0.4 J/cm^2 energy density for the values of 0°, 45° and 90° of laser light polarization. For all laser polarization cases there is no melting.*

of an alloy with the local variation of the alloy fraction. However, differently from the 1D case, we note that the quenching involves the whole figure and the effect in the temperature trend of the intermediate alloy fraction is not easily identifiable.

Increasing the pitch value from 35 nm to 55 nm, the system has a similar behavior, but with a more pronounced difference when different polarization is considered. In particular, considering fig. 5.5, which represents the 55 nm pitch case with a laser fluence of 0.5 J/cm^2, the 0° angle now is a non-melting case, while the 90° case reaches a higher value of the temperature in comparison with the corresponding 35 nm case. The maximum temperature reached in the system is always below the melting temperature of silicon, and as a consequence the maximum melt area is equal to the diamonds one. The 45° case has an overall smaller melting area than those obtained in the corresponding polarization configuration for the 35 nm case.

A qualitative similar trend is followed in the case of a 75 nm pitch: we can observe that the system reaches overall lower temperatures than in the previous case. Also in this case the 90° polarization has the already discussed "hill" of the temperature as a function of the time in the melting stage, but here it is less pronounced.

In the last case considered in this analysis, a 100 nm pitch with a 0.5 J/cm^2 fluence (see fig. 5.7), the fluence is too low to reach the melting temperature, also for the 90° angle of polarization.

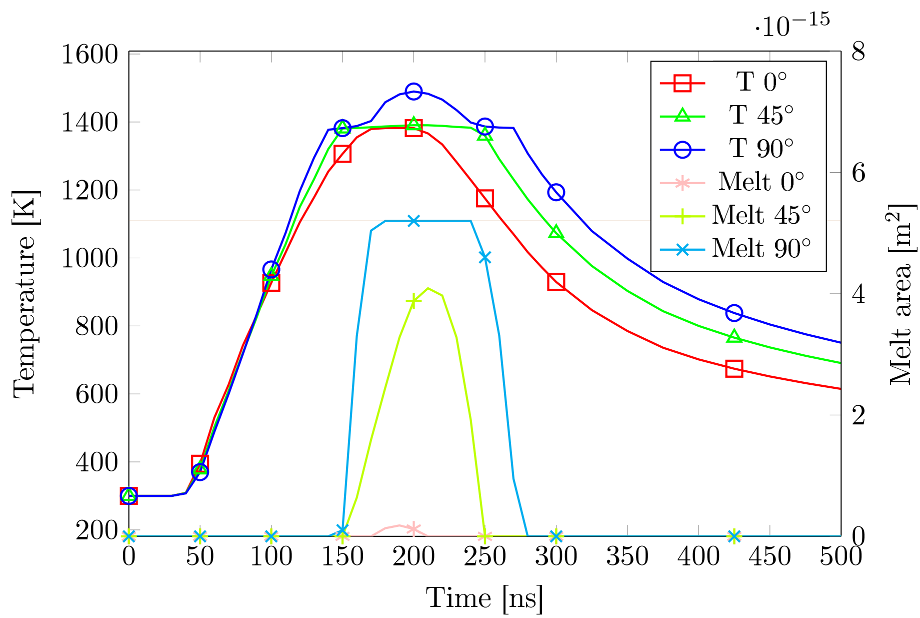

Figure 5.3: *Maximum temperature and total molten area as a function of time for a MEOL geometry with pitch a of 35 nm and an irradiation process with 0.5 J/cm² energy density for the values of 0°, 45° and 90° of laser light polarization. Only the 90° value reaches the full melting of the diamonds, while in the other cases there is only a partial melting of the diamonds. The total area of the diamonds is indicated by the horizontal solid brown line.*

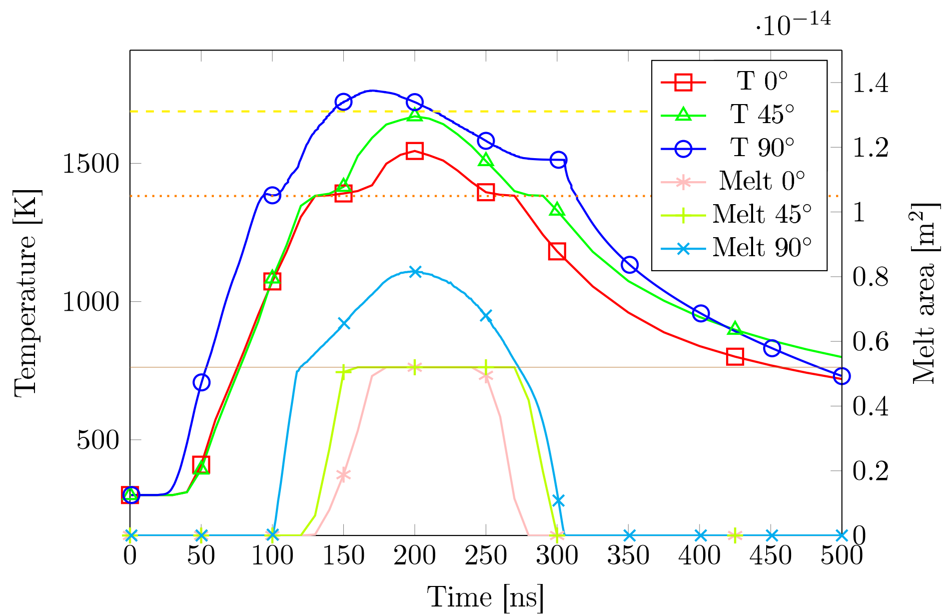

Figure 5.4: *Maximum temperature and total molten area as a function of the time for a MEOL geometry with a pitch of 35 nm and an irradiation process with 0.6 J/cm² energy density for the values of 0°, 45° and 90° of laser light polarization. While in all the cases there is the full melting of the diamonds, only with a laser polarization of 90° there is the partial melting of the silicon columns. The total area of the diamonds is indicated by the horizontal solid brown line. A dotted orange line and a yellow dashed one represent the melting temperature of* $Si_{0.5}Ge_{0.5}$ *and silicon, respectively.*

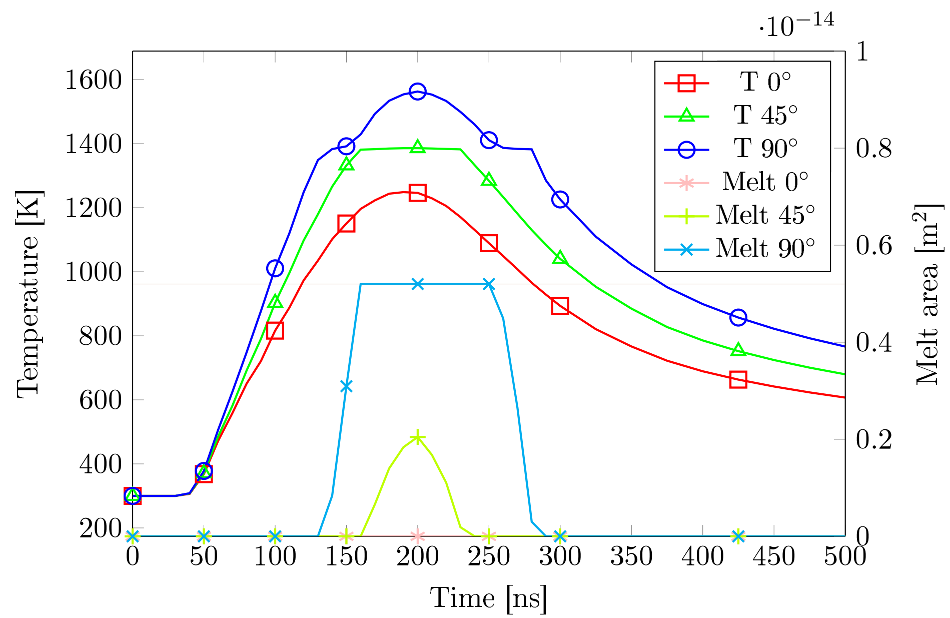

Figure 5.5: *Maximum temperature and total molten area as a function of the time for a MEOL geometry with pitch of 55 nm and an irradiation process with 0.5 J/cm² energy density for the values of 0°, 45° and 90° of laser light polarization. Only the 90° reach the full melting of the diamonds, while the other cases reach a partial melting of the diamonds. The total area of the diamonds is indicated by the horizontal solid brown line.*

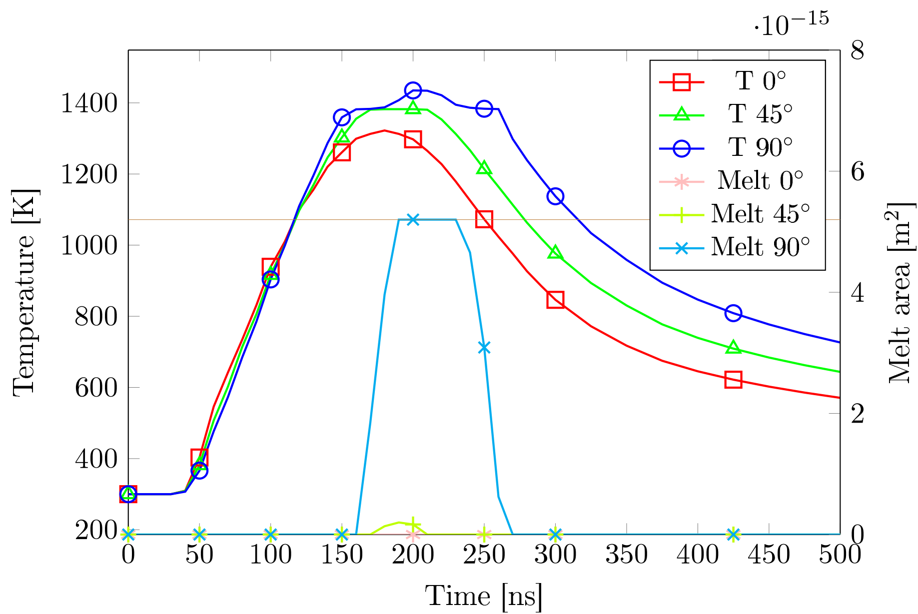

Figure 5.6: *Maximum temperature and total molten area as a function of the time for a MEOL geometry with pitch of 75 nm and an irradiation process with 0.5 J/cm^2 energy density for the values of 0°, 45° and 90° of laser light polarization. The 90° polarization case reaches the full melting of the diamonds, the 45° polarization case is a partial melting case, while for 0° of polarization case there is no melting at all. The total area of the diamonds is indicated by the horizontal solid brown line.*

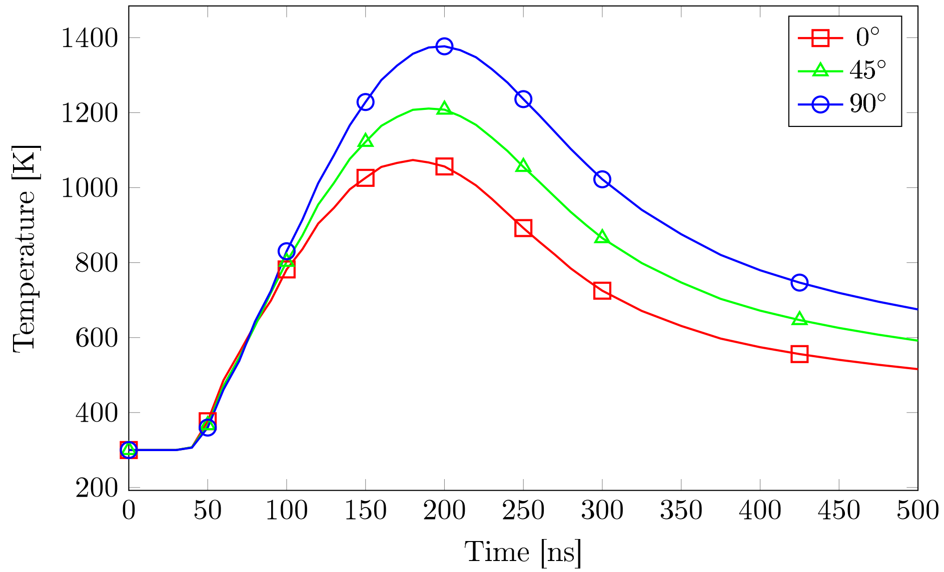

Figure 5.7: *Maximum temperature as a function of time for a MEOL geometry with a pitch of 100 nm and an irradiation process with 0.5 J/cm^2 energy density for the values of 0°, 45° and 90° of laser light polarization. For all polarization angles there is no melting*

5.3.1 Temperature geometry dependencies

In this section we discuss the behavior of the global maximum temperature T_{max}^{global} as a function of the geometric constrain. Similarly to the FinFET case in all the following figures the dashed lines have to be considered simple guidelines due the non-linear effects of the geometrical changes. Figure 5.8 collects all the maximum temperatures reached by the system during the LA process for different geometries and polarization angles with a fixed fluence of 0.5 J/cm^2. Following the 0° we can see a decrease of T_{max}^{global} passing from the "35nm" geometry to the "55 nm" one, an increase for the 75 nm pitch value and another strong decrease for the 100 nm pitch value. The line relative to the 45° polarization angle shows a constant value for the "35-55-75 nm" geometries with a value equal to the melting temperature of the $Si_{0.5}Ge_{0.5}$: this means that for all these geometries there is always a partial melting of the diamonds. In the 100 nm case the temperature is lower, and as a consequence this is a no melting case. The 90° curve has an opposite behavior with respect to the 0° one: increasing for 55 nm, decreasing for 75 nm and with another reduction of T_{max}^{global} for the "100 nm" geometry, without reaching the melting threshold. Also the spreading between the curves has no predictable profile by trivial extrapolation, quite close for the 35nm pitch and even more for the 75 one, while wider for the 55 nm and 100 nm pitches. We plot only the 0.5 J/cm^2 case because the curves for the 0.4 and

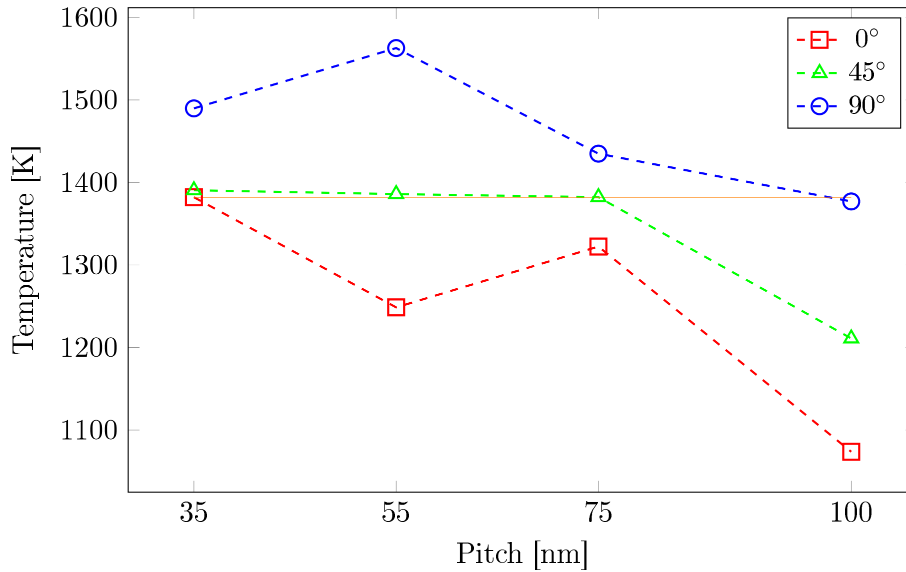

Figure 5.8: *Maximum temperature in the MEOL structure for different pitch and polarization values, in the 0.5 J/cm² case. An orange horizontal line represents the melting temperature of $Si_{0.5}Ge_{0.5}$.*

0.6 J/cm² cases show a similar behavior. Anyway, we should keep in mind that different fluences lead to different maximum temperature values. For the MEOL structure, within the range of values considered, we have not reached a stationary trend, in comparison with the FinFET structure (see Chapter 3, and in particular fig. 3.16 on page 72, cases 225 nm and 270 nm).

From figs. 5.9 to 5.11 we plot the maximum temperature reached in the system for different laser fluence and geometries, changing the polarization. The 0° polarization case shows an overall decrease in temperature when increasing the pitch value, except for the 75 nm geometry where we can observe an increase. The 0.6 J/cm² curve does not exhibit this trend because the maximum temperature is the melting point. The average temperature of the system in the 0° case is the lowest of the series. The general comment is again that the non-linearity of the overall results when the parameters are modified is a crucial feature of the LA process control.

Analyzing the case of 45 ° polarization we derive that the temperature increases with the fluence, and decreases monotonically by increasing the size of the geometry (see fig. 5.10). In this case the maximum temperature of the 0.6 J/cm² curve is always above the melting temperature, i.e. there is melting for all cases, while in the 0.4 J/cm² case no liquid phase is simulated. The 0.5 J/cm² curve reaches the melting temperature only for the "35-55-75 nm" geometry value.

The 90° polarization case shows that the 55 nm pitch value reaches the highest temperature. The average temperature of all curves in the 90° case

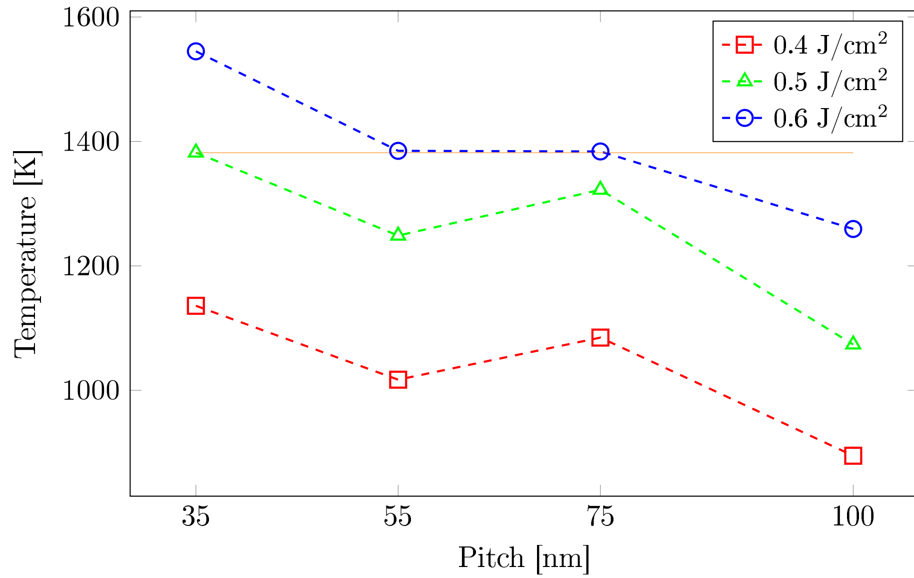

Figure 5.9: *Global maximum temperature for different laser energies, for the 0° polarization. An orange horizontal line represents the melting temperature of the* $Si_{0.5}Ge_{0.5}$.

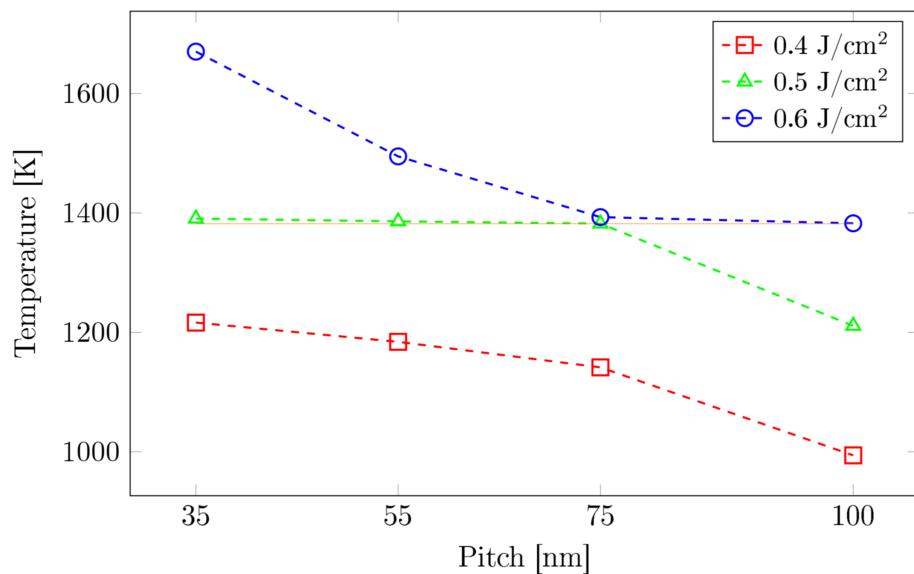

Figure 5.10: *Maximum temperature over time for different laser energies, for the 45° polarization. An orange horizontal line represents the melting temperature of* $Si_{0.5}Ge_{0.5}$.

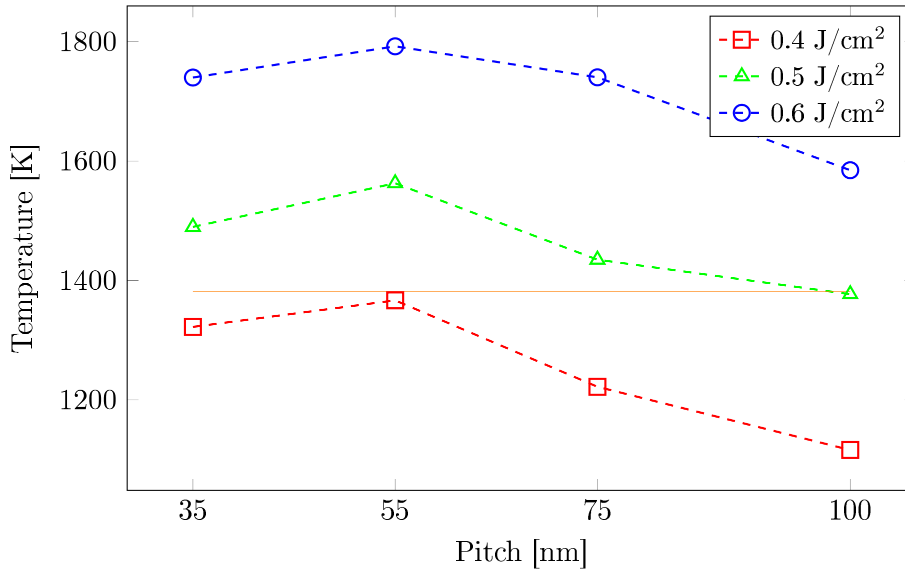

Figure 5.11: *Maximum temperature over time for different laser energies, for a 90° polarization. The orange horizontal line represents the melting temperature of* $Si_{0.5}Ge_{0.5}$.

is the largest with respect to other polarization series. Moreover, for 0.5 and 0.6 J/cm^2 fluences, the temperature is higher than the melting temperature of $Si_{0.5}Ge_{0.5}$: the horizontal line in the figure. For the laser energy density of 0.6 J/cm^2 the temperature is higher than the T_{melt} of silicon and a partial fusion of the columns under the diamonds occurs.

5.3.2 Considerations on the melting area shape

In all the previous plots we have compared only the total value of melting area for the different geometries. This comparison is not exhaustive for the process TCAD in this type of geometry, since in addition to the global value changes, also the shape of the liquid zone is different. For example: considering fig. 5.12, where we report the left diamond for the 35 nm and 75 nm geometries on the left and right plots respectively, the melting area is quite the same but the shape significantly different. Note that the temperature distribution in the structure is rather similar for all geometries due to the thermal conductivity that averages/balances the localized heat sources.

From fig. 5.13 to fig. 5.15 we plot the melting area for different geometries and laser fluence for the different polarization angles. The figures share the same identification rules for the curves meanings. The first one, i.e. fig. 5.13, shows no melting at all for the 0.4 J/cm^2 fluence for all geometries, while for the case of 0.5 J/cm^2 there is only a slight melting in the 35 nm geometry. The case with the higher laser fluence, the 0.6 J/cm^2 one, shows a decrease

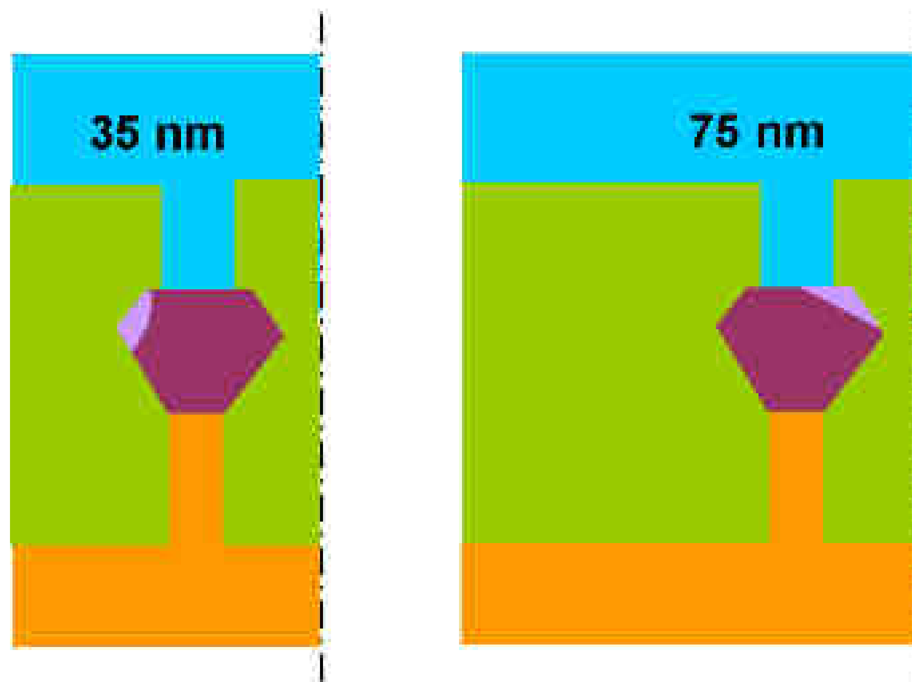

Figure 5.12: *Different melt shape for different pitch geometries, 35 and 75 nm, respectively, in the case of 0° polarization. We show only the left diamond for each geometry, the shape is symmetric for the two diamonds for the same geometry. The melted area is the same but in the opposite side of the diamonds.*

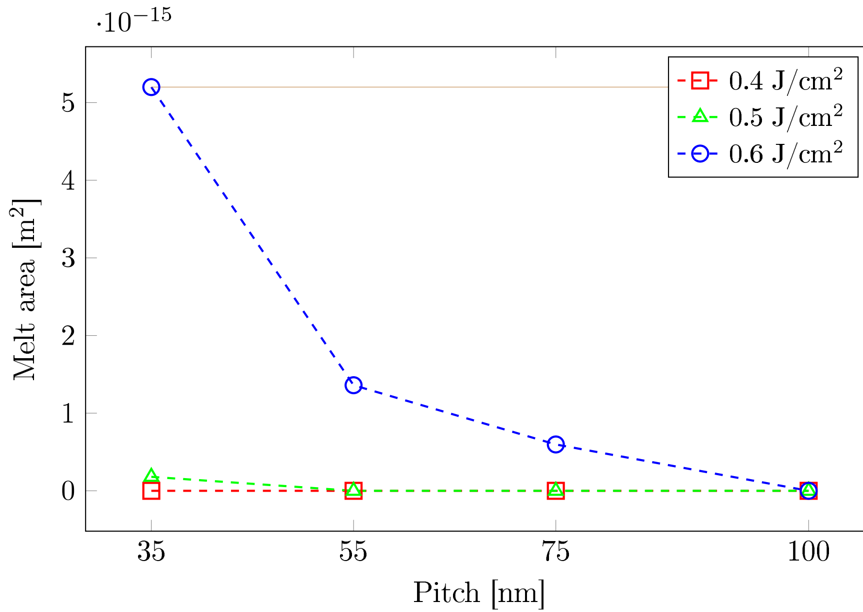

Figure 5.13: *Global maximum melt area for different laser energies, for the 0° polarization case. The total area of the diamonds is indicated by the horizontal solid brown line.*

of the melting area with the increase of the pitch from the full diamond melting (the horizontal line in the figure) to a non melting case.

The 45° angle of the laser polarization is the second graph of the series. For the 0.4 J/cm^2 case there is no melting for any geometry. In the 0.5 J/cm^2 case there is a decrease of the melting area with the increase of the pitch value. In the 0.6 J/cm^2 curve the 35 and 55 nm cases reach the full melting of the diamonds (the horizontal line in the figure), while larger geometries have smaller melting areas.

In the 90° angle case, the last considered in these series, the lower fluence (0.4 J/cm^2) shows no melting for all pitch values. The 0.5 J/cm^2 curve shows the full melting of the diamond (the horizontal line in the figure) for all the geometries except for the 100 nm one. The 0.6 J/cm^2 case exhibits a melting above or equal to the total area of diamonds for all geometries. The 55 nm case shows the highest melting areas.

In fig. 5.16 we plot the melt area in the 0.5 J/cm^2 case for different polarization and geometry values. In the 0° case there is melting only in the 35 nm geometry. In the 45° case there is a decrease of the melting area when increasing the pitch value. In the 90° polarization case, there is the full diamonds melting for all geometries, except for the 100 nm one. With 0.5 J/cm^2 energy density there is no melting at all for the 100 nm geometry, and this corresponds to the fig. 5.8 where the temperature in the 100 nm case never reaches the melting temperature. Again, the brown horizontal

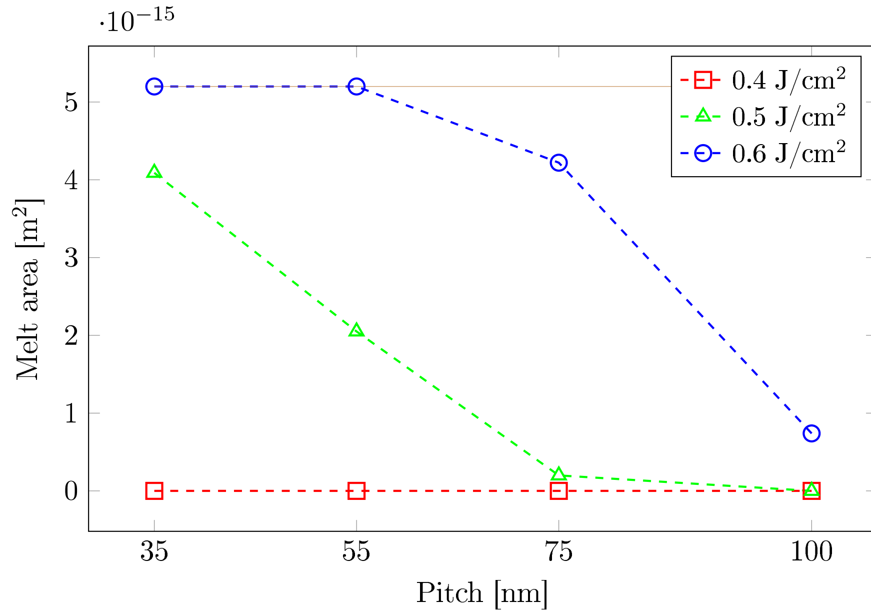

Figure 5.14: *Global maximum melt area for different laser energies, for the 45° polarization case. The total area of the diamonds is indicated by the horizontal solid brown line.*

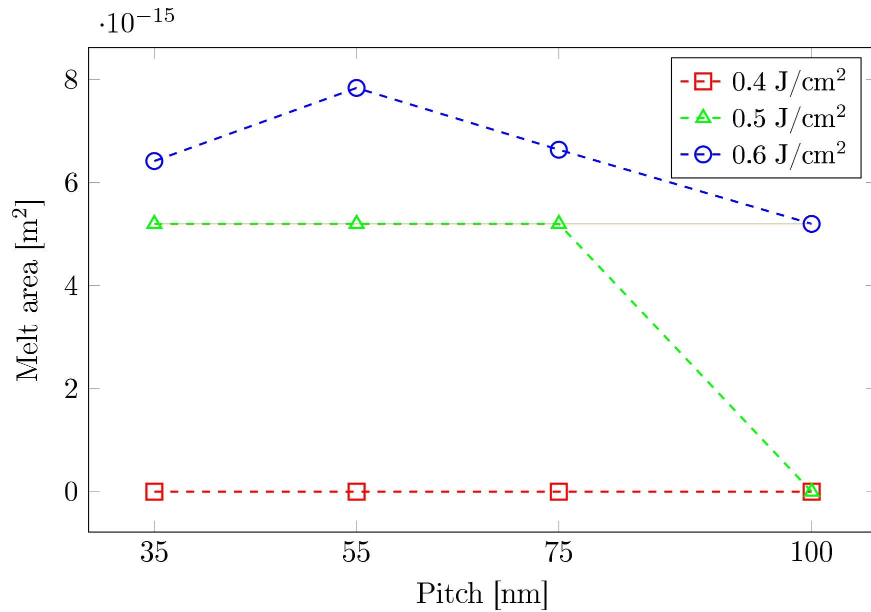

Figure 5.15: *Global maximum melt area for different laser energies, for the 90° polarization case. The total area of the diamonds is indicated by the horizontal solid brown line.*

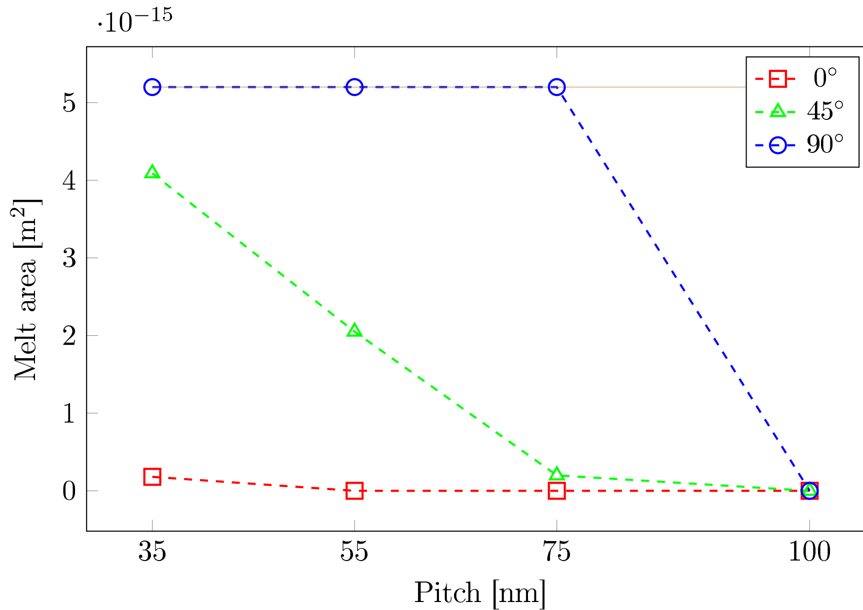

Figure 5.16: *Global maximum melt area for different polarization values, for the 0.5 J/cm^2 case. The total area of the diamonds is indicated by the horizontal solid brown line.*

line represents the total area of diamonds.

5.4 Conclusion

In this chapter, an LA process has been designed for a typical device manufacturing element now considered in the innovative semiconductor manufacturing. The results obtained showed a very strong interaction between the laser source, the materials used and the system response that makes the system highly non-linear and therefore needs the appropriate computational tools to be analyzed. Considering the complex scenario here presented, the main general conclusion is simply the following: the application of LA in nano-device manufacturing makes mandatory simulation campaigns on the proposed structure with a change in geometry, laser power, and polarization with a phase transition model coupled with alloy and impurities distribution. Any pure experiment-based Design of Experiment (DOE) procedure is ineffective or even useless!

6 Conclusion

Advances in technology have resulted in smaller and more powerful computing devices. As a consequence of these technological achievements, currently we have access to a variety of portable personal tools, including wireless telephones such as mobile and smart phones, tablets and laptop computers that are small, lightweight, and easily carried by the users. Further, many of these tools incorporate additional functionality such as digital (video) cameras, digital recorders audio file players. These devices can communicate voice and data packets over wireless networks. Moreover they can process autonomously executable instructions, including software applications with significant computing capabilities implementing the Internet of Things (IoT) paradigm.

Fundamental components of a portable equipment include conventional computer parts like integrated circuits, processors, memory arrays, and so on made by nano-electronic devices (e.g. transistors). Due to the decrease in the size of integrated circuit devices, the complexity of the processes used to prepare the nano-devices has also increased. In this trend towards miniaturization, see the International Technology Roadmap for Semiconductors (ITRS), the ability to simulate the behavior of internal device structures during the process has a crucial role to play in understanding the role of process key parameters and on what and how to act in order to achieve the desired results. A strong complexity arises just thinking to the list of usable materials, temperatures and the whole sequence of upstream and downstream processes.

TCAD software plays a key role in these developments and, to be truly useful and effective, it must evolve accordingly. The main purpose of this PhD thesis, focusing on two "difficult" manufacturing processes, was to develop simulation tools which meet the typical requirements for the use in process design in semiconductor industry production. Starting from the available academic theoretical production in the field we have engineered

the models in order to be of immediate use as real TCAD tools. Moreover, we have also expanded the formalism and its relative implementation in order to consider phenomena barely addressed in the previous scientific literature. To be more specific, we have analyzed those processes that through the use of "modifiable" electromagnetic fields allow the structural modification of the sample. This branch of science is very wide, and it also includes areas far away from the semiconductor technology, such as social fields(see [38]) or medical fields (see [39]), and similar concepts of the numerical tool can be also applied in a broader context; however in the present thesis we focused on plasma and laser processes applied to semiconductor device processing. Here we would like to outline the main achievements obtained with this work.

In the Chapter 1 we deal with plasma processes very useful for applications on thermally sensitive materials which are becoming more and more important today, such as plastic or paper. As a first step we simulated a reactor analyzing at a macro scale its internal electrical thermal and mass transport, in order to find the average process effect on the wafer scale [40]. In the second part using a stochastic approach coupled with the macroscopic one we simulated the nanostructure evolution on the basis of the machine (macro) parameters as required by the usual TCAD paradigm which is difficult to achieve for plasma manufacturing [9].

The second part of the thesis (the largest one) focuses on laser treatments. Chapter 2 provides a theoretical part useful to model this type of process and some comparison between our simulations and experimental data in blanket systems. In the same chapter we have introduced the software with TCAD capabilities able to simulate laser processes. This software was developed, in the framework of two international cooperation projects, to model laser processes and called LIAB (Laser Innovation Application Booster). Among the various features (see the Appendix B for the full description) here we cite the stability, the modularity, the scalable database as well as user friendly capabilities. We have completed this chapter with some examples of the validation and benchmarking activity which always achieve excellent results. We emphasizes that we have tested the code using different materials, with different laser energies (sub-melting and melting conditions) and finally with different geometries (1D and 2D).

After gaining confidence with the newly developed tool we decided to use it as TCAD in typical structures used in micro- and nano-electronics. The first case analyzed is Fin Field-Effect Transistor (FinFET), in the Chapter 3, whose peculiarity lies in the distance to which the various Fin are positioned between them, and hence their mutual relationship (the body size of the Fin, although a key variable, is kept fixed). The simulation showed a strong dependence of the results from the chosen parameters and above all in LA of this non-planar structure emerges the importance of the laser source polarization. Changing polarization means changing the absorption of the energy in different regions of the structure, leading to simulations

whose temperature profiles are deeply different from each other, and this type of relationship varies not monotonously with the dimension of the FinFET pitch. In the tighter geometry case (pitch 35nm) the polarization has, in terms of heat source, an opposite effect than in all the other cases. It has also been shown that, by appropriately matching geometry, power and polarization dimensions, it is possible to diversify the effects on the sample, obtaining configurations with high thermal gradient or uniform annealing, thus changing deeply the thermal evolution of the process in the sample's materials.

We have evolved the code to study particular cases, leveraging the modularity and flexibility that this original code permits to obtain, concentrating on studying amorphous materials and alloys. We firstly developed a new phase field model for simulating the simultaneous presence of 3 phases (liquid, amorphous, crystal) with phase change [41]. The new model was used to study the explosive crystallization phenomenon in 1D domain, and with a broad comparison with a plethora of in-situ and ex-situ characterizations obtaining excellent results. The second evolutionary line instead adds a new variable that takes into account self-consistently the alloy fraction.

This alloy model was used to analyze in the last Chapter 5 another typical semiconductor geometry, the Middle-End-Of-Line, in a 2D configuration. In this case the studied geometric variance, which represents the distance between the various channels, leads as expected to a big difference in the simulation results. The influence of polarization also in this case is crucial to produce different behaviors between the various cases. Finally the use of a variable such as the alloy fraction that changes over time, according to the liquid phase evolution, which varies the temperature of the melting and latent heat creates great stability issues in the code which have been solved exploiting the great flexibility of the implemented front tracking method.

6.1 Future development

Following the *Red Queen hypothesis* it is crucial for a software, like any other organism, that wants to survive in a competitive world to continue to evolve to meet external needs. Thanks to the experience developed during this period of PhD, there are some topics that will be interesting to study in the future, just to make the software progress and approaching the experimental demands to have a better predictive capacity.

An important remaining work for our TCAD tool is to extend the database with a greater number of materials and, above all, to improve the existing parameters because they are not always complete (as a function of the temperature or alloy fraction). Many materials listed in Appendix A have parameters that do not depend on temperature. This is a problem, as a source of inaccuracy in self-consistent codes. This is true for less explored materials

but also for materials that should be perfectly known as silicon. An experimental campaign aimed at filling these gaps would give greater confidence to the obtainable results. Amorphous materials in the first place could play a key role in the future of the code. As already seen in Chapter 4, normal production processes involve a doping phase, which is often done with ionic implantation that tends to amorphize the material. It is therefore common practice to have amorphous domains that are properly modeled in order to have a correct prediction of the result. Referring to the results of Chapter 3 it is worth noting that small geometric differences can create great differences in the result, see in particular the difference between geometries 35 and 45 nm, where only 10 nm change the very essence of the system response. Just having in mind this profound non-linearity of the problems faced, it should be noted the importance of using sophisticated production processes as well as simulations conducted with an adequate degree of miniaturization and always producing a similar result with very low production tolerances. From the calibration side understanding the effects of the size constrains in the thermal properties or even in the "thermal energy" transport mechanism is a big future challenge. Another interesting field to investigate is the mechanical stress induced by the thermal field, both during the process and as residual stresses. This parameter is important in a device to be marketed because a high rate of tension could compromise its reliability with easily imaginable consequences. To solve this problem, it would be necessary to couple the models here presented with a structural analysis or even better with a fatigue analysis. The last interesting but fundamentally challenging topic is to be able to apply a model as complete as possible to a 3D geometry. We have seen the importance of spatial distribution of the elements between Chapter 2 and Chapter 3 and also Chapter 5, so we expect that a possible transition to 3D can lead to a higher level of knowledge. It should be noted, however, that among the proposals listed above, this has to deal with problems of non-simple resolution, not so much for implementing the code itself as in the technical-economic feasibility of modeling such a complex system, where computational requests are not trivial.

Material Parameters

A.1 Introduction

The aim of the present appendix is to report the complete set of material parameters that have been used in the simulations.

A.1.1 Phases

The materials in this thesis could be in 3 phases and are:

Crystal The common solid phase of each material. Energetically, this structure has the lowest free energy and is therefore the most stable one. The extension of the symmetry of this structure defines the quality of the crystal which is called polycrystalline when composed of different crystalline regions (grains).

Liquid Generally the typical properties are high thermal conductivity and reflectivity. Energetically, the liquid phase is in a state of much higher free energy than the solid.

Amorphous The amorphous structure is different from the crystalline one because in that the bonds are stretched, bent or broken and reformed. These variations are nevertheless quite small and give rise to a certain short-range order while a large-range order is lost. The fact, that the amorphous structure is not very well defined implies that not a simple amorphous state exists but a continuum of different thermodynamic states with different properties, each corresponding to a certain deviation from the ideal crystalline structure.

A.1.2 Dopant

The addition of a small percentage of foreign atoms in the regular crystal lattice of silicon or germanium produces dramatic changes in their electrical properties, producing n-type and p-type semiconductors.

N-Type semiconductor The addition of pentavalent impurities such as antimony, arsenic or phosphorous contributes free electrons, greatly increasing the conductivity of the intrinsic semiconductor. The addition of donor impurities contributes electron energy levels high in the semiconductor band gap so that electrons can be easily excited into the conduction band. This shifts the effective Fermi level to a point about halfway between the donor levels and the conduction band.

P-Type semiconductor The addition of trivalent impurities such as boron, aluminum or gallium to an intrinsic semiconductor creates deficiencies of valence electrons,called "holes". The addition of acceptor impurities contributes hole levels low in the semiconductor band gap so that electrons can be easily excited from the valence band into these levels, leaving mobile holes in the valence band. This shifts the effective Fermi level to a point about halfway between the acceptor levels and the valence band.

A.2 Material set

The following table shows a summary of the parameters, their description and units of measure that will be repeated for every material. The T in many values represents the temperature in Kelvin. k_b is the Boltzmann constant.

The diffusion coefficient uses as superscript the symbol of the impurity atom. Each material has a different set of possible dopants.

Parameter	Description	Unit
L	Latent heat	J/g
T_M	Melting temperature	K
C_p	Thermal capacitance	J/(g· K)
ρ	Density	g/cm^3
K	Thermal conductivity	W/(cm ·K)
A	Speed prefactor	m/s
E_a	Speed activation energy	eV
N	Atomic density	1/cm^3
μ	interface mobility	cm^4/(J · s)
σ		J/cm^2
n	Index of refraction	
k	Extinction coefficient	
n$_{probe}$	Index of refraction of the probe	
k$_{probe}$	Extinction coefficient of the probe	a.u.
D	Diffusion coefficient	cm^2/s
k$_{out}$	Out of diffusion coefficient	m/s

Table A.1: *Data parameter meanings*

A.3 Silicon

Silicon is a chemical element with symbol Si and atomic number 14. A hard and brittle crystalline solid with a blue-gray metallic luster, it is a tetravalent metalloid. It is a member of group 14 in the periodic table, along with carbon above it and germanium, tin, and lead. It is not very reactive, although more reactive than carbon, and has great chemical affinity for oxygen; it was first purified and characterized in 1823 by Jöns Jakob Berzelius.

Silicon is the eighth most common element in the universe by mass, but very rarely occurs as the pure element in the Earth's crust. It is most widely distributed in dusts, sands, planetoids, and planets as various forms of silicon dioxide (silica) or silicates. Over 90% of the Earth's crust is composed of silicate minerals, making silicon the second most abundant element in the Earth's crust (about 28% by mass) after oxygen. Most silicon is used commercially without being separated, and often with little processing of the natural minerals. Such use includes industrial construction with clays, silica sand, and stone.

Elemental silicon also has a large impact on the modern world economy. Most free silicon is used in the steel refining, aluminium-casting, and fine chemical industries (often to make fumed silica). Even more visibly, the relatively small portion of very highly purified silicon used in semiconductor electronics (< 10 %) is essential for integrated circuits. Most computers, cell phones, and modern technology depend on it. Silicon is the basis of the widely used synthetic polymers called silicones. The transition parameter used in the dual component dopant simulation is

$$k_{\tau}^{Si} = 1\text{E}7 \quad [1/\text{s}]$$

Parameter	Amorphous	Crystalline	Liquid
L	1317	1797	/
T_M	1420	1688	/
C_p	$1\text{E-}3\left(\frac{10 \cdot T^{1.034}}{1.02 + 0.01 \cdot T} - 213\right)$	C_{pa}	1.045
ρ	2.1	2.32	2.52
K	$\begin{cases} 1.8\text{E-}3 & \text{if } T \leq 420 \\ 1\text{E-}3 \cdot (1.8 + (2.5\text{E-}5 \cdot T - 420)^2) & \text{if } T > 420 \end{cases}$	$\begin{cases} 1523.7 \cdot T^{-1.226} & \text{if } T \leq 1200 \\ 9 \cdot T^{-0.502} & \text{if } T > 1200 \end{cases}$	$0.502 + 2.93\text{E-}4\,(T - T_{Mc})$
A	1E5	1E5	/
E_a	0.32	0.42	/
N	4.9E22	5E22	/
μ	600	600	/
σ	2.75E-5	3.45E-5	/
n	3.35	5.0814	1.22
k	3.3	3.735	4.15
n_{probe}	4.2023	3.869	1.22
k_{probe}	0.4157	0.016	3.31
D^{Si}	1E-10	1E-10	HD = 4E-4

Continued on next page

Table A.2 – continued from previous page

Parameter	Amorphous	Crystalline	Liquid
			LD =8e-6
D^{Si}	1E-10	1E-10	$\begin{cases} \text{2E-4} \\ HD = \text{4E-4} \\ LD = \text{8E-4} \end{cases}$
D^{B}	D$_c^B$	$\text{8.7E+7} \cdot \exp\left(\frac{-3.46}{k_b \cdot T}\right)$	$\begin{cases} \text{3.3E-4} \\ HD = \text{3.3E-4} \\ LD = \text{6.6E-6} \end{cases}$

Table A.2: *Data parameter of Silicon*

A.4 Germanium

The name is due to the country of its discovery. The existence of Ge was predicted by Mendeleev in 1871 as "Ekasilikon" and the element was found by Winkler, a professor of Chemistry, in 1886. Ge is a silvery white brittle semiconductor of the carbon group in the periodic system. It is stable in air and water and is unaffected by alkalis and most acids. Its physical properties are very similar to those of Silicon which precedes it in the same group. Whereas Si is the most abundant element on earth, Ge is found only in trace amounts in some coals and ores. Pure Ge is produced by reduction of the oxide and ultra high purity material is obtained by zone refining. Ge is a poor conductor of electricity but has exceptional properties as a semiconductor material on account of photoconductivity. The transition parameters used in the dual component dopant simulations are

$$k_\tau^P = 1.4\text{E}7 \quad [1/\text{s}]$$
$$k_\tau^{As} = 1.5\text{E}7 \quad [1/\text{s}]$$

Parameter	Amorphous	Crystalline	Liquid
L	350	510	/
T_M	965	1210	/
C_p	$1.72\text{E-}4{\cdot}T + 0.29$	$1.17\text{E-}4{\cdot}T + 0.293$	0.46
ρ	5.32	5.32	$5.6 - 0.625\text{E-}3 \cdot (T - T_{Mc})$
K	0.158	$0.602 \cdot \left(\frac{T}{300}\right)^{-1.25}$	0.297
A	5E4	0.3E4	/
E_a	0.52	0.5	/
N	4.15E22	4.56E22	/
μ	600	600	/
σ	1.8E-5	3.45E-5	/
n	2.7	3.993	1.18
k	2.77	3.398	3.398
n_{probe}	4.667	5.44	3.26
k_{probe}	1.362	0.691	5.92
D^P	$8.7\text{E+}7 \cdot \exp\left(\frac{-3.46}{k_b \cdot T}\right)$	$8.7\text{E+}7 \cdot \exp\left(\frac{-3.46}{k_b \cdot T}\right)$	$\text{HD} = 0.21{\cdot} \exp\left(\frac{-0.6}{k_b \cdot T}\right)$

Continued on next page

Table A.3 – continued from previous page

Parameter	Amorphous	Crystalline	Liquid
			LD $=4.2\text{E-}3 \cdot \exp\left(\frac{-0.6}{k_b \cdot T}\right)$
D^{P}	$8.7\text{E}{+}7 \cdot \exp\left(\frac{-3.46}{k_b \cdot T}\right)$	$8.7\text{E}{+}7 \cdot \exp\left(\frac{-3.46}{k_b \cdot T}\right)$	$\begin{cases} 0.07 \exp\left(\frac{-0.6}{k_b T}\right) \\ HD = 0.21 \cdot \exp\left(\frac{-0.6}{k_b \cdot T}\right) \\ LD = 4.2E - 3 \cdot \exp\left(\frac{-0.6}{k_b \cdot T}\right) \end{cases}$
k^{P}_{out}	$2.8\text{E}2 \cdot \exp\left(\frac{-0.8}{k_b \cdot T}\right)$	$2.8\text{E}2 \cdot \exp\left(\frac{-0.8}{k_b \cdot T}\right)$	HD=0.47 LD=0.04
D^{As}	1E-10	1E-10	HD = 3.84E-4 LD =3.84E-5

Table A.3: *Data parameter of Germanium*

A.5 Silicon Germanium

SiGe, or silicon-germanium, is an alloy with any molar ratio of silicon and germanium, i.e. with a molecular formula of the form $Si_{1-x}Ge_x$. It is commonly used as a semiconductor material in integrated circuits (ICs) for heterojunction bipolar transistors or as a strain-inducing layer for CMOS transistors. IBM introduced the technology into mainstream manufacturing in 1989. This relatively new technology offers opportunities in mixed-signal circuit and analog circuit IC design and manufacture. SiGe is also used as a thermoelectric material for high temperature applications ($\geq$ 700 K).

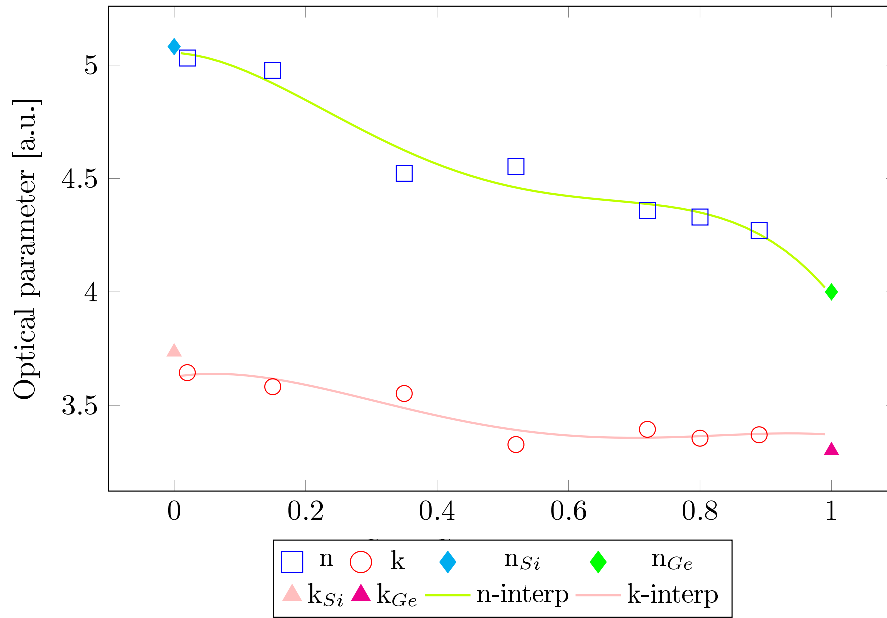

Figure A.1: *Optical parameter n and k for $Si_{1-x}Ge_x$. The solid lines are he interpolation curves used in the database. On the 0 and 1 side are also reported the n and k value for pure Silicon and Germanium, respectively.*

A.5.1 $Si_{0.5}Ge_{0.5}$

In the Chapter 2 we use the silicon germanium in the $Si_{0.5}Ge_{0.5}$ composition, so here we propose a subsection with the characteristics of this particular material.

Parameter	Crystalline	Liquid
L	1797-1287X_{Ge}	/
T_M	$273.15+\left(1412 - 738X_{Ge} + 263X_{Ge}^2\right)$	/
C_p	$\frac{1}{m_{SiGe}}(19.6 + 2.9X_{Ge})$	0.39
ρ	(2.329+3.493X_{Ge}-0.499X_{Ge}^2)	(2.52*(1-X_{Ge})+5.633X_{Ge})
K	0.046+0.084X_{Ge}	0.428
A	0.3E4	/
E_a	0.5	/
N	$(5 - 0.58X_{Ge})$*1E22	/
n	$\left(-7.5143X_{Ge}^4 + 13.509X_{Ge}^3 - 6.9265X_{Ge}^2 - 0.1374X_{Ge} + 5.0544\right)$	$(1.18X_{Ge}) + (1 - X_{Ge}) \cdot 1.22$
k	-2.9112 X_{Ge}^4+6.5857 X_{Ge}^3-4.3904 X_{Ge}^2+0.4605 X_{Ge}+3.6258	$(3.398X_{Ge}) + (1 - X_{Ge}) \cdot 4.15$

Table A.4: *Data parameter of* $Si_{1-X}Ge_X$. $m_{SiGe} = (1 - X_{Ge}) * 28.0855 + X_{Ge} * 72.61))$

Parameter	Crystalline	Liquid
L	1153.5	/
T_M	1381.9	/
C_p	0.418	0.39
ρ	3.951	4.0765
K	0.088	0.428
A	1000	/
E_a	0.42	/
N	4.71E22	/
n	4.478	1.2
k	3.393	3.774

Table A.5: *Data parameter of* $Si_{0.5}Ge_{0.5}$.

A.6 Copper

Copper is a chemical element with symbol Cu (from Latin: cuprum) and atomic number 29. It is a soft, malleable, and ductile metal with very high thermal and electrical conductivity. A freshly exposed surface of pure copper has a reddish-orange color. Copper is used as a conductor of heat and electricity, as a building material, and as a constituent of various metal alloys, such as sterling silver used in jewelry, cupronickel used to make marine hardware and coins, and constantan used in strain gauges and thermocouples for temperature measurement.

Parameter	Cristalline	Liquid
L	231	/
T_M	1356	/
C_p	481	531
ρ	8.960	$8.938 - 7.367\text{E-4} \cdot T^1$
K	$4.187 - 7.509\text{E-4} \cdot T$	$0.897 + 4.98\text{E-4} \cdot T$
A	1.3E3	/
E_a	0.45	/
N	8.49E22	/
n	1.3267	0.01
k	1.7280	2
n_{probe}	0.1086	1
k_{probe}	3.6067	5

Table A.6: *Data parameter of copper.*

A.7 Silicon Dioxide

Silicon dioxide, also known as silica (from the Latin silex), is an oxide of silicon with the chemical formula SiO_2, most commonly found in nature as quartz and in various living organisms. Silica is one of the most complex and most abundant families of materials, existing as a compound of several minerals and as synthetic product. Notable examples include fused quartz, fumed silica, silica gel, and aerogels. It is used in structural materials, microelectronics, and as components in the food and pharmaceutical industries.

Parameter	Amorphous
T_M	1986
C_p	$0.7074 + 2.989\text{E-}4 \cdot T$
ρ	2.2
K	$\begin{cases} 1.005 + 1.298\text{E-}3 \cdot T & \text{if } T \leq 1170 \\ 2.512 \cdot T & \text{if } T > 1170 \end{cases}$
n	1.4984
k	0.0001208

Table A.7: *Data parameter of Silicon dioxide.*

A.8 Dielectric materials

We list here several materials that have a very similar purpose as they are used as dielectrics

LowK In semiconductor manufacturing, a low-κ is a material with a small dielectric constant relative to silicon dioxide. Although the proper symbol for the dielectric constant is the Greek letter κ (kappa), in conversation such materials are referred to as being "low-k" (low-kay) rather than "low-κ" (low-kappa). In digital circuits, insulating dielectrics separate the conducting parts (wire interconnects and transistors) from one another. Replacing the silicon dioxide with a low-κ dielectric of the same thickness reduces parasitic capacitance, enabling faster switching speeds and lower heat dissipation.

Silicon nitride Silicon nitride is a chemical compound of the elements silicon and nitrogen, with the formula Si_3N_4. It is a white, high-melting-point solid that is relatively chemically inert.

TaN Tantalum nitride (TaN) is an inorganic chemical compound. It is sometimes used to create barrier or "glue" layers between copper, or other conductive metals, and dielectric insulator films such as thermal oxides. These films are deposited on top of silicon wafers during the manufacture of integrated circuits, to create thin film surface mount resistors and has other electronic applications.

TiN Titanium nitride (TiN) (sometimes known as tinite) is an extremely hard ceramic material, often used as a coating on titanium alloys, steel, carbide, and aluminium components to improve the substrate's surface proper-

Parameter	Amorphous
T_M	1986
C_p	$500 + 1.05 \cdot T - 3.7\text{E-4} \cdot T^2$
ρ	2.2
K	$\begin{cases} 1.005 + 1.298\text{E-3} \cdot T & \text{if } T \leq 1170 \\ 2.512 \cdot T & \text{if } T > 1170 \end{cases}$
n	2.26
k	0

Table A.8: *Data parameter of low-κ.*

Parameter	Amorphous
T_M	2500
C_p	0.7
ρ	3.27
K	0.29
n	2.256
k	0.05

Table A.9: *Data parameter of silicon nitride.*

Parameter	Amorphous
T_M	2500
C_p	0.21
ρ	13.8
K	0.0831
n	2.1
k	1.1

Table A.10: *Data parameter of tantalium nitride.*

Parameter	Amorphous
T_M	2500
C_p	$1\text{E-}2 \cdot \big(-5\text{E-}16 \cdot T^6 + 4\text{E-}12 \cdot T^5 - 1\text{E-}08 \cdot T^4 +$ $+2\text{E-}05 \cdot T^3 - 0.0129 \cdot T^2 + 5.8105 \cdot T - 319.44\big)$
ρ	5.4
K	$1\text{E-}2{\cdot}(1\text{E-}10{\cdot}T^4{-}4\text{E-}7{\cdot}T^3{+}$ $+0.0005 \cdot T^2 - 0.3206 \cdot T + 87.054)$
n	2.36934
k	1.1585

Table A.11: *Data parameter of titanium nitride.*

ties. Applied as a thin coating, TiN is used to harden and protect cutting and sliding surfaces.

A.9 Tungsten

Tungsten, also known as wolfram, is a chemical element with symbol W and atomic number 74. Tungsten is a hard, rare metal (under standard conditions, when uncombined), and is found naturally on Earth almost exclusively in chemical compounds. The free element is remarkable for its robustness, especially the fact that it has the highest melting point of all the elements discovered, melting at 3695 K (3422 °C). Polycrystalline tungsten is an intrinsically brittle and hard material, making it difficult to work. However, pure single-crystalline tungsten is more ductile, and can be cut with a hard-steel hacksaw.

Parameter	Crystalline
T_M	3683
C_p	1.2085E-15 $\cdot T^5 -$1.0508E-11$\cdot T^4 +$ $+$3.827E-8$\cdot T^3 -$ 6.266E-5 $\cdot T^2 +$ 6.475E-2 $\cdot T +$ 117.69
ρ	$-$4.4717E-5 $\cdot T^2 -$ 1.7140E-1 $\cdot T +$ 19404.83
K	-3.984E-15$\cdot T^5 +$ 4.529E-11 $\cdot T^4 -$ 1.976E-7 $\cdot T^3 +$ $+$ 4.150$\cdot T^2 -$ 4.321E-1 $\cdot T +$ 271.192
n	0.43
k	3.95
n_{probe}	0.2521
k_{probe}	5.1246

Table A.12: *Data parameter of tungsten.*

A.10 Air

The atmosphere of Earth is the layer of gases, commonly known as air, that surrounds the planet Earth and is retained by Earth's gravity. The atmosphere of Earth protects life on Earth by absorbing ultraviolet solar radiation, warming the surface through heat retention (greenhouse effect), and reducing temperature extremes between day and night (the diurnal temperature variation).

By volume, dry air contains 78.09% nitrogen, 20.95% oxygen, 0.93% argon, 0.04% carbon dioxide, and small amounts of other gases. Air also contains a variable amount of water vapor, on average around 1% at sea level, and 0.4% over the entire atmosphere.

Parameter	gas
T_M	3000
C_p	$1\text{E-}3\cdot\left(1047 - 0.373 \cdot T + 9.45\text{E-}4 \cdot T^2 + -6.02\text{E-}7 \cdot T^3 + 1.29\text{E-}10 \cdot T^4\right)$
ρ	$1\text{E-}6 \cdot \frac{28.96}{0.0821} \cdot T$
K	$1\text{E-}2 \cdot \left(-0.0023 + 1.15\text{E-}4 \cdot T - 7.9\text{E-}8 \cdot T^2 + +4.12\text{E-}11 \cdot T^3 - 7.44\text{E-}15 \cdot T^4\right)$
n	1
k	0

Table A.13: *Data parameter of air.*

B

The graphic interface Laser innovation application booster

In this appendix we present the LIAB Graphic User Interface (GUI), in the development stage, used for simulation of LA process.

The use of the software goes through the choices necessary to properly implement the model, in particular here we report a couple of screenshots of the GUI and explain its operations steps.

The main window, see fig. B.1, reports in the main bar the SCREEN logo and date/time, in the middle title of the tab, in this case *Project and Recipe*. On the left are the various tabs, divided into 3 conceptual sections, and we are as the suggested by title in the 2D Recipe tab. The central area allows you to go into detail and set every detail of the 2D structure to be used in the simulation. The task to do here is to choose a structure file, which is the joining of a geometry file (selectable in the center zone and the figure is an empty field) and the domain description including their features. In detail, for each domain, the user must assign a name (useful for easy identification), a database material and its phase (*crystal, amorphous or liquid*, or a alloy and the corresponding spatial profile, activate or no the resolution of the phase equations combined with the mesh refinement field allows a computational saving when correct user defined choices are picked. This aspect is important for project management because it is possible to create and save geometry, indicating the features of each domain to create the complex structure file. At this point it is very convenient to be able to reuse the same geometry using different materials, the new correspondence materials/geometry saved with a different structure name will create 2 distinct files from a single geometry. In the right part the the screenshot there

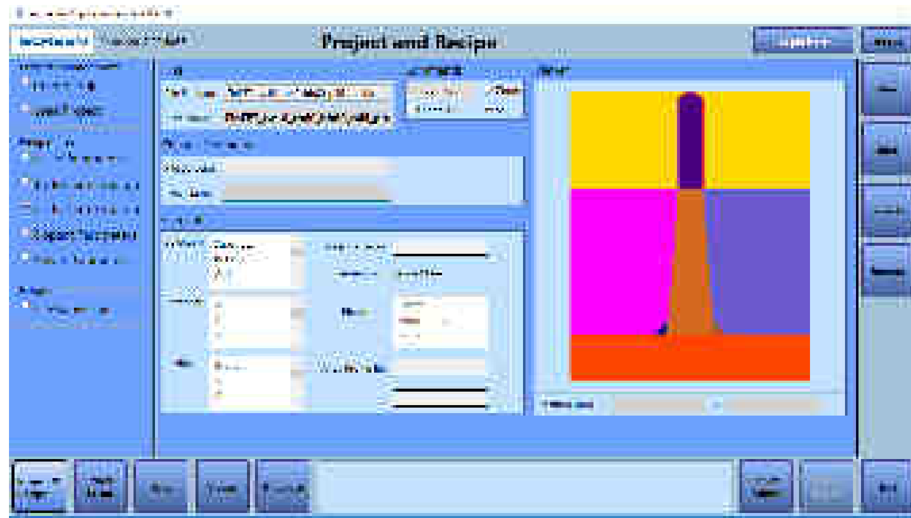

Figure B.1: *Screenshot of the LIAB GUI, a FINFET device is shown and the different colors indicate the domains, which can be initialize with different materials properties.*

is a figure representing geometry chosen with each colored domain in a different way. In the far right, commands allow panel management in this case for creating and saving the structure. Bottom left there are buttons macro that allow you to switch to different usage profiles. Indeed, they divide the recipe, which we now find in the CAD designer, to process the resolutions (with jobs) to the viewer after obtaining the results of the simulation and end to the database tab. The lower right and top left commands are used to configure access to the computing server set. We note the 1D menu is practically the same as the one used for defining a 2D geometry. The Laser parameter tab allows you to recall one of the preset laser profiles, fluence and polarization. The solver parameter tab handles the size of the mesh, the duration of the simulation, the output step. File converter helps in transforming user profiles, lasers, etc., into profiles that are compatible with the program. Create and load project allows profiling to be easily reused for subsequent simulations.

The tab **Structure Editor** (not shown) is a simple CAD that can draw point-to-point structures. the structures created can be recalled in the main-tab project and recipe.

In fig. B.2 is reported the **Viewer**, as indicated by the main bar and the bottom button. on the left are the resolved files that you can view, in the center the plot parameters (for x and y axis) and at the center the actual plot. Just above the buttons to load the simulation there is the *Export* key.

The last screenshot, fig. B.3 shows the database. From left to right there is the choice of materials, the choice of the stage, the software automatically

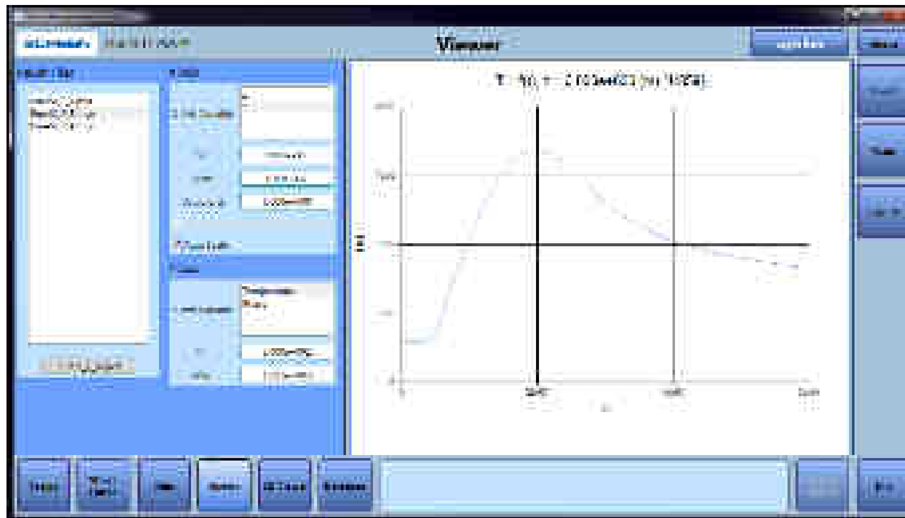

Figure B.2: *Screenshot of the LIAB GUI, the viewer panel permits to see the results of the simulations. In the image the surface temperature for a 1D simulation.*

discriminates the materials that have more than one phase and the choice of the parameters to be displayed. The picture shows the thermal conductivity of crystalline silicon. The formula used is shown at the top and the parameters are inserted below. The formulation is free, and it can go from a constant value to a more complex formula as shown here. Note how the formula uses temperature T as the parameter T. On the right part of this screenshot, the various buttons permit the user to modify the data, save the changes or return them to the default. This panel is very important because each user can customize the material used if it is not present in the database library.

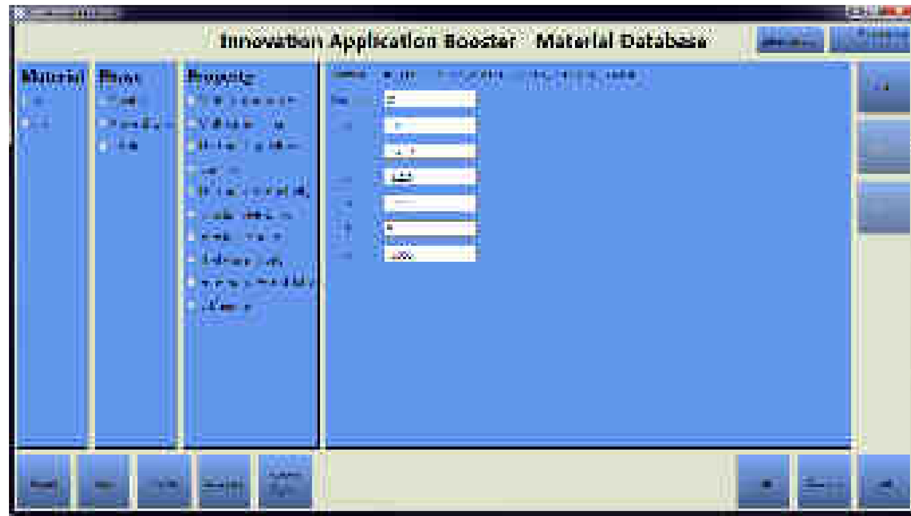

Figure B.3: *Screenshot of the LIAB GUI, the database mask. On the extreme left there is the choice of the material (here only silicon and germanium are present) than the phase and the relative property. On the right the formula of the thermal conductivity with its constant used.*

B.1 Solver

The solver core is written with the FEniCS software in python language. The equations implemented are the same described in Chapter 2. The link between the solver and the GUI is in the assignment of the properties in the domains. Models of laser annealing process have been developed in the past by our team for particular limited applications and implemented in academic or commercial packages [12–14, 32]. However, the development of the LIAB TCAD tool is essential to overcame the limitation of other packages (see e.g. discussion in Ref. [33]), especially when modeling complex structures with $\sim$ nm wide elements made of different materials/phases with concurrent phase changes.

Acknowledgments

Catania, october 2017

I would like to acknowledge Prof. Maria Grazia Grimaldi, for giving me the chance to switch my PhD study to irradiated laser systems. I would like to thank Dr. Antonino La Magna for guidance, support and patience during this period of PhD. The desire to do more and more, the instinct and the knowledge to find new solutions and its indomitable sense of duty have been an example. It will be difficult to forget the innumerable car trips, the instantaneous jokes, and his smile to face the huge amount of daily work. I am grateful to Dr. Ioannis Deretzis, my roommate at CNR-IMM, for his attention, availability and preparation, his computational support, and the ultimate revision of the present thesis. He is the perfect blend of ancient greek wisdom and modern computational materials science. I would like to thank Dr. Karim Huet of SCREEN Semiconductor Solutions Co. for giving me the opportunity to work for three months in the SCREEN-LASSE laboratory in Gennevillers, France. This period greatly improved the development of the LIAB tool presented on Chapter 2. I would like to thank also Armand Verstraete for the hospitality. I want to thank one by one the CNR-IMM guys: the matriarch Gabriella, the doyen Michele, the overflowing Simona, the laconic Daniele, the frail Marzia, the seraphic Salvo, the stoic Valentina and the pugnacious Sebastiano. A thanks also to all the other who have passed through (as well as a greeting to all those who will come after): Rosa, Emanuele, Cristina, Antonio, Alessandra, Giovanni, Silvia, Salvo B., Rosaria, Luca, Francesca, Claudio, Monia, Alberto, Emanuela, Enzo, Roberta, Giovanni and in particular Alessio and Giuseppe.

A heartfelt thanks goes to my lifetime friends, whose the thought of meeting each other gave me new energies to continue this difficult journey, Andrea and Veronica, but I do not forget Concetto, Renzo, Alessandro, Giuseppe

and Ilaria. I would like to thank my family who has always supported me, each with its capabilities in everything I needed, my dad Pino, my mom Agata and my sisters Sofia and Flavia. Finally, I would like to thank my wife, Maria Agata, for the dedication, patience and love with which she has accompanied me in this very intense period, and not only. She bear and supported me in a useful and sweet way. If it was a good and profitable time, it's thanks to her that was always close to me. May this be a springboard for our lives.

Curriculum vitae

Salvatore Francesco Lombardo was born on the 3rd of october 1983 in Catania. He obtained his Degree in mechanical engineering at the University of Catania in 2013. In 2014 he was admitted to the Ph.D. course in Materials Science and Nanotechnology at the University of Catania (Department of physics and astronomy), developing his research activities in collaboration with the Institute for Microelectronics and Microsystems (IMM) of the Consiglio Nazionale delle Ricerche (CNR). During the Ph.D. period he spent three months, as a visiting student, in the SCREEN-LASSE laboratory. He also collaborated with the LAAS-CNRS in Tolouse (Fr), through the Understanding and Modeling of Excimer Laser Annealing (UMEX) project.

His research activities mainly concern the interaction between electromagnetic field and materials, in particular with respect to the dielectrophoresis technique, the plasma environment and the thermal annealing of materials with infrared laser for microelectronics.

He is author or coauthor of several publications in international journals (JCR). During the Ph.D. course he has presented the results of his work at the main European conferences giving oral contributions.

List of publications

- Quantitative modelling of the nanoscale evolution during the explosive crystallization phenomenon. S.F. Lombardo, S. Boninelli, F. Cristiano et al. Submitted to JAP;

- Phosporous doped large Si nanoparticles as anode material for lithium-ion batteries. G. Mannino, F. Monforte, S.F. Lombardo and A. La Magna. To be submitted to ACS NANO;

- Atom by Atom simulation of nano-materials manipulation: the plasma etching case. A. Campo, S. F. Lombardo et al.IEEE Transactions on Nanotechnology PP(99):1-1 · June 2017.
DOI: 10.1109/TNANO.2017.2719281.

- Nonequilibrium steady states and electron transport in molecular systems. I. Deretzis, S. F. Lombardo, G. G. N. Angilella, R. Pucci, A. La Magna. book: Correlations in Condensed Matter under Extreme Conditions, Edition: I, Chapter: 10, Publisher: Springer International Publishing, pp.pp 127-150; isbn:978-3-319-53664-4.
DOI: 10.1007/978-3-319-53664-4_10

- Laser annealing in Si and Ge: Anomalous physical aspects and modeling approaches. S.F. Lombardo, S. Boninelli, F. Cristiano, F. et al. Materials Science in Semiconductor Processing.
DOI: 10.1016/j.mssp.2016.10.047.

- Elution time changes due to anomalous DEP effects in microchannels under uniform and non-uniform electric fields; A. Magliano, M. Camarda, S.F. Lombardo, et al., Sensing and Bio-Sensing Research Volume: 8 Pages: 59-64 Published: 2016.
DOI: 10.1016/j.sbsr.2016.02.004.

- Fluoro-Carbon Chemistry: 0-dimensional model for oxide and nitride dry etching; Garozzo G., Colombo S., Lombardo S. F., La Magna A., IEEE Transactions on Semiconductor Manufacturing.
DOI: 10.1109/TSM.2015.2427876.

- Relazione tecnica sulle simulazioni a molte scale di processi di deposizione assistiti da plasma con applicazione alla fabbricazione di celle fotovoltaiche a film sottile. Prt.n°0006841 del 11/09/2014

List of conferences

My own contributions

- Materials.it 2016 (Aci Castello, IT), 12/2016. Presentation: The multiwell phase-field of the explosive crystallization phenomenon.

- Nanosea2016 (Giardini Naxos, IT), 7/2016. Presentation: Quantitative predictions of the nanoscale evolution during the explosive crystallization phenomenon.

- E-MRS Spring meeting 2016 (Lille, Fr) 6/2016. Presentation: Quantitative modelling of the explosive crystallization phenomenon.

- E-MRS Spring meeting 2014 (Lille, Fr), 5/2014. Presentation: Boron activation and defects dynamics in Si solid phase during excimer laser annealing processes. Symposium X, Materials research for group IV semiconductors: growth, characterization and technological developments

- E-MRS Spring meeting 2014 (Lille, Fr), 5/2014. Poster: Simulation and design of thin film solar cells. Symposium Y, Advanced materials and characterization techniques for solar cells.

Other contributions

- FEniCS'17, (Luxemburg, LU), 6/2017. Presentation: LIAB: a FEniCS based computational tool for laser annealing simulation

- FEniCS'17, (Luxemburg, LU), 6/2017. Poster: MD-FEM Force Field Simulation of particle subjected to dielectrophoresis interaction

- MRS 2017 Spring meeting, (Phoenix, USA), 4/2017. Presentation: Investigation of n-type Germanium doping by melting laser annealing. Symposium ED3, Physics, chemistry and materials for beyond silicon electronics.

- Materials.it2016 (Aci Castello, IT), 12/2016. Poster: Force field simulations of particle subjected to dielectrophoresis interaction.

Bibliography

[1] A. Bogaerts, E. Neyts, R. Gijbels, and J. van der Mullen. "Gas discharge plasmas and their applications". In: *Spectrochimica Acta* 57 (Apr. 2002), pp. 609–658. DOI: 10.1016/S0584-8547(01)00406-2.

[2] D. Petersohn. "Principles of plasma discharges and materials processing. Von. M. A. Liebermann und A. J. Lichtenberg, XXVI, 572S., John Wiley & Sons, Inc., New York 1994, £ 54.00, ISBN 0-471-00577-0". In: *Materials and Corrosion* 46.9 (1995), pp. 551–551. ISSN: 1521-4176. DOI: 10.1002/maco.19950460909. URL: http://dx.doi.org/10.1002/maco.19950460909.

[3] Comsol Multipysics, ed. *The Plasma Module User's Guide*.

[4] C. Cavallotti, M. Di Stanislao, and S. Carrà. "Interplay of physical and chemical aspects in the PECVD and etching of thin solid films". In: *Progress in Crystal Growth and Characterization of Materials* 48-49.Supplement C (2004). Vapour Growth of Bulk Crystals and Epitaxy: Part II, pp. 123–165. ISSN: 0960-8974. DOI: https://doi.org/10.1016/j.pcrysgrow.2005.05.003. URL: http://www.sciencedirect.com/science/article/pii/S0960897405000239.

[5] R. Winkler. "Swarm Studies and Inelastic Electron-Molecule Collisions. Proceedings of the Meeting of the Fourth International Swarm. Seminar and the Inelastic Electron-Molecule Collision Symposium, Tahoe City, 1985, California, USA. Edited by L. C. Pitchford, B. V. McKoy, A. Chutjian, S. Trajmar Springer-Verlag 1987". In: *Beiträge aus der Plasmaphysik* 27.6 (1987), pp. 416–416. ISSN: 1521-3986. DOI: 10.1002/ctpp.19870270603. URL: http://dx.doi.org/10.1002/ctpp.19870270603.

[6] R. Cariou, R. Ruggeri, X. Tan, Giovanni Mannino, J. Nassar, and P. Roca i Cabarrocas. "Structural properties of relaxed thin film germanium layers grown by low temperature RF-PECVD epitaxy on Si and Ge (100) substrates". In: *AIP Advances* 4.7 (2014), p. 077103. DOI: 10.1063/1.4886774. eprint: http://dx.doi.org/10.1063/1.4886774. URL: http://dx.doi.org/10.1063/1.4886774.

[7] C. Lee, D. B. Graves, M. A. Lieberman, and D. W. Hess. "Global Model of Plasma Chemistry in a High Density Oxygen Discharge". In: *J. Electrochem. Soc.* 141.6 (1994), pp. 1546–1555. DOI: 10.1149/1.2054960. eprint: http://jes.ecsdl.org/content/141/6/1546.full.pdf+html. URL: http://jes.ecsdl.org/content/141/6/1546.abstract.

[8] L. Chiaramonte, R. Colombo, G. Fazio, G. Garozzo, and A. La Magna. "A numerical method for the efficient atomistic simulation of the plasma-etch of nano-patterned structures". In: *Computational Materials Science* 54 (2012), pp. 227–235. ISSN: 0927-0256. DOI: http://dx.doi.org/10.1016/j.commatsci.2011.10.027. URL: http://www.sciencedirect.com/science/article/pii/S0927025611005982.

[9] A. Campo, S. F. Lombardo, I. Deretzis, G. Garozzo, G. G. N. Angilella, and A. L. Magna. "Atom by Atom Simulations of Nanomaterial Manipulation: The Plasma Etching Case". In: *IEEE Transactions on Nanotechnology* 16.5 (Sept. 2017), pp. 790–797. ISSN: 1536-125X. DOI: 10.1109/TNANO.2017.2719281.

[10] F. Cristiano, M. Shayesteh, R. Duffy, K. Huet, F. Mazzamuto, Y. Qiu, M. Quillec, H.H. Henrichsen, P.F. Nielsen, D.H. Petersen, A. La Magna, G. Caruso, and S. Boninelli. "Defect evolution and dopant activation in laser annealed Si and Ge". In: *Materials Science in Semiconductor Processing* 42, Part 2 (2016). E-MRS Spring Meeting 2015 Symposium Z: Nanomaterials and processes for advanced semiconductor {CMOS} devices, pp. 188–195. ISSN: 1369-8001. DOI: http://dx.doi.org/10.1016/j.mssp.2015.09.011. URL: http://www.sciencedirect.com/science/article/pii/S136980011530189X.

[11] A. A. Wheeler, W. J. Boettinger, and G. B. McFadden. "Phase-field model for isothermal phase transitions in binary alloys". In: *Phys. Rev. A* 45 (10 May 1992), pp. 7424–7439. DOI: 10.1103/PhysRevA.45.7424. URL: http://link.aps.org/doi/10.1103/PhysRevA.45.7424.

[12] Antonino La Magna, Paola Alippi, Vittorio Privitera, Guglielmo Fortunato, Marco Camalleri, and Bengt Svensson. "A phase-field approach to the simulation of the excimer laser annealing process in Si". In: *Journal of Applied Physics* 95.9 (2004), pp. 4806–4814. DOI: 10.1063/1.1690861. eprint: http://dx.doi.org/10.1063/1.1690861. URL: http://dx.doi.org/10.1063/1.1690861.

[13] Antonino La Magna, Paola Alippi, Vittorio Privitera, and Guglielmo Fortunato. "Role of light scattering in excimer laser annealing of Si". In: *Applied Physics Letters* 86.16, 161905 (2005). DOI: http://dx.doi.org/10.1063/1.1906318. URL: http://scitation.aip.org/content/aip/journal/apl/86/16/10.1063/1.1906318.

[14] G. Fisicaro, K. Huet, R. Negru, M. Hackenberg, P. Pichler, N. Taleb, and A. La Magna. "Anomalous Impurity Segregation and Local Bonding Fluctuation in *l*-Si". In: *Phys. Rev. Lett.* 110 (11 Mar. 2013), p. 117801. DOI: 10.1103/PhysRevLett.110.117801. URL: http://link.aps.org/doi/10.1103/PhysRevLett.110.117801.

[15] G. Impellizzeri, E. Napolitani, S. Boninelli, G. Fisicaro, M. Cuscunà, R. Milazzo, A. La Magna, G. Fortunato, F. Priolo, and V. Privitera. "B-doping in Ge by excimer laser annealing". In: *Journal of Applied Physics* 113.11, 113505 (2013). DOI: http://dx.doi.org/10.1063/1.4795268. URL: http://scitation.aip.org/content/aip/journal/jap/113/11/10.1063/1.4795268.

[16] E. Bruno, G. G. Scapellato, A. La Magna, M. Cuscunà, E. Napolitani, S. Boninelli, F. Priolo, G. Fortunato, and V. Privitera. "Anomalous transport of Sb in laser irradiated Ge". In: *Applied Physics Letters* 101.17, 172110 (2012). DOI: http://dx.doi.org/10.1063/1.4764069. URL: http://scitation.aip.org/content/aip/journal/apl/101/17/10.1063/1.4764069.

[17] R. Milazzo, E. Napolitani, G. Impellizzeri, G. Fisicaro, S. Boninelli, M. Cuscunà, D. De Salvador, M. Mastromatteo, M. Italia, A. La Magna, G. Fortunato, F. Priolo, V. Privitera, and A. Carnera. "N-type doping of Ge by As implantation and excimer laser annealing". In: *Journal of Applied Physics* 115.5, 053501 (2014). DOI: http://dx.doi.org/10.1063/1.4863779. URL: http://scitation.aip.org/content/aip/journal/jap/115/5/10.1063/1.4863779.

[18] G. Fisicaro, L. Pelaz, P. Lopez, and A. La Magna. "Kinetic Monte Carlo simulations for transient thermal fields: Computational methodology and application to the submicrosecond laser processes in implanted silicon". In: *Phys. Rev. E* 86 (3 Sept. 2012), p. 036705. DOI: 10.1103/PhysRevE.86.036705. URL: http://link.aps.org/doi/10.1103/PhysRevE.86.036705.

[19] G. Fisicaro and A. La Magna. "Modeling of laser annealing". In: *Journal of Computational Electronics* 13.1 (Mar. 2014), pp. 70–94. ISSN: 1572-8137. DOI: 10.1007/s10825-013-0545-9. URL: https://doi.org/10.1007/s10825-013-0545-9.

[20] R. Milazzo, G. Impellizzeri, D. Piccinotti, A. La Magna, G. Fortunato, D. De Salvador, A. Carnera, A. Portavoce, D. Mangelinck, V. Privitera, and E. Napolitani. "Impurity and defect interactions during laser thermal annealing in Ge". In: *Journal of Applied Physics* 119.4, 045702 (2016). DOI: http://dx.doi.org/10.1063/1.4940737. URL: http://scitation.aip.org/content/aip/journal/jap/119/4/10.1063/1.4940737.

[21] Yang Qiu, Fuccio Cristiano, Karim Huet, Fulvio Mazzamuto, Giuseppe Fisicaro, Antonino La Magna, Maurice Quillec, Nikolay Cherkashin, Huiyuan Wang, Sébastien Duguay, and Didier Blavette. "Extended Defects Formation in Nanosecond Laser-Annealed Ion Implanted Silicon". In: *Nano Letters* 14.4 (2014). PMID: 24588318, pp. 1769–1775. DOI: 10.1021/nl4042438. eprint: http://dx.doi.org/10.1021/nl4042438. URL: http://dx.doi.org/10.1021/nl4042438.

[22] J. Stefan. "Ueber die Theorie der Eisbildung, insbesondere über die Eisbildung im Polarmeere". In: *Annalen der Physik* 278.2 (1891), pp. 269–286. ISSN: 1521-3889. DOI: 10.1002/andp.18912780206. URL: http://dx.doi.org/10.1002/andp.18912780206.

[23] A. B. Tayler. "Free and Moving Boundary Problems. By J. CRANK. Clarendon, Oxford, 1984. 425 pp." In: *Journal of Fluid Mechanics* 158 (1985), pp. 532–533. DOI: 10.1017/S0022112085212750.

[24] Alain Karma and Wouter-Jan Rappel. "Quantitative phase-field modeling of dendritic growth in two and three dimensions". In: *Phys. Rev. E* 57 (4 Apr. 1998), pp. 4323–4349. DOI: 10.1103/PhysRevE.57.4323. URL: http://link.aps.org/doi/10.1103/PhysRevE.57.4323.

[25] N. A. Ahmad, A. A. Wheeler, W. J. Boettinger, and G. B. McFadden. "Solute trapping and solute drag in a phase-field model of rapid solidification". In: *Phys. Rev. E* 58 (3 Sept. 1998), pp. 3436–3450. DOI: 10.1103/PhysRevE.58.3436. URL: http://link.aps.org/doi/10.1103/PhysRevE.58.3436.

[26] E. V. Monakhov, B. G. Svensson, M. K. Linnarsson, A. La Magna, M. Italia, V. Privitera, G. Fortunato, M. Cuscunà, and L. Mariucci. "The effect of excimer laser pretreatment on diffusion and activation of boron implanted in silicon". In: *Applied Physics Letters* 87.19, 192109 (2005). DOI: http://dx.doi.org/10.1063/1.2126144. URL: http://scitation.aip.org/content/aip/journal/apl/87/19/10.1063/1.2126144.

[27] K. K. Ong, K. L. Pey, P. S. Lee, A. T. S. Wee, X. C. Wang, and Y. F. Chong. "Dopant distribution in the recrystallization transient at the maximum melt depth induced by laser annealing". In: *Applied Physics Letters* 89.17, 172111 (2006). DOI: http://dx.doi.org/10.1063/1.

2364834. URL: http://scitation.aip.org/content/aip/journal/apl/89/17/10.1063/1.2364834.

[28] I. Štich, R. Car, and M. Parrinello. "Bonding and disorder in liquid silicon". In: *Phys. Rev. Lett.* 63 (20 Nov. 1989), pp. 2240–2243. DOI: 10.1103/PhysRevLett.63.2240. URL: https://link.aps.org/doi/10.1103/PhysRevLett.63.2240.

[29] J. T. Okada, P. H.-L. Sit, Y. Watanabe, Y. J. Wang, B. Barbiellini, T. Ishikawa, M. Itou, Y. Sakurai, A. Bansil, R. Ishikawa, M. Hamaishi, T. Masaki, P.-F. Paradis, K. Kimura, T. Ishikawa, and S. Nanao. "Persistence of Covalent Bonding in Liquid Silicon Probed by Inelastic X-Ray Scattering". In: *Phys. Rev. Lett.* 108 (6 Feb. 2012), p. 067402. DOI: 10.1103/PhysRevLett.108.067402. URL: https://link.aps.org/doi/10.1103/PhysRevLett.108.067402.

[30] N. Jakse and A. Pasturel. "Dynamics of liquid and undercooled silicon: An ab initio molecular dynamics study". In: *Phys. Rev. B* 79 (14 Apr. 2009), p. 144206. DOI: 10.1103/PhysRevB.79.144206. URL: https://link.aps.org/doi/10.1103/PhysRevB.79.144206.

[31] P. M. Fahey, P. B. Griffin, and J. D. Plummer. "Point defects and dopant diffusion in silicon". In: *Rev. Mod. Phys.* 61 (2 Apr. 1989), pp. 289–384. DOI: 10.1103/RevModPhys.61.289. URL: https://link.aps.org/doi/10.1103/RevModPhys.61.289.

[32] K. Huet, G. Fisicaro, J. Venturini, H. Besaucèle, and A. La Magna. "Defect kinetics and dopant activation in submicrosecond laser thermal processes". In: *Applied Physics Letters* 95.23, 231901 (2009). DOI: http://dx.doi.org/10.1063/1.3268472. URL: http://scitation.aip.org/content/aip/journal/apl/95/23/10.1063/1.3268472.

[33] S.F. Lombardo, S. Boninelli, F. Cristiano, G. Fisicaro, G. Fortunato, M.G. Grimaldi, G. Impellizzeri, M. Italia, A. Marino, R. Milazzo, E. Napolitani, V. Privitera, and A. La Magna. "Laser annealing in Si and Ge: Anomalous physical aspects and modeling approaches". In: *Materials Science in Semiconductor Processing* 62 (2017). Advanced doping methods in semiconductor devices and nanostructures, pp. 80–91. ISSN: 1369-8001. DOI: http://dx.doi.org/10.1016/j.mssp.2016.10.047. URL: http://www.sciencedirect.com/science/article/pii/S1369800116304899.

[34] Daniel Payne. *FinFETs for your Next SoC*. 2014. URL: https://www.semiwiki.com/forum/content/3792-finfets-your-next-soc.html.

[35] C. Fenouillet-Beranger, B. Mathieu, B. Previtali, M. P. Samson, N. Rambal, V. Benevent, S. Kerdiles, J. P. Barnes, D. Barge, P. Besson, R. Kachtouli, M. Cassé, X. Garros, A. Laurent, F. Nemouchi, K. Huet, I. Toqué-Trésonne, D. Lafond, H. Dansas, F. Aussenac, G. Druais, P. Perreau, E. Richard, S. Chhun, E. Petitprez, N. Guillot, F. Deprat, L. Pasini, L. Brunet, V. Lu, C. Reita, P. Batude, and M. Vinet. "New insights on bottom layer thermal stability and laser annealing promises for high performance 3D VLSI". In: *2014 IEEE International Electron Devices Meeting*. Dec. 2014, pp. 27.5.1–27.5.4. DOI: 10.1109/IEDM.2014.7047121.

[36] G. Götz. "Explosive crystallization processes in silicon". In: *Applied Physics A* 40.1 (May 1986), pp. 29–36. ISSN: 1432-0630. DOI: 10.1007/BF00616588. URL: https://doi.org/10.1007/BF00616588.

[37] Italy Trevi, J M Poate, Gaetano Foti, and D.C Jacobson. *Surface modification and alloying by laser, ion, and electron beams / edited by J. M. Poate G. Foti and D.C. Jacobson.* Ed. by Springer Science & Business Media. Nov. 2013, p. 414.

[38] Feyyaz Ozdemir and Aysegul Kargi. "Electromagnetic Waves and Human Health". In: *Electromagnetic Waves*. Ed. by Vitaliy Zhurbenko. Rijeka: InTech, 2011. Chap. 22. DOI: 10.5772/16343. URL: http://dx.doi.org/10.5772/16343.

[39] Antonino Magliano, Massimo Camarda, Salvatore Francesco Lombardo, Rossana Di Martino, Michele Cascio, Alessandra Romano, Luigi Minafra, Giorgio Russo, Mariacarla Gilardi, Francesco Di Raimondo, Silvia Scalese, and Antonino La Magna. "Elution time changes due to anomalous DEP effects in microchannels under uniform and non-uniform electric fields". In: *Sensing and Bio-Sensing Research* 8.Supplement C (2016), pp. 59–64. ISSN: 2214-1804. DOI: https://doi.org/10.1016/j.sbsr.2016.02.004. URL: http://www.sciencedirect.com/science/article/pii/S2214180416300162.

[40] Giovanni Mannino, Francesca Monforte, Salvatore Francesco Lombardo, and Antonino La Magna. "Phosphorous doped large Si nanoparticles as anode material for lithium-ion batteries". In: *Submitted to ACS Nano* ().

[41] Salvatore Francesco Lombardo, Simona Boninelli, Fuccio Cristiano, Maria Grazia Grimaldi, Karim Huet, Enrico Napolitani, and Antonino La Magna. "Quantitative modelling of the nanoscale evolution during the explosive crystallization phenomenon". In: *Submitted to Journal of Applied Physics* ().